Review

Intrinsic intermediate gap states of TiO_2 materials and their roles in charge carrier kinetics

Baoshun Liu[a,*], Xiujian Zhao[a], Jiaguo Yu[b], Ivan P. Parkin[c], Akira Fujishima[d], Kazuya Nakata[d]

[a] State Key Laboratory of Silicate Materials for Architectures, Wuhan University of Technology, Wuhan City, Hubei Province 430070, PR China
[b] State Key Laboratory of Advanced Technology for Material Synthesis and processing, Wuhan University of Technology, Wuhan City, Hubei Province 430070, PR China
[c] Department of Chemistry, Materials Chemistry Centre, University College London, 20 Gordon St., London WC1H 0AJ, UK
[d] Research Institute for Science and Technology, Energy and Environment Photocatalyst Research Division, Tokyo University of Science, 1-3 Kagurazaka, Shinjuku-ku, Tokyo 162-8601, Japan

Keywords:
TiO_2 materials
Intermediate gap states
Intrinsic defects
Charge carrier localization
Charge carrier kinetics
Photocatalysis

A B S T R A C T

Titanium dioxide (TiO_2) is regarded as an important prototype photocatalytic material for several decades. The charge carrier kinetics determines the photocatalytic properties of TiO_2 materials; this is found to be greatly dependent on electronic structures. It has been revealed that the intrinsic intermediate gap states (intrinsic GSs) play a significant role in charge carrier kinetics that drive the photocatalytic processes of TiO_2 materials, which are not well summarized until now. Motivated by this thought, the purpose of this review focuses on physiochemical science of the intrinsic GSs of TiO_2 materials and their important role in charge carrier kinetics. We first give a summary on the chemical resources of the intrinsic GSs in TiO_2 and their physiochemical nature. Their general energy distribution, charge carrier population, and the associated thermodynamic properties are also elaborated from an overall viewpoint. We further carefully summarize and compare the experimental studies on the energy and the density distribution of the intrinsic GSs and discuss the associated chemical resources and charge carrier localizations. Trapping is the dominant function of intrinsic GSs in the charge carrier kinetics of TiO_2 materials. The significant effect of trapping on the transport, recombination, and interfacial transfer of charge carriers are also comprehensive summarized. Furthermore, the effects of charge carrier kinetics on photocatalytic performances are also discussed to some extents. Because of the importance of intrinsic GSs in modulating charge carrier kinetics, it is expected to increase the photocatalytic activity by engineering the intrinsic GSs, not only for TiO_2 materials, but also for the other semiconductor photocatalysts.

Contents

Baoshun Liu was born in 1977 in inner Mongolia, China. He received his BS and MS in material science from Wuhan university of Technology, and his Ph.D in material physics and chemistry in 2006 from Wuhan university of Technology. In 2013, he became a professor at Wuhan University of Technology. He was awarded a standard postdoctoral fellowship from japan society for the promotion of science (JSPS) at Kanagawa Academy of Science and Techology from 2010 to 2012, an invitation scholar supported by JSPS at Tokyo university of Science from 2016 to 2017, a short-visiting scholar at University college London in 2015 and 2017. His current research interests mainly focus on thermodynamics and kinetics of semiconductor photocatalysis, as well as photocatalytic materials.

Xiujian Zhao was born in 1959 in Hunan Province, China. He received his BS in inorganic material engineering in 1982 from Wuhan Institute of Building Materials Technology, China and his MS in inorganic material engineering in 1985 from Kyoto institute of Technology, Japan. He received his Ph.D in Molecular engineering in 1988 from Kyoto University, Japan. Since 1988, he joined in Wuhan university of Technology as a lecturer. In 1993, he become a professor at Wuhan University of Technology. Since 2000, he was appointed as the director of Key Laboratory of Silicate Materials Science and Engineering, Ministry of Education (Wuhan university of technology). From 2011–2016, he served as the director of The State Key Laboratory of Silicate Materials for Architectures (Wuhan university of Technology). He received the Gottardi Prize from International Commission on Glass in 1998. His current research interest includes semiconductor photocatalysis and photoactive glass materials.

Jiaguo Yu received his BS and MS in chemistry from Central China Normal University and Xi'an Jiaotong University, respectively, and his PhD in Materials Science in 2000 from the Wuhan University of Technology. In 2000, he became a Professor of the Wuhan University of Technology. He was a post-doctoral fellow at the Chinese University of Hong Kong from 2001 to 2004, visiting scientist from 2005 to 2006 at the University of Bristol, and visiting scholar from 2007 to 2008 at the University of Texas, Austin. His research interests include semiconductor photocatalysis, photocatalytic hydrogen production, CO2 reduction, solar fuels, dye-sensitized and perovskite solar cells, adsorption, CO2 capture, graphene and related topics.

Ivan Paul Parkin was born in 1965 in UK. He received his BS in chemistry in 1986 from Imperial College, University of London, and his Ph.D in chemistry in Imperial College London in 1989. He became a lecturer in University College London (UCL) in 1993 and then a senior lecturer and a reader in UCL in 1997 and 1999. In 2000, he became a professor of inorganic and solid state chemistry in University College London. He was appointed as the head of the inorganic and material section, UCL chemistry in 2006 and the head of UCL chemistry in 2010. Since 2016, he was appointed as a Dean of Mathematical and Physical Science (MAPS) faculty, UCL. He were elected as a Fellow of Royal Society of Chemistry (RSC) in 2003 and a Fellow of the Institute of Materials, Minerals and Mining in 2005. He received many awards, including a PW Allen Award from Forensic Society, Griffith Medal from IOM-3, and Tilden Medal from RSC. His current research interest includes chemical vapour deposition, thin film for windows, inorganic analysis of oxide materials, materials with photocatalytic activities, for example. For more details see: https://www.ucl.ac.uk/chemistry/people/prof-ivan-p-parkin

Akira Fujishima was born in 1942 in Tokyo, Japan. He received his BSc. (1966) from the Yokohama National University, and his MSc (1968) and PhD (1971) in engineering from The University of Tokyo. He became a lecturer at Kanagawa University in 1971 and then a lecturer at The University of Tokyo in 1975. After serving as an associate professor (1978) and professor (1986), he became a professor at The University of Tokyo Graduate School of Engineering in 1995. He was appointed as the Chairman of the Kanagawa Academy of Science and Technology and Director of the Functional Materials Research Laboratory of the Central Japan Railway Company in 2003. He was appointed as professor emeritus of The University of Tokyo and later became a special university professor emeritus of The University of Tokyo in 2005. He served as the chairman for the Chemical Society of Japan from 2006 to 2007 and has been the Director of the China Research Center at the Japanese Science and Technology Agency since 2008. He has been the President of Tokyo University of Science since 2010 and a professor emeritus since 2018. He received the Asahi Prize in 1983, the Chemical Society of Japan Award in 2000, the Purple Ribbon Medal (Shijuhosho) in 2003, and in 2004 he received the Japan Prize and the Japan Academy Prize and was named an Honorable Citizen of Kawasaki City. He also received the Imperial Invention Award and Kanagawa Culture Award in 2006. He received a Cultural Contributor in 2010 and Cultural Merit in 2017.

Kazuya Nakata was born in 1977 in Sapporo, Japan. He received his BSc(2000) from Shizuoka University, and his MSc (2002) and PhD (2005) in science from Tokyo Metropolitan University under the supervision of Professor Masahiro Yamashita. In 2005, he joined Tohoku University as a research fellow of the Japan Society for the Promotion of Science(JSPS), and then joined the Massachusetts Institute of Technology in 2006 as a JSPS research fellow. He has been a full-time researcher in the photocatalyst group at the Kanagawa Academy of Science and Technology (KAST) since December 2007. In September 2010, he also joined in the Organic Solar Cell Assessment Project at KAST. He has also been a visiting associate professor at the Tokyo University of Science since January 2011. In April 2013, he has been an associate professor at the Tokyo University of Science. He received a Sano award for young scientists from the electrochemical society of Japan in 2012, The Japanese Photochemistry Association Prize for Young Scientist in 2013, green sustainable chemistry award for young scientist in 2016.

Notation

ΔH_f (kJ/mol) the enthalpy change by forming V_Os under isobaric conditions
n_{Vo} (cm^{-3}) the density of V_Os
N (cm^{-3}) the density of normal lattice sites
k_B (J/K) Boltzmann constant
T (K) absolute temperature
E_b (eV) binding energy of an exciton
m_{eh} relative reduced mass of exciton
ε (F/m) *D*ielectric constant
m_c relative effective mass of a CB electron
m_v relative effective mass of a VB hole
N_L (cm^{-3}) total density of exponential-distributed gap states
E_c energy position of the CB edge
T_c: (K or °C) a parameter controlling the gap state distribution depth
E_0 (eV) the most probable energy of monoenergetic gap states
σ (eV) thermal fluctuation broadening of the monoenergetic gap state distribution
$N(E_c)$ (cm^{-3}) DOS at the CB edge
υ_c (s^{-1}) the free carrier vibration velocity
σ_c (cm^2) capture cross-section of gap states
τ_r (s) electron emission time from gap states to the CB state
υ_{th} (s^{-1}) the attempted-escape frequency
E_T (eV) energy position of a gap state level
E_F (eV) Fermi level of electrons
N_t (cm^{-3}) total DOS of gap states
C_{gs} (F) chemical capacitance of gap states
$E_{F,0}$ (eV) Fermi level of thermodynamic electrons
E_d (eV) demarcation energy level for separating deep gap states with shallow ones
τ_0 (s) average trapping lifetime of free electrons at gap states
β_n (s) time constant per unit volume for capturing electrons
α_c defined as T/T_C
N_t (cm^{-3}) total DOS of monoenergetic gap states
n_s (cm^{-3}) density of electrons near surface
C_H (F) chemical capacitance of the Helmholtz layer
λ (eV) reorganization energy
$E_{F,Redox}$ (eV) Fermi level of redox couples in electrolyte
$\hbar$ (J s) the reduced Planck constant
D_n ($cm\,s^{-1}$) chemical diffusion coefficient of electrons
μ_n ($cm^2\,V^{-1}\,s^{-1}$) mobility of electrons
V_{fb} (V) the flat electrochemical potential
λ (eV) the reorganization energy
$E_{F,redox}$ (eV) the Fermi level of redox couples
m^* (kg) the free electron mass

1. Introduction

Environmental pollution and energy resource shortages are two serious issues limiting the continuous development of human society on a global scale in the new century [1–5]. Photocatalysis has been regarded as an effective tool to help deal with them by using sunlight [6–10]. Although many semiconductor materials are been investigated in photocatalytic applications over several decades [11–15], TiO_2 is still the most important one due to its excellent advantages over other photocatalytic materials [16–21]. In current studies, many kinds of TiO_2 materials were prepared by means of nanostructured construction [22–25], band structure engineering, defect structure modulation [26,27], and surface decoration, so as to promote photocatalytic performances and make use of visible light [28–30]. It is anticipated that TiO_2 will continue to be the most important prototype material in future photocatalytic studies.

The photocatalytic activity of TiO_2 materials is dependent on the kinetics of charge carriers (the holes and the electrons) and the reactant diffusion to their surfaces [31–35]. Under conventional conditions, the diffusion of reactants (O_2, organics molecule, and others) is usually fast [36–38], so often the charge carrier kinetics determine the photocatalytic efficiency. Studying charge carrier kinetics and their effects on photocatalysis is highly interesting to us; this is complicated when TiO_2 materials are in forms of nanostructures and contain significant defects [39–41]. In principle, the charge carrier kinetics are mainly affected by the electronic structures of TiO_2 materials, which are also shown to be related to the crystalline phases [42], exposed facets [43], interparticle boundaries [44–46], interfaces exposure to adsorbates [47], energy band bending [48], and others.[49,50].

Electronic structures of stoichiometric bulk TiO_2 consist of the O2p-derived valence band (VB) states and the Ti3d-derived conduction band (CB) states, with a bandgap separating them [51–54]. A bandgap energy (E_g) determines the wavelength of lights absorbed by TiO_2 materials. The energy positions of the VB edge and the CB edge decide the oxidized and reduced potentials of free electrons and free holes, respectively. In practical cases, the main electronic structures, i.e., the CB states and the VB states, are not the key factors determining the charge carrier kinetics of TiO_2 materials, especially nano-TiO_2 materials, whereas the intrinsic intermediate gap states are found to play a decisive role [55–57]. Charge carriers exist in a delocalized form when they reside in the CB states and the VB states for gap-state free TiO_2 materials. However, they tend to be trapped when the gap states are present, which are universally found to exist in nano-TiO_2 materials due to the presence of either intrinsic defects or extrinsic impurities [58–61]. The gap states are closely associated with the self-localization of charge carriers at TiO_2 normal lattice sites. For example, the self-localization of electrons at a normal Ti site results in an electron polaron, which features Ti3d states (Ti^{3+}) locating below the CB edge as an occupied gap state. The Ti^{3+}-induced gap states can absorb light from the visible to near infrared regions in addition to a trapping effect.

It was shown that the transport, the interfacial transfer, and the recombination of charge carriers are greatly affected by the intermediate trapping role of gap states [62–65]. As a result, the photocatalytic properties of TiO_2 materials can be modulated by engineering gap states through defect selective implantation [66–70]. The effects of gap states on charge carrier kinetics depend on their chemical resources (entities), charge localization, energy distributions, densities of states (DOS), and spatial distributions.

Many works studied the chemical entities of gap states, their role in charge carrier kinetics, as well as the connection with photocatalytic properties. The electronic structure and associated charge carrier kinetics caused by gap states can be studied by: transient absorption (TA) spectroscopy [71]; electron paramagnetic resonance (EPR) [72]; photoluminescence (PL) [73]; electrochemical techniques; photoelectron spectroscopy; surface photovoltage spectroscopy (SPS) [74]; microwave photoconductivity (MPC) [75] and the other methods [76–78]. The exact chemical entities and the spatial configuration of gap states cannot be directly revealed with these statistical techniques. The atomic-resolved technique (scanning tunneling microscope, STM) and first-principle calculations are also needed [79,80].

In recent years, some published review papers summarized the preparation, morphologies, electronic structures, defects, photocatalytic principles, as well as the photocatalytic properties of TiO_2 materials [9,81–87]. However, very few works have been devoted to summarizing the intrinsic intermediate gap states, we call gap states below, of TiO_2 materials and their role in charge carrier kinetics relating to photocatalytic and photoelectrochemical applications. Although a recent review article summarized the charge carrier trapping, recombination and transfer in TiO_2 photocatalysis [88], it actually did not associate the charge carrier kinetics with the gap states of TiO_2 materials. The physiochemical nature of gap states is complicated due to the different chemical entities and the different material types. A complete and full elaboration of gap states and their effects on charge carrier kinetics in TiO_2 photocatalysis and photoelectrochemistry is challenging but needed, so a comprehensive review on this topic is highly recommended. Therefore, it is the purpose of this review to summarize and discuss the progresses of the researches carried out into the gap states of TiO_2 materials, their properties, and their role in charge carrier kinetics associated with photocatalysis, so as to gain some deep insights into future selective electronic structure engineering for further improving photocatalytic activity. Although the extrinsic foreign dopants can also create intermediate gap states in TiO_2 materials, we will not consider them in this review and mainly focus on the intrinsic ones and their role in charge carrier kinetics so as to go deep to our discussion. The processing methods to create gap states in TiO_2 materials are also not the focal point of our review because we want to concentrate the science of gap sates.

Based the above thought, the structure of this review is organized as below. An overview of the chemical resources (entities) of gap states, their spatial distribution and mobilities is firstly summarized in Section 2. Section 3 illustrates the theoretical and experimental studies on the charge carrier localizations in the TiO_2 lattice, which determines the intrinsic physicochemical nature of the gap states. Section 4 elaborates on the general features of gap state energy distribution, charge carrier population statistics of electrons at gap states and their thermodynamic properties. The further summary of experimental studies on TiO_2 gap states and the association with chemical entities and charge carrier localization is presented in Section 5. The last section gives a comprehensive review on the charge carrier kinetics mediated by gap states and the relationship with photocatalytic activities. Finally, we give a bottom-to-top level summary that reflects the whole structure of this review and the relationship between different sections.

2. Chemical entities of gap states, spatial distribution, and mobilities

Intrinsic defects are important chemical entities that can introduce gap states in TiO_2 materials. The intrinsic defects of oxides, including vacancies and interstitial species, are formed by a thermal fluctuation [37,61,89]. O vacancies (V_Os) and Ti interstitials (Ti(i)s) are two main kinds of point defects in TiO_2 lattice. O interstitials and Ti vacancies are seldom reported, because TiO_2 materials usually appear as O-deficient n-type oxides [90–93]. The density of intrinsic point defects is determined by the enthalpy change (ΔH_f) by forming them under isobaric conditions according to [61,94]

$$n = Ne^{-\Delta H_f/k_B T} \quad (1)$$

where N, k_B, and T are the lattice site density, the Boltzmann constant, and the absolute temperature, respectively.

V_o is formed by removing a lattice O atom, simultaneously accompanied with the formation of an under-coordinated (uc-) Ti atoms, a local distortion, and excess electrons [95–97]. Ti(i) is formed by placing a Ti atom in the void of a distorted O-octahedral [98], which can cause a more local distortion relative to that induced by a V_O [99–103]. The densities of V_os and Ti(i)s are generally too low to cause an obvious visible light absorption [104–109], so extrinsic techniques, such as vacuum thermal-annealing [110], electron bombardment [111], Ar^+ ion sputtering [112], UV photon irradiations [113], and reductions [114–116] are usually used to create additional defects that make TiO_2 materials in a highly-reduced form. Strictly speaking, these extrinsically induced defects cannot be considered as the intrinsic defects of TiO_2 materials any longer, but belong to self-dopants [117,118]. There is almost no difference between the self-dopants and the intrinsic defects in addition to the densities.

Compared to bulk, surfaces are more important due to their direct connection with surface reactions. Ideal surfaces are formed by truncating lattice periodicities in different directions [119,120]. Engineering defect structures on a surface region is an effective pathway for tuning the photocatalytic activity of TiO_2 materials due to their role in changing charge carrier transfer [121,122]. Surface structures differ from surface to surface and from phase to phase. Taking anatase TiO_2 (a-TiO_2) as an example, the Wulff-constructed equilibrated shape includes the most stable {101} surfaces and the second most stable {001} surface [123]. The clean a-(101) (a-TiO_2 (101)) surface has (1×1) periodicity, consisting of 5-fold (5-f) and 6-f Ti atoms (Ti_{5c} and Ti_{6c}), as well as bridged 2-f and 3-f O atoms (O_{2c} and O_{3c}). A clean a-(001) (a-TiO_2 (001)) (1×1) surface is composed of Ti_{5c} and bridged O atoms, as well as fully coordinated O_{3c} atoms, which usually reconstructs to the (1×4) periodicity [124,125]. The most stable (110) surfaces of rutile (r-(110)) are characterized by rows of Ti_{5c} atoms alternating with rows of bridging O atoms [98,126]. The real surfaces of TiO_2 are not strictly smooth and consist of the terraces separated by steps and kinks [127]. V_O species are predominant on surface regions [128,129]. It was revealed that V_O species mainly locate at the sub-surface lattice sites of a-(101) and a-(001)-(1×4) surfaces, whereas they favorably reside on the top-surface of r-(110) as bridging V_O sites. In addition to intrinsic thermodynamic factors, the spatial distribution of V_O species at different sites was also found to depend on some environmental factors, such as the external strain, the electric field, and the surface adsorption. At temperatures higher than absolute zero degree, thermal mobilities of V_o on TiO_2 surfaces causes them to hop among different surface sites or between different surface layers has been observed. These features of V_O spatial distribution should have important effects on the gap states and the associated charge kinetics in TiO_2 photocatalysis.

2.1. Oxygen vacancies on rutile TiO_2 (r-TiO_2) surfaces

r-(110) surfaces were widely used as a prototype to study the catalytic reactions happening on the surface [129–131]. The density of V_Os on a r-(110) surface is quite large (5–10%) under standard preparation conditions; their spatial distribution was extensively studied over past decades [132–136]. DFT calculations show a favorable formation of bridging V_Os on r-(110) surfaces, compared to other surfaces and sub-surfaces [132]. As shown in Fig. 1(A)-

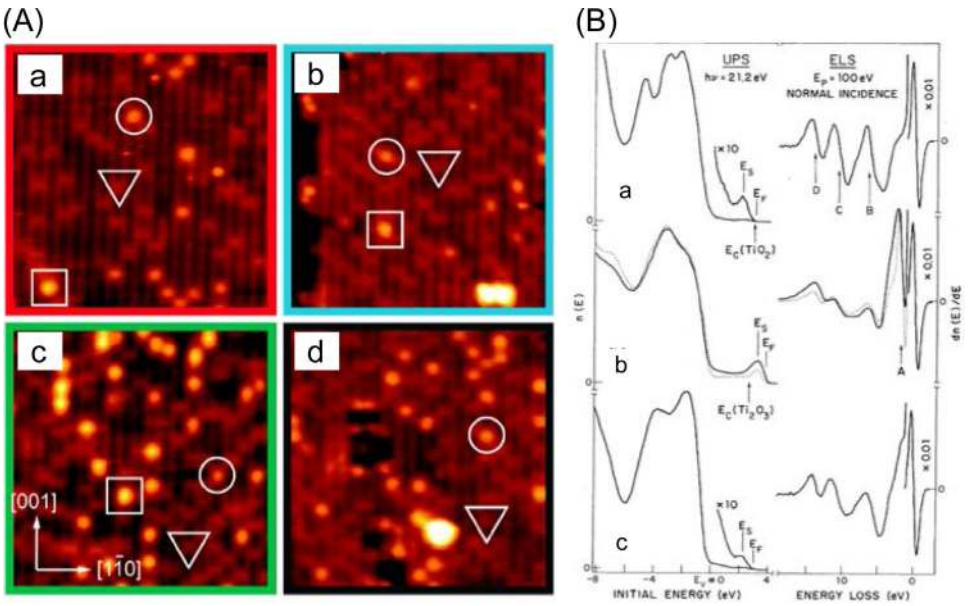

Fig. 1. (A) STM images (125×125 Å^2) of (a) the as-prepared r-(110) surface and its appearance after electron bombardment (kinetic energy ~75 eV, ~1 mA) for (b) 5, (c) 10, and (d) 20 s. Symbols indicate V_Os (triangles), bridging hydroxyls (circles), and hydroxyl pairs (squares). Reproduced with permission from Ref. [137]. Copyright 2010 American Physical Society. (B) UPS and ELS spectra for (a) annealed r-(110) surface, (b) Ar^+-bombarded r-(110) (solid curves) and vacuum-fractured r-(110) (dotted curves), and (c) Ar^+-bombarded r-(110) after exposure to 10 L of O_2.
Reproduced with permission from Ref. [138]. Copyright 1976 American Physical Society.

a, the preferential formation of bridging V_O species on an r-(110) surface was observed with high-resolution STM [137]. The V_O density can be varied by a low energy e-bombardment, as determined by the STM analysis (Fig. 1(A)-a–d)). The bridging-V_Os at a r-(110) surface were also studied in other research by using ultraviolet photoelectron spectroscopy (UPS) and electron energy loss spectroscopy (EELS) [138]. Fig. 1(B) shows the UPS spectra (left) and the ELS spectra (right) for an annealed r-(110) surface. The Ti3d-derived photoemission (PE) peak (a) was greatly increased after a period of Ar^+ sputtering (b), accompanied with the decrease of O-to-Ti cross excitations and the appearance of a strong peak associated with the d-to-d transitions involving Ti^{3+} ions, labeled as "A" in the ELS spectra. This observation showed that an Ar^+ sputtering created V_Os at r-(110) surfaces. A further exposure of the sputtered r-(110) surface to O_2 greatly decreases the intensity of Ti3d-derived PE peak (c), and also weakens the ELS peak "A". Such evidence revealed a location of the Ar^+ sputter induced V_Os on the top-surface, and also showed the presence of electron transfer from Ti3d states to the surface adsorbed O_2 molecule.

Both surface defects and sub-surface defects can contribute to Ti3d featured gap states. In recent research performed by Yang et al., the contribution of sub-surface defects of r-(110) surfaces was determined by UPS. The gentle photocatalytic dissociation of a methanol molecule on a r-(110) surface was used to quench top surface V_o sites by varying bridging hydroxyl density, whereas the density of sub-surface V_o sites remains unchanged, based on this the contribution to Ti3d states of sub-surface V_o species can be separated from the top-surface ones. The results showed that the contribution of sub-surface defects in r-(110) surfaces account for ~1.9% monolayer bridging hydroxyl groups, so they concluded that it is the top-surface defects that play a dominant role in determining the electronic structure in the gap of TiO_2 and the surface chemistry [139].

2.2. *Oxygen vacancies on anatase TiO_2 (a-TiO_2) surfaces*

A resonant photoemission (PE) spectroscopical study showed that the PE peaks derived from Ti3d electronic states of a-TiO_2 is higher than r-TiO_2 [140]. Because the Ti3d peak usually arises from V_O s, this result indicated that more V_Os exist on an a-(101) surface region than a r-(110) surface. However, other adsorption and calorimetric results suggested that an a-(101) top-surface has lower density of V_Os relative to a r-(110) top-surface [141–143]. It was also seen that an a-(101) surface is more difficult to reduce than a r-(110) surface under the same preparation conditions. These results indicate that V_Os do not reside on the top-layer of a-(101) surface region, but on the sub-surface layer. By means of density functional theory (DFT) calculations, STM, and XPS, a comprehensive study was carried out to disclose the location of V_Os on an a-(101) surface [144]. The V_O formation energies (E_{form}) at various surface and sub-surface sites were calculated in a slab model (Fig. 2(A)). As compared to the generation of top-surface V_O species (V_{O1}, V_{O2}, and V_{O3}), the formation of sub-surface V_O species (V_{O4} and V_{O5}) is more favorable in energy, also in line with other studies [132]. Location of V_os at the sub-surface sites was directly confirmed by the STM image (Fig. 2(B)); this shows that the freshly cleaved a-(101) surface is almost free of surface V_O sites. As shown in Fig. 1(C), V_Os led into a-TiO_2 by reduction exist in the form of half ovals residing in short chains along the [101], [111], or [$1\bar{1}\bar{1}$] directions, as marked with green, blue, and red small circles. These defects are different from the top-surface V_Os created by e-bombardments, because they are relatively inert and covered with adsorbates upon prolonged exposure to the residual gas. The sensitivity of their contrast in the STM images to bias or current indicated their location at surface region. These observations lead to a conclusion that V_O species predominantly locate at sub-surface sites, and tend to form linear arrays along the [101], [111], or [$1\bar{1}\bar{1}$] directions.

The V_o distribution differs dependent on different surfaces. For identically-prepared a-TiO_2 surfaces, it was found that the density of V_O species closely depends on the chemical nature of the surfaces. The most stable a-(101) surface contains the highest density of top-surface V_O species, whereas an a-(001) surface has a very low density of V_Os [145,146]. The population of V_Os at a-(101) surfaces and a-(001) surfaces was compared by resonant-XPS research [145]. The V_o-induced gap states undergoing a Ti3d feature resonance were used to indicate the formation of V_Os in an a-(101)

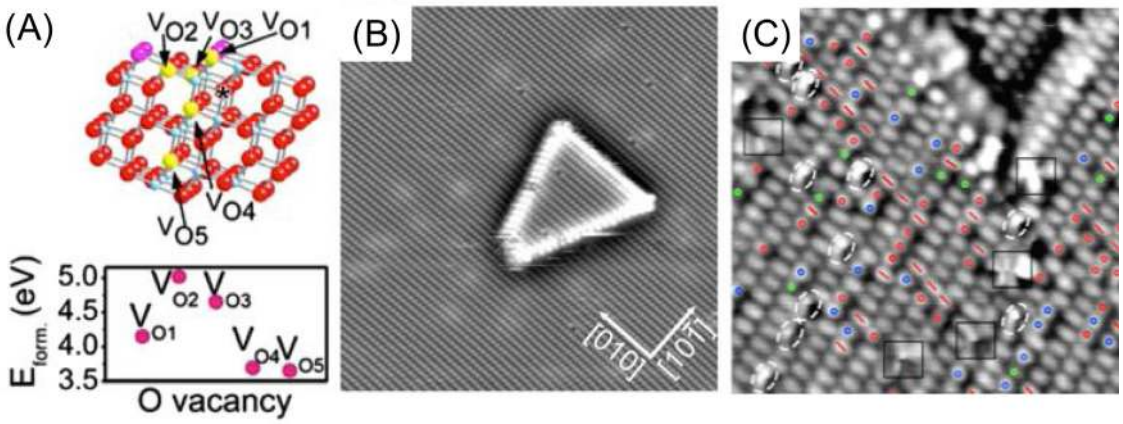

Fig. 2. (A)Various on- and subsurface V_Os (top) and their corresponding formation energies (down); (B) STM image of the freshly cleaned a-(101) surface and (C) high-resolution image (100×100 Å^2) with subsurface defects. Marked with colored circles are half ovals that are darker (green), same brightness (red), or brighter (blue) than regular ovals; red dashes mark extra-bright ovals.

Reproduced with permission from Ref. [144]. Copyright 2009 American Physical Society.

surface. The same surface treatment procedure generated more V_Os on an a-(101) surface than on an a-(001) surface. a-(001) surfaces usually suffer from a stress-driven (34) reconstruction [147,148]. The surface energy of (1×4) reconstructed surfaces (0.51 eV) is lower than that of (1×1) unreconstructed surfaces (~0.90 eV) [148]. The a-(001)-(1×4) surface is also more stable in energy with respect to the V_O creation in an a-(101) surface. To creating obvious V_O defects on reconstructed surfaces, higher energy Ar^+ sputtering and higher temperature annealing were needed. This conclusion was further supported by theoretical calculations. For example, irrespective of the surface or the sub-surface V_O sites, DFT computations showed that the formation of V_O on an a-(101) surface is more favorable than on an a-(001) surface [132,149]. The structural relaxation about V_O sites leads to larger atomic displacements in sub-surface region than at the top-surface, resulting in favorable location of V_Os at sub-surface sites of both a-(101)-(1×1) and a-(001)-(1×4) surfaces [69].

2.3. Effects of strain and electric field on oxygen vacancy spatial distribution

External stimuli can cause the spatial distribution of V_os in TiO_2 materials to deviate from their thermodynamic distribution. It was reported that the interaction between external strain and V_Os can lead to a redistribution of surface V_Os due to the change of surface elastic properties [150]. A theoretical calculation studied the interaction between an external strain and a V_o on a r-(110) surface [151]. As shown in Fig. 3(A), three different V_O sites, in a tri-layer model were considered. The dependences of V_O formation energies (left-y) and V_O induced surface energies (right-y) on external strains along $(1\bar{1}0]$ (ε_{11}) and [001] (ε_{22}) directions were computed, as shown in Fig. 3(B) and (C). The energetically (*E*-) favorable V_O appears on the bridged sites of the first layer in the absence of an external strain, which moves to the in-plane sites and the sub-bridging sites under a tensile strain along $(1\bar{1}0]$ direction and a compressive strain along either [001] or $(1\bar{1}0]$ direction. Such V_O spatial re-distribution engineered by external strains may have an important effect on surface reactivity and carrier kinetics, because external strains are common in nanostructures, thin films, and heterogeneous interfaces [152–154]. It was also reported in recent research that the strain in a 2-dimentional TiO_2 material can result in a great decrease of band gap, consequently leading to an obvious change in visible light responded activity [155]. In addition to the external strain, the external electric fields can also change the spatial distribution of V_o. For example, it was reported that the electric field applied between the STM tip and a-(101) surface can pull the sub-surface $V_{O,s}$ to the surface [126,156]. A recent theoretical calculation was also performed to investigate the effect of external electric fields on the V_o spatial distribution and energy stability. The electric field in the direction perpendicular to the a-(101) slab was simulated by adding a sawtooth-like potential to the bare ionic potential. The most stable surface and sub-surface V_O defects were focused. The calculation showed that the subsurface V_O is more stable in energy over the surface V_O in the absence of an electric field. When an electric field was applied, the surface V_O can be either stabilized or destabilized relative to the sub-surface V_O depending on the electric field direction. The formation energy shows a much stronger dependence on the electric field for a surface V_O than a subsurface V_O because of the reduced screening at the surface layer. The surface V_O becomes more stable than that sub-surface V_O when a positive electric field is applied in a GGA + U (3.3 eV) calculation. This study further showed that the effect of electric fields on subsurface-to-surface V_O migrations is relatively minor despite of their large influence on the relative stabilities [157].

2.4. Thermal mobilities of oxygen vacancies

In principle, V_O cannot be fixed at a certain site because of the diffusion activated by thermal fluctuation. The DFT [168] calculations showed that *E*-favorable diffusion pathway of a V_O is from surface to subsurface sites in an a-(101) surface. A 0.74 eV thermal barrier allows the V_O diffusion during annealing processes. However, the reverse V_o diffusion from sub-surface to surface sites is inhibited by a high thermal barrier (1.25 eV). Therefore, the top-surface V_O species created by sputtering or e-bombardment can easily move to sub-surface sites, which is in good agreement with the experimentally observed low density of defects [144]. Dynamic thermal diffusion leads to statistical population of V_O species at the top-surface, within subsurfaces, and in the bulk in terms of Boltzmann distribution, which was further verified by first-principle molecular dynamic calculations.

The V_o mobilities at a-(101) surface region were directly observed in a temperature-controlled high-resolved STM study [158] The pre-cleaned pristine a-(101) surface (Fig. 4(A)) was firstly exposed to electron irradiation to create and freeze the V_O species on the top-surface at very low temperature. The comparison between the STM images of an a-(101) surface (Fig. 4(A) vs. Fig. 4(B)) shows that the V_O specie appears as an extra bright fea-

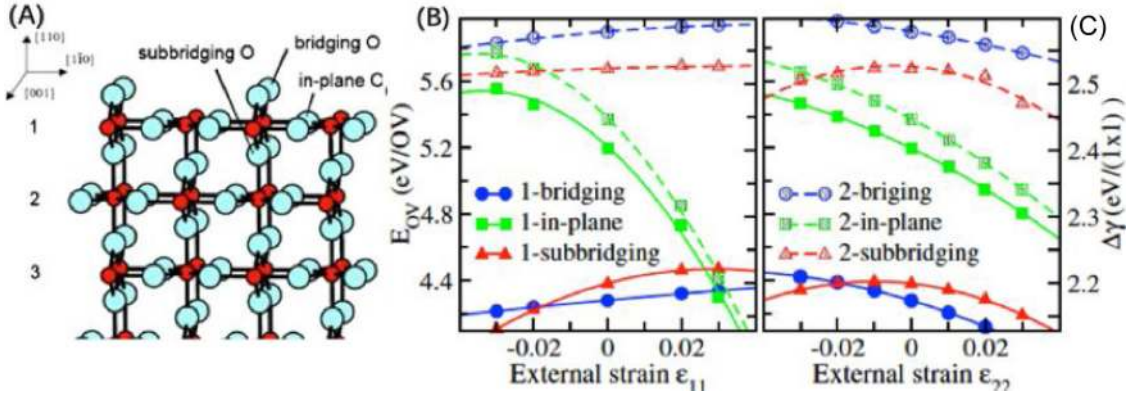

Fig. 3. (A) Slab model schematic of the r-(110) surface; The V_o formation energy E_{OV} (left-y) and surface energy (right-y) as a function of the applied strain along [1$\bar{1}$0] (B) and [001] (C).

Reproduced with permission from Ref. [151]. Copyright 2008 American Physical Society.

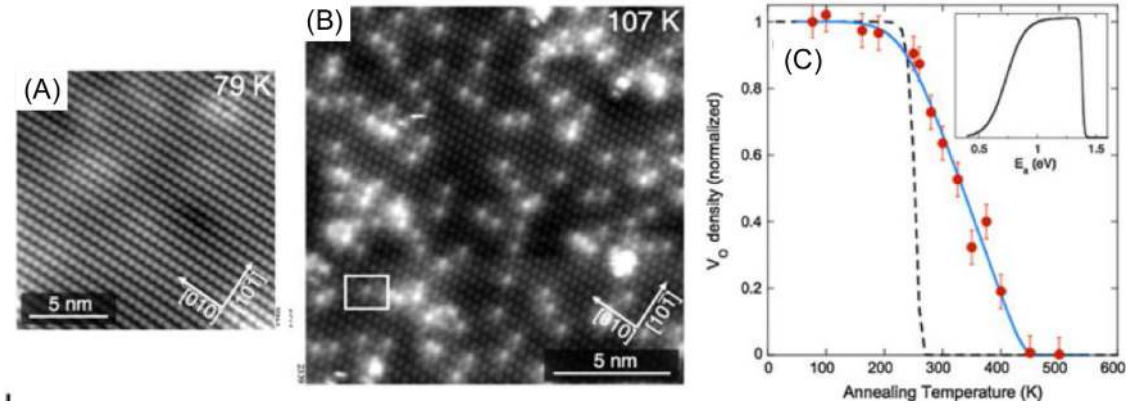

Fig. 4. STM images of the a-(101) surface. (A) The freshly prepared surface; (B) After further 500 eV electron beam bombardment. (C) Stability of surface electron beam induced V_Os. The plot shows the density of surface V_Os after heating the sample to various temperatures for 10 min, normalized to the initial value after electron bombardment at 105 K. The dashed line shows the expected behavior assuming one thermal barrier (0.75 eV). The solid line assumes the trapezoidal distribution of thermal barriers from 0.6 to 1.2 eV displayed in the inset.

Reproduced with permission from Ref. [158]. Copyright 2012 American Physical Society.

ture at regular bridging O lattice sites. It was seen that the density of surface V_O sites varied with heating at different temperatures (Fig. 4(C)). The surface V_O was found to be stable up to a 200 K temperature, and started to decrease greatly after heated to 230 K due to a surface-to-subsurface diffusion. The temperature-dependence of V_O density does not follow any diffusion models with a constant thermal barrier (E_{act}) (dashed line in Fig. 4(C)). The thermal barrier seems to be subject to a dynamical change due to a change of the immediate environments of each surface V_O. The diffusion model with varied thermal barriers fitted well with the experimental data in the solid line of Fig. 4(C). The time-lapse images at various temperatures further show that the V_o mobilities increase with the increase of temperature. At temperatures above 200 K, a temperature-dependent dynamic equilibrium of V_O population at the different sites on surface region and in the bulk is reached in a very short time, also in good accordance with the conclusions drawn by DFT calculations [158].

Differently from an a-(101) surface, the thermal intra-layer motion of bridging V_O species along bridging O rows is more favorable than an inter-layer motion for a r-(110) surface. The bridging V_o diffusion along a r-(110) surface was observed by an atomically-resolved STM [159]. Comparing Fig. 5(A) with (B) reveals the movement of two bridging V_Os along the [001] direction that results from an adjacent O movement in the opposite direction. The spatial distribution of all moved bridging V_O species was visualized from the difference image (Fig. 5(C)), which shows that the bridging V_O species exclusively diffuse along bridging O rows ([001] directions). The accordance of V_o motions with a random hopped walk model also reveals a thermal activation feature of V_O diffusions on a r-(110) surface. Fitting hopping rate with the Arrhenius mode leads to a thermal barrier of diffusion (1.15 ± 0.05 eV), in accordance with the 1.03 eV obtained from a DFT calculation [159].

2.5. Spatial distribution and mobilities of hydroxyl groups

Hydroxyls (OHs) are important defects that universally exist on TiO_2 surfaces. Strictly speaking, OHs cannot be regarded as intrinsic defects. However, OHs are commonly present on TiO_2 surface even freshly cleaned TiO_2 surfaces quickly undergo hydroxylation. The universal presence of OHs has a significant effect on the photocatalytic and photoelectrochemical behaviors of TiO_2 materials. Theoretical and experimental studies show that the localization of photoinduced holes on a TiO_2 surface results in (OH radicals [160–162], one of the main reactive oxygen species. The donation of excess electrons by H atoms also results in the localization of Ti3d-featured gap states. Therefore, hydroxyls are one of the key chemical entities for the intrinsic gap states in TiO_2 materials.

Water dissociation on TiO_2 surfaces is the main cause for OH formation; this was proposed to happen exclusively on defect sites associated with V_o species. High resolution STM measurements and DFT calculations are the commonly-used methods to study the spatial distributions and the mobilities of OHs on TiO_2 surfaces. For

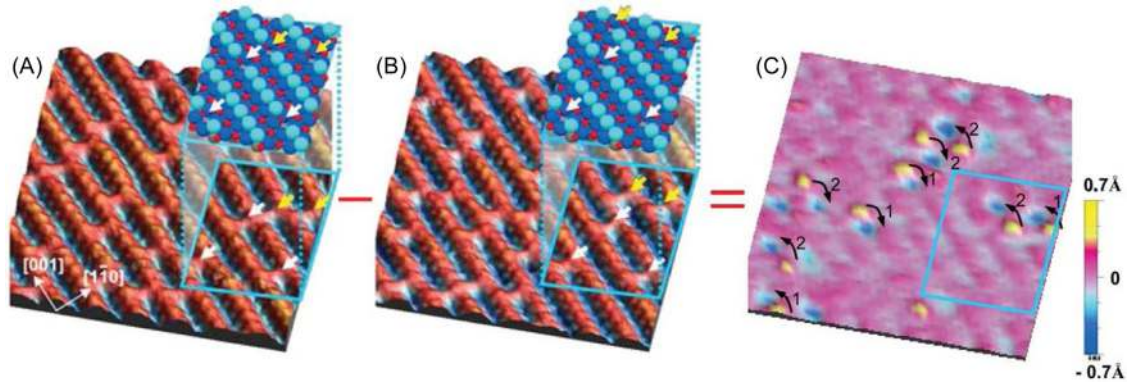

Fig. 5. (A) and (B) Two subsequent atomically-resolved empty state STM images taken from an STM movie that was obtained on the same area of a clean r-(110) at 400 K. Superimposed are ball models of r-(110) surface depicting regions of the STM images highlighted with blue squares. The rows of surface bridging O_s are light blue, lattice O ions dark blue, surface Ti ions red, and bridged V_os marked with arrows. (C) Difference image, in which (B) is subtracted from (A); the blue depressions indicate the new bridged V_O positions in (B) and the yellow protrusions indicate the original bridged V_O positions in (A).
Reproduced with permission from Ref. [159]. Copyright 2007 American Physical Society.

example, Schaub et al. studied the water dissociation on a r-(110) surface by combining the STM observations and the DFT calculations [163]. It was seen that the V_o species on a pre-cleaned r-(110) surface can be removed by a low dose of water. All of the hydroxyls situate on bridging O sites, without the terminal OH groups adhering to Ti_{5c} sites. This research shows the dissociative adsorption of water at bridging V_O sites via a proton transfer to a neighboring bridging O atom, which accordingly creates two bridging OHs per initial V_O. In stoichiometric surfaces, the dissociation state of water as hydroxyls is unstable relative to a molecular adsorption. Therefore, the presence of V_O makes the water dissociation strongly favorable due to the high-energy feature. The research performed by Bikondoa et al. showed that the H-adatoms on a bridged O of r-(110) surfaces can be selectively desorbed by applying voltage pulses from STM tips [164]. They firstly removed all of H-adatoms by STM scanning in a clean-off area, whilst leaving the V_O defects intact, and it was then seen that water exposure generated new OHs at V_O sites, solidly supporting the conclusion that water dissociates at V_O sites.

The dynamic interaction of water with a V_O on a reduced r-(110) surface and the OH mobilities were studied by using high-resolution STM [165]. They gave a clear picture of water dissociation at a V_o site and the resulted paired bridging hydroxyl groups (OHs). Importantly, it is shown that the OHs pair are immobile. However, the interaction with a water molecule can transfer protons to an adjacent O row, forming single OH group. By using a heavily reduced r-(110) surface with estimated bridging V_o concentration, a STM movie was recorded to see the water dissociation on a reduced r-(110) surface. Some sequenced snapshots are shown in Fig. 6. Various bright spots corresponding to OH_{br} pairs and single OH_{br} are discernible. The bridging V_O sites appear as faint spots; the molecular absorbed water is seen on Ti rows as protruding species, which can diffuse along Ti_{5c} troughs (Fig. 6(A)–(C)). When the water molecular reaches a Ti_{5c} next to a V_O, both of the water and the V_O disappear, and are replaced by an OH_{br} pair (Fig. 6(D)). This reaction dynamically monitored the water dissociation as two bridging OHs in a bridging V_O. After a water molecule has diffused to a Ti_{5c} next to an OH_{br} pair [Fig. 6(E) and (F)], the OH_{br} pairs split as two single OH_{br} (Fig. 6(G) and (H)). This observation shows that water molecules mediate the proton transfer from one bridged O row to another. The above dynamic views confirm that water dissociation at bridged V_O, sites is the major channel for producing the OH pairs. The DFT calculation shows that the energy barrier for proton transfer for water dissociation is ~0.2 eV. The dissociated OH pair state is ~0.4 eV more stable than the molecular state of water at an oxygen vacancy. The splitting of bridging OH pair prefers to occur, because transferring a proton from it is favored compared to the case where a proton is taken from the single bridged OH. Such a sequence of proton transfers was calculated to be possible also when a water molecule passes a single bridging OH. Accordingly, water molecules mediate the splitting of bridged OH pairs, as well as the net bridged OH diffusion along the [1−10] direction.

In addition to the V_o-mediated dissociation mechanism, an electron polaron (see Section 3) assisted water dissociation was also proposed in a solvated TiO_2 surface, which includes a delocalized and a localized case. In the delocalized case, the electrons delocalizing over a [010] row of the Ti_{5c} sites trigger water dissociation along a parallel O_{br} row. For a localized case, a typical water dissociation involves two water molecule closing to Ti^{3+} sites. One water molecule is initially adsorbed on a 5-f Ti^{4+} site other than the Ti^{3+} sites, and one H atom of second water molecule is bonded to the lattice bridging O next to Ti^{3+} site. Dissociation states with a proton transfer from the second water to the bridging O atom, resulting in the formation of an O_{br}-H and a solvated OH^-. The localized electron (Ti^{3+}) stabilizes the nearby O_{br}-H and leads to a second proton transfer from the first water to the solvated OH^-, resulting in a terminal OH^- on the "non-polaronic" Ti_{5c} on the other side of O_{Br}-H. This polaron-assisted dissociation of adsorbed water is consistent with previous studies showing a lower barrier for water dissociation on reduced (101) and is distinct from the reaction of a hydrated electron water to form solvated H and OH^-. The interaction of electron polarons with water can help us understand why anatase nanocrystals are generally observed to be hydroxylated in an aqueous environment.

2.6. Ti interstitial (Ti(i)) defects

Ti(i)s and Ti vacancies are two Ti point defects in TiO_2. Most of surface science studies so far focused on the Ti(i)s. Both V_Os and Ti(i)s are formed in TiO_2 during the sputtering and annealing process, and the Ti(i)s were found to be the main type of defects in slightly reduced TiO_2 relative to V_Os. In many cases, the Ti(i) mainly locate in a bulk distorted O octahedra, as shown in Fig. 7. The formation of a Ti(i) in the lattice is much more difficult that forming a V_o under an oxygen rich condition, whereas the formation energies of the two defect species are almost the same under a Ti rich condition, indicating the favorable formation of Ti(i)s in a reduction environment [166]. Another DFT calculation also showed the slightly favorable formation of V_Os relative to Ti(i)s in r-TiO_2 materials [167].

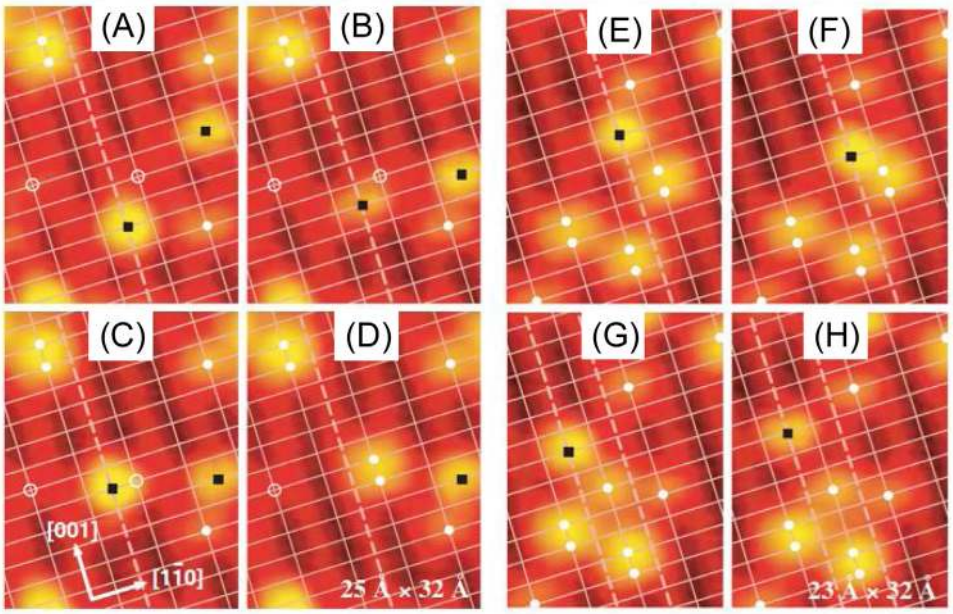

Fig. 6. (A)–(C) STM images for the dissociation of water in a bridging V_O on r-(110) at 187 K. Protrusions are labeled as follows: bridging V_Os (open white circles), OH_{br} groups (filled white circles), water on Ti_{5c} sites (filled black squares). (E)–(H) STM images for the splitting of an OH_{br} pair mediated by a water molecule at 187 K. Reproduced with permission from Ref. [165]. Copyright 2006 American Physical Society.

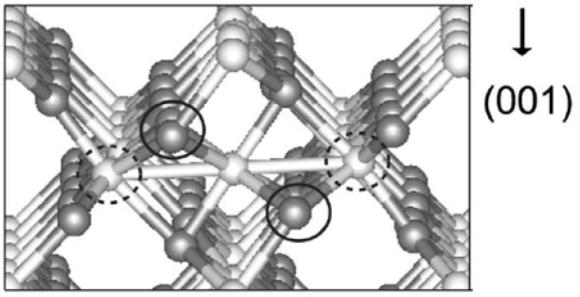

Fig. 7. Relaxed geometry around the Ti(i), dark and light gray spheres indicate O and Ti atoms, respectively. The atoms within circles are under largest relaxations. Reproduced with permission from Ref. [166]. Copyright 2006 American Physical Society.

In addition to bulk sites, Park et al. observed residence of Ti(i)s on r-TiO_2 surface by an ultrahigh vacuum STM study [168]. Fig. 8 shows the magnified STM image of an Ar-ion sputtered r-TiO_2(110) surface that was also followed by a further annealing. Fig. 8(A) shows that the surface exhibits strands terminated with bright spots on r-(110) terraces; this is attributed to a line of Ti adatoms along [001] right next to the Ti_{5c} row and right above the surface O_{3c} row. Fig. 8(B) shows that the height of this line of adatoms is 1.1–1.4 Å above the surface Ti_{5c} row, which indicates a real structural feature on r-(110) surface. The DFT geometry relaxations of a periodic Ti row added on a TiO_2 slab revealed the most stable position of the added Ti at an interstitial site "A": above the surface O_{3c} row, and another interstitial site "B" when Ti is shifted along [001] by half the lattice constant. The formation of such surface Ti(i)s is also accompanied with a surface lattice distortion so as to decrease the lattice stress. The partial complete octahedra centered on Ti(i)s share the edges of the equatorial O plane with each other along the row and share faces with the substrate octahedra. This edge- or face-sharing geometry provides a means to coordinate the Ti(i) cation octahedrally with oxygens at substoichiometry. The STM image of the edge- or face-sharing substoichiometric (1×1) r-(110) surface presents small terraces with half the height of that expected from corner-shared octahedra of bulk-like termination. By combining with a DFT calculation, the small terrace is assigned to the Ti_2O_2 row on a r-TiO_2 (110) surface with a protruded bridging O, as shown in Fig. 8(C). By removing the bridging O row from the Ti_2O_2 row, a geometrical relaxation results in a reconstructed Ti_2O structure with a (1*x*2) periodicity on a r-(110) surface.

The surface Ti(i) induced reconstruction of (1×1) periodicity to (1*x*2) periodicity proposed by Park et al. was also further observed by a TEM study [169]. The r-TiO_2 (110) surface were reduced in situ by a high-voltage electron irradiation during a TEM measurement. Both HV-TEM and HAADF-STEM showed the positions of Ti(i)s on a r-(110) surface on orthogonal projected images. Based on the contrast between Ti and O species, there is a stronger contrast in Ti columns and weaker in O columns, the high resolution HV-TEM images observed from different directions revealed the surface reconstruction that shifts the top Ti atoms from the expected positions, as labeled by the arrows (Fig. 9(C) and (E)). Similar results were also obtained from the HAADF-STEM images (Fig. 9(D) and (F)), where the bright contrast corresponds to the Ti columns. The simulated images for the HV-TEM and HAADF-STEM in the insets show good agreement of the assignment of O and Ti atoms on these images. The height of the Ti(i)s from the bottom Ti layer is estimated to be ~1.6 Å by the HAADF-STEM image. It is seen that the above observation is in good accordance with the (1*x*2) reconstructed model proposed by Park et al. [168].

In addition to the static location of Ti(i)s, their diffusion in a TiO_2 lattice was also studied by a first principle atomic dynamic calculation [167]. The Ti(i) diffusions along both the [001] and the [110] directions of r-TiO_2 were examined. The Ti(i) diffusion takes place through the interstitial region along the open [001] channels, accompanied with a lattice relaxation to accommodate the induced stress. The thermal barriers for Ti^{4+}(i) and Ti°(i) diffusion are 0.37 eV and 0.7 eV, respectively. The energy barrier of Ti^{4+}(i) diffusion along [110] is 0.225 eV. This is significantly lower than that along the [001] direction, also in reasonable accordance with experiential measurement more or less. The preferred Ti(i) diffusion along [110] direction is due to the different channels because the diffusion of Ti^{4+}(i) along [110] is not via the interstitial mecha-

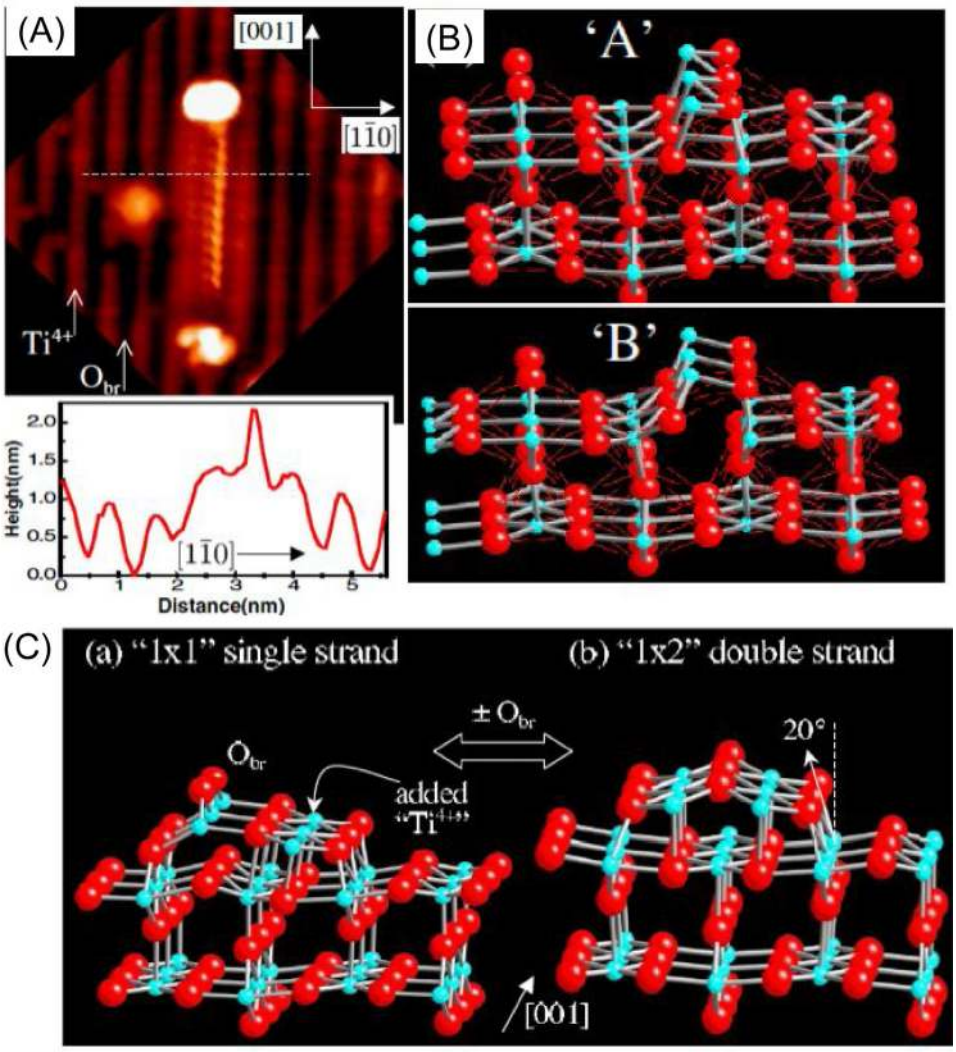

Fig. 8. (A) STM image of a strand on r-(110) surface with the height profiles across (dotted line) the line defect. (B) DFT-relaxed structures of a Ti(i) row on the r-(110) slab surface: at 'A' above surface O_{3c} row; at 'B' for Ti(i) aligned to bridging O along [110] (unfavored). (C) DFT-relaxed structures of (a) the Ti_2O_2 single strand with (1×1) periodicity and (b) the Ti_2O double strand with a (1x2) periodicity.

Reproduced with permission from Ref. [168]. Copyright 2006 American Physical Society.

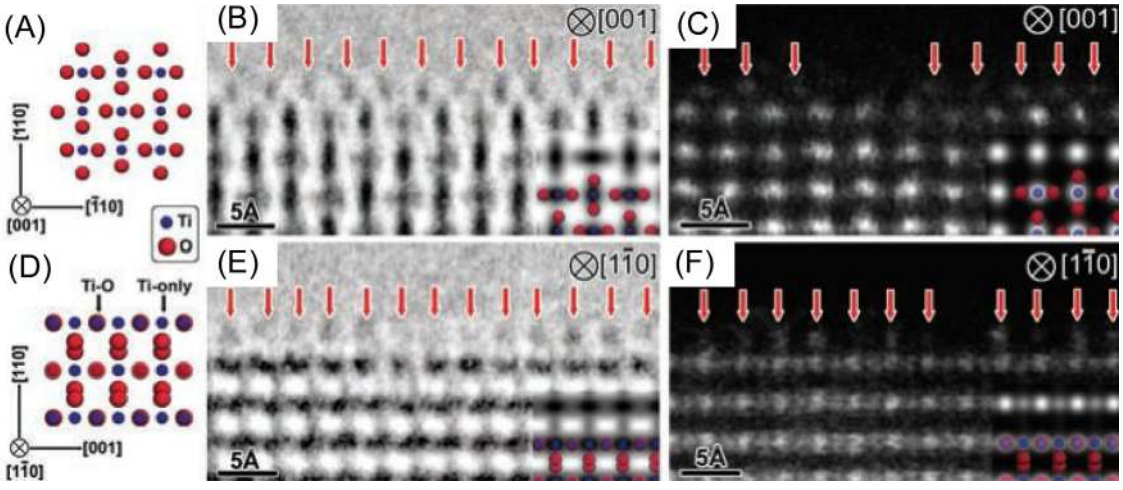

Fig. 9. Schematic illustrations of a r-(110) surface viewed along the [001] (A) and [110] (D) directions. The magnified high-voltage (HV-) TEM images of the r-(110) surface viewed from the [001] (B) and [110] (E) directions. The insets show the simulated images. Atomic-resolution HAADF-STEM images of the r-(110) surface after HV-TEM observations viewed from the [001] (C) and [110] (F) directions. The insets show the simulated HAADF-STEM images.

Reproduced with permission from Ref. [169]. Copyright 2008 AAAS [169].

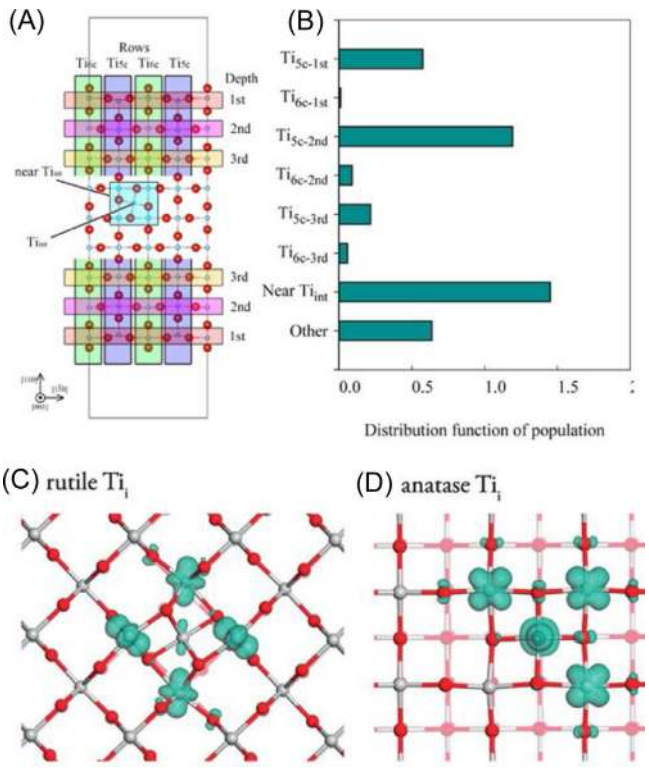

Fig. 10. (A) Schematic image of the surface slab model used in simulations. Small blue spheres represent Ti and large red spheres represent O. Grouping of Ti sites was performed according to the row and depth of each Ti site. The "near Ti(i)" group was defined as the four rows near Ti(i). Ti sites that did not belong to any group were denoted as the "other" groups. (B) Distribution function of the population calculated for each group. Reproduced with permission from Ref. [195]. Copyright 2017 American Chemical Society. Partial charge densities for the Ti(i) induced states in (C) r-TiO_2 and (D) a-TiO_{22}. The isosurfaces are shown at 0.05 eV/Å^3. Both images are viewed along the [001] crystal axes. Reproduced with permission from Ref. [189]. Copyright 2017 American Chemical Society.

nism as in the [001] case, but through the interstitial mechanism, in which the diffusion of a Ti(i) atom kicks out one of the bulk Ti atoms and takes its lattice position. The diffusion of Ti(i)s from bulk or sub-surfaces to top-surfaces were also indicated by STM [98], which revealed the formation of small islands with a height of ~2.2 Å on r-(110) terraces at 393 K. The further increase of temperature to 448 K increases the density of the islands, and some larger with a height of 3.2 Å were formed. The height of 3.2 Å closely corresponds to one TiO_2 layer. Therefore, the newly formed islands are attributed to the TiO_{2-x} structure caused by the migration of Ti(i)s from a deeper layer to interstitial sites in layers near the surfaces.

3. Physiochemical nature of gap states: charge carrier localization

Creating intrinsic defects (V_O and Ti(i) species) and surface hydroxylation will lead to thermal excess electrons in TiO_2 materials. Photoexcitation and electrochemical reduction can inject non-thermal excess electrons in TiO_2 [170,171]. Excess holes are mainly created by photo-excitation for n-type semi-conductors, such as TiO_2, ZnO, and other oxide materials, which are seldom studied as compared to the electrons [172,173]. Excess electrons and holes can be delocalized at the CB and the VB extended states, self-localized at regular lattice sites, or localized around defect sites. Different spatial distributions of charge carrier localization lead to different features of gap states, playing an important role in charge carrier transfer relating with surface reactions. The difference between the thermal and non-thermal electrons mainly lies in their thermodynamic features [39]; they are almost the same in spatial distribution. The spatial distribution of excess charge carriers is important to determine the physical nature of the gap states.

Localization/semi-localization of excess charges at regular lattice sites of TiO_2 results in polaron states, a main physical nature of gap states. The polaron results from the interaction between a carrier and ions in a polar material [174,175]. An immobilized charge carrier distorts the equilibrium configuration of nearby ions, and conversely the carrier position responds to the surrounding ions. The charge carrier and the responded surrounding local lattice distortion becomes a quasiparticle termed a polaron [176]. Depending on weak and strong interaction between charge carriers and lattice phonon modes, polarons are categorized as large and small. Large polarons typically extend over several lattice constants, having high motilities. Small polarons usually localize at a single site and can thermally hop from one site to another [177,178], leading to a population between free carriers and polarons according to thermodynamic statistics.

It is expected that the polarons commonly exist in TiO_2 materials and have a significant effect on the migration and the redox ability of charge carriers [179–181]. Electron polarons (e-polarons) were studied more extensively compared to hole polarons (h-polaron) due to the n-type feature of TiO_2. The e-polarons preferentially locate at specific Ti3d orbitals, and distort the local Ti-O octahedral geometry that is crucial for forming a small e-polaron [182]. The excess electrons can delocalize over several Ti sites to exist in large polaron or partially delocalized states [183]. Many studies were devoted to e-polarons and had gave a clear physical picture for spatial population of them. The spatial distribution of e-polarons includes the Ti sites where the electrons reside on, the Ti3d orbital configurations where the electron occupies, and the responded lattice distortion. The spatial distribution of e-polarons differs for different crystalline phases and different surfaces.

DFT calculations are main methods to study the spatial distribution of polarons in TiO_2. The actual results depend on the functionals used, which make the theoretical studies uncertain. The local density approximation (LDA) and the semi-local generalized gradient approximation (GGA) predict a rather delocalized feature of electrons because such functionals bias against localization on correlated *d* states; they are unable to provide a satisfactory description of e-polarons [184]. The usually used approaches, including the hybrid functional and the DFT + U (Hubbard correction), are shown to be useful for disclosing the polaron population, although the results are limited by the ad-hoc parameters (the value of *U* in DFT + *U* and the fraction of Hartree–Fock exchange in hybrid functional) [185,186].

3.1. Theoretical studies of charge carrier localization in TiO_2 materials

3.1.1. Bulk electron polarons (e-polarons)

Different Ti-O octahedron stacking in different TiO_2 polymorphs lead to different spatial distributions of e-polarons [187,188]. A DFT + *U* calculation was used to study the spatial distribution of V_O-induced bulk Ti polaron in r-TiO_2 and a-TiO_2 [189]. For r-TiO_2, the V_o-induced excess electrons are strongly localized at two Ti sites neighboring to the V_o, forming two Ti3d featured e-polarons. The polaron–polaron (p-p) interaction split the degenerated Ti3d levels as double gap states ~1.6 eV below the CB edge. Two excess electrons in a-TiO_2 are localized at Ti sites adjacent to the V_o and a next-nearest Ti in the mutual (100) plane, respectively. The two Ti3d e-polarons form a degenerated level ~1.5 eV below the CB edge. The formation of e-polarons leads to the movement of one O atom toward the V_o site. Localization of electrons at the V_O-neighbored Ti sites was also present for a-TiO_2, but 0.05 eV higher

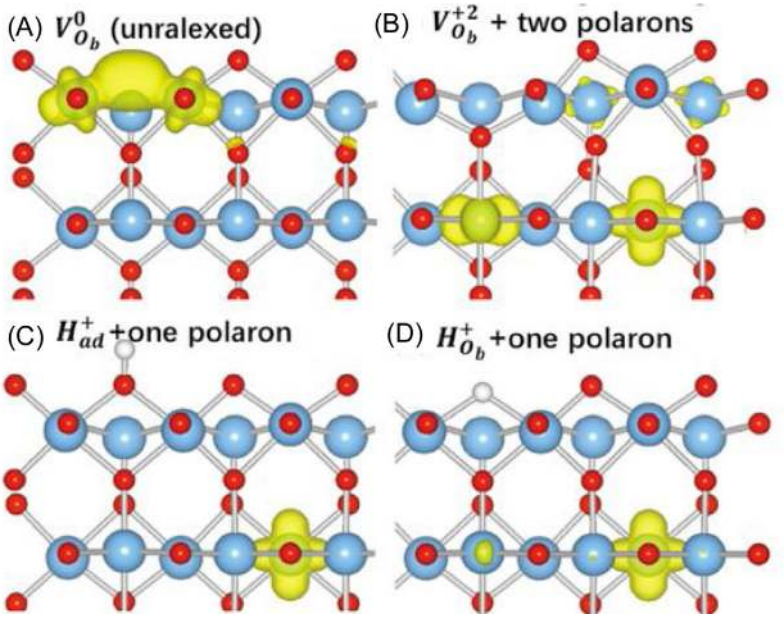

Fig. 11. Structure and charge density of donor defects and small polarons on a r-(110) surface. Large blue balls represent Ti, small red balls O, and small light gray ball H. Charge–density isosurfaces correspond to 10% of maximum charge density. (A) Unrelaxed bridging V_o in the neutral charge state; (B) bridging V_O in the +2 charge state with two associated polarons; (C) H adatom on a bridging O with associated polaron; and (D) substitutional H on a bridging O site with associated polaron.
Reproduced with permission from Ref. [197]. Copyright 2016 AIP Publishing.

in energy. By distorting the starting geometry and setting the initial magnetic moments on the Ti atoms, a partially delocalized solution was also obtained. In this solution, one electron is localized at a V_o-neighboring Ti site, and the other electron is delocalized over the CB extended states, in line with the report of Mattioli et al. (GGA + *U*) [190] and Finazzii et al. (B3LYP) [191]. It was also revealed that localization of a n-type dopant denoted excess electrons, such as from F^-, Nb, H, and the others, is almost the same as that induced by V_Os, showing some independence from chemical entities.

In addition to V_O species, the Ti(i) is another main chemical entity causing e-polaron states [192–195]. In recent research, a DFT + *U* ab initio molecular dynamics (AIMD) and a static DFT were adopted to investigate the localization of Ti(i)-induced electrons at Ti lattice sites, as shown in Fig. 10(A) [195]. It was seen by them that the average lifetime of an electron at a specific Ti site is around 0.1 ps. The most probable localization was found for the "near Ti(i)" group followed by $Ti_{2c\text{-}2nd}$ and the $Ti_{5c\text{-}lst}$ (Fig. 9(B)). The substantial population of excess electrons on deeper "near Ti(i)" sites suggested the interaction between the Ti(i) and the excess electrons. The static DFT calculation shows that $Ti_{5c\text{-}2nd}$ is more stable than other sites. One electron is trapped at the Ti(i) site, and the other three behave similarly to the ones donated by a V_O and are attracted to the Ti(i).

The bulk Ti(i)-induced e-polarons in a-TiO_2 was also studied by a B3LYP DFT calculation in other research [196]. The Ti(i) takes a quasi-pyramidal coordination with five O in lattice. Similar conclusion was obtained that one electron is localized at the Ti(i) site, and the other three are localized on regular Ti sites. The Ti^{3+}(i) spin state lies at 2.6–2.7 eV above the VB edge. These studies further concluded that the e-polarons tend to be independent on the chemical entities. The localization of Ti(i)-induced electrons in bulk a-TiO_2 and r-TiO_2 was compared by the GGA + *U* computation [189]. The Ti(i)-induced gap states dispersed along the 0.94 eV and 0.47 eV energy scale for a-TiO_2 and r-TiO_2. For r-TiO_2, the Ti atoms that the electrons reside on includes the two axial and two equatorial Ti atoms sharing a common [001] plane. The occupied orbitals on the equatorial sites have d_{xy}-like feature, whereas these on the axial sites have d_{z2}-like feature (Fig. 10(C)). For a-TiO_2, one Ti(i) induced electron is strongly localized at the Ti(i) site in a $3d_{z2}$ orbital; the other three electrons occupy three of the closest Ti sites in $3d_{xy}$ orbitals (Fig. 10(D)). 0.12 e and 0.74 e charges are found at the Ti(i) sites for r-TiO_2 and a-TiO_2 because of the different interstitial geometries in the two polymorphs.

3.1.2. *Surface electron polarons (e-polarons)*

Polaron spatial configuration on TiO_2 surfaces have attracted significant attention due to the direct relationship with charge carrier transfer. The truncation of periodicity on surface creates inequivalent Ti atoms, so different spatial localization of excess electrons is found. On the surface region, bridging V_Os ($V_{o,br}$s) and surface hydroxylation (OH_s) are the main intrinsic chemical entities that provide excess electrons. Theoretical studies have shed deep insights on the physical nature of electron localizations on the TiO_2 surfaces.

In recent research, the HSE screened hybrid functional was used to study the $V_{O,br}$ and the OH_s induced small polarons on a r-(110) unrelaxed surface [197]. The electrons are mainly localized around $V_{O,b}$ and do not lead to Ti3d gap states for an unrelaxed surface (Fig. 11(A)). However, the electrons are localized at the Ti3d t_{2g} (d_{xy}, d_{yz}, d_{xz}) orbital sets on the sub-surface layer for the relaxed r-(110) surface. The two polarons locate at the Ti atoms below a Ti_{5c} row and below the $V_{O,b}$ (Fig. 11 (B)), 0.94 and 1.3 eV respectively below the CB edge in energy, having the same spin and a $S = 1$ configuration. The average outward relaxation of the O atoms surrounding the polarons is 3% of the equilibrated Ti-O bond length. Localization of the electrons at Ti3d t_{2g} states is in good accordance with resonant photoelectron studies [198]. Two cases of H_{ad} (adsorbed on bridged O, Fig. 11(C)) and H surface doping (replacing bridged O, Fig. 11(D)) were considered for surface hydroxylation. The excess electron is stabilized as a small e-polaron located at a sub-surface Ti site below a Ti_{5c} row in the both cases, forming a gap state ~1.3 eV underneath the CB edge. The polaron spatial distribution is similar to that induced by $V_{O,Br}$, indicating the weak interaction between the donors and the induced polarons.

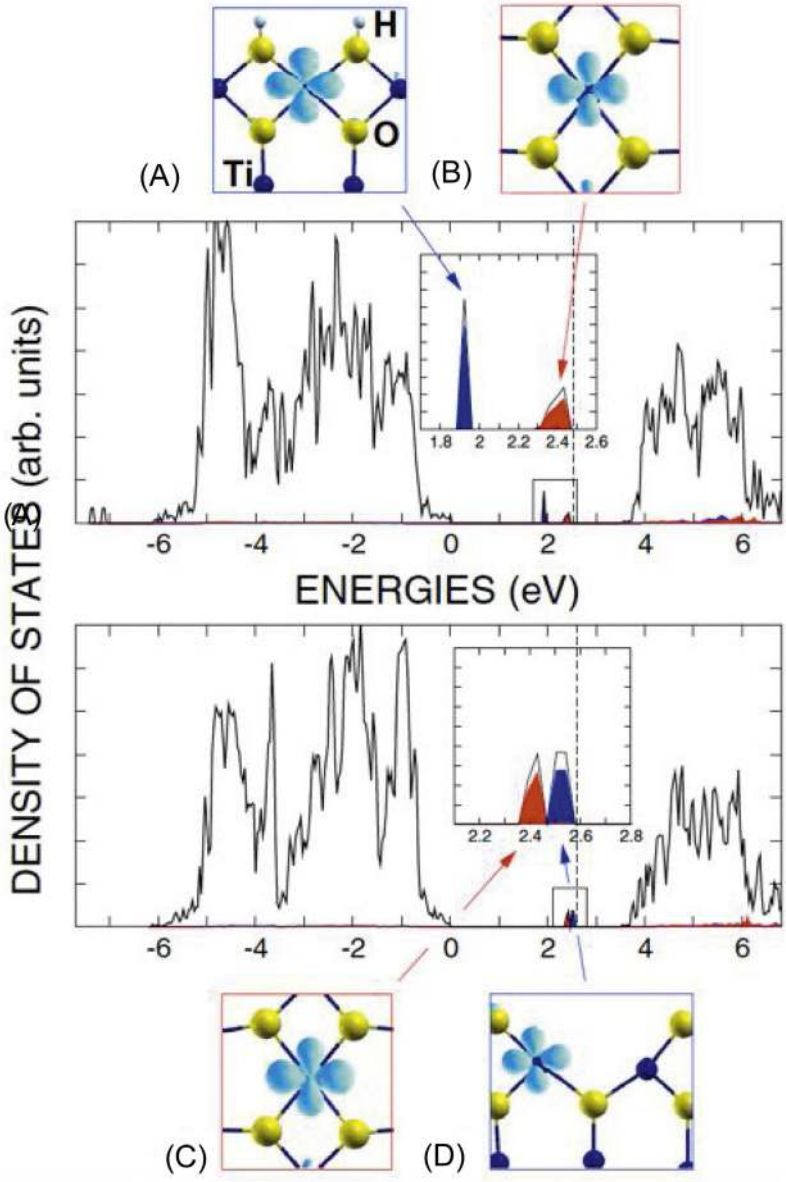

Fig. 12. Total and projected density of states for the hydroxylated (top) and reduced (bottom) r-(110) surface. The Ti^{3+} states are localized on: (A) the Ti ion between the two bridging OH groups, $Ti_{br\text{-}OH}{}^{3+}$; (D) the Ti ion nearest to the oxygen vacancy, $Ti_{br\text{-}v}{}^{3+}$; (B), (C) on a Ti_{5c} ion, $Ti_{5c}{}^{3+}$, of the surface. Spin density plots are shown in (A), (D) $Ti_{br}{}^{3+}$, and (B), (C) $Ti_{5c}{}^{3+}$. The vertical dotted line in the PDOS denotes the position of the Fermi energy. Only the majority spin component is reported.
Reproduced with permission from Ref. [199]. Copyright 2006 American Physical Society.

Spin-polarized B3LYP DFT research however has predicated a different spatial distribution of e-polarons on the reduced and hydroxylated r-(110) surface [199]. Two gap states associated with the HO_{br} induced polarons can be almost fully projected on two specific Ti atoms on the top-surface layer. One polaron locates at the Ti_{6c} $3d_{xz}$ orbital between the two OH_{br} ($Ti_{Br\text{-}OH}{}^{3+}$), 1.6 eV below the CB edge; the other locates at the nearby Ti_{5c} $3d_{xy}$ orbital ($Ti_{5c}{}^{3+}$), 1.2 eV below the CB edge (Fig. 12(A) and (B)). The structural distortion extends to the first and second neighbors due to formation of small e-polarons. This result shows that the Ti atom capped with an OH group is a good electron trap. It is also found that the two V_o-denoted electrons are also located at Ti $3d_{xy}$ and Ti $3d_{xz}$ states on the surface, lying 1.1 eV and 0.9 eV below the CBM, respectively (Fig. 12(C) and (D)); rather than localizing at the two nearest uc-Ti sites neighboring to the $V_{o,Br}$. One electron remains on a neighbored uc-Ti atom and the other moves to Ti_{5c} near the $V_{o,br}$ ($Ti_{Br,V}{}^{3+}$). Because water dissociation at the $V_{O,Br}$ generates an OH_{Br} pair, the above result also indicates that water dissociation cannot affect the polaron states that contribute to gap states, which also leads to the conclusion that the electron polarons are almost independent on the chemical entities that donate electrons [188].

A DFT+U calculation was also used to compare the e-polaron spatial population on bare and hydroxylated (OH_{Br}) r-(110) surfaces in recent research [200]. The bare surface was given one net excess electron compensated by a uniform positive background charge [201]; the hydroxylated surface was neutral and had no background charge. For the bare surface, the electron is most stable when occupying a Ti3d orbital of a t_{2g} set, which minimizes the Tid-Op orbital overlap and leads to a π^* interaction, in accordance with the ligand field theory [202]. The formation of small e-polarons is accompanied by a lengthening of the Ti-O bonds by ~0.08 Å on average. The most stable site occurs in the first sub-surface trilayer under a Ti_{5c} row. Although the presence of an OH_{Br} leads to some inequivalent Ti sites compared to a clean surface, the relative

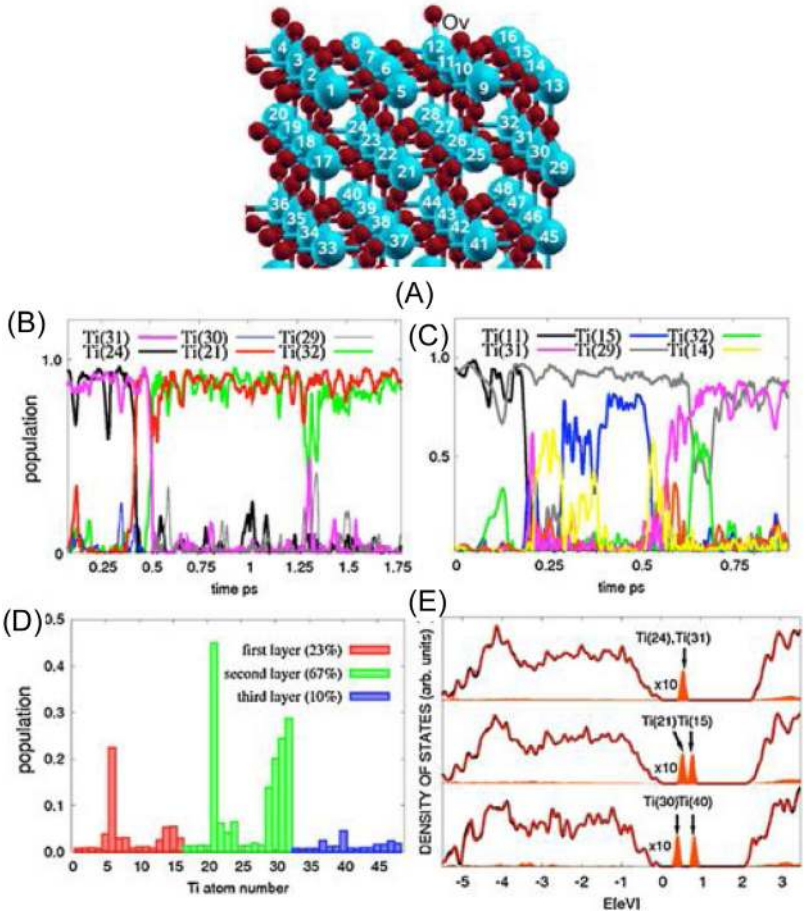

Fig. 13. (A) Ball and stick model of the defective r-(110) surface. Red and blue spheres are O and Ti atoms, respectively. (B) Dynamics of the fractional occupation of particular Ti3d orbitals during a time fragment of the simulation carried out at 1000 K; populations of about 1 and 0 correspond to Ti^{3+} and Ti^{4+} charge states, respectively. (C) Same as (B) but the charge is initially localized in the first layer at Ti(11) and subsurface at Ti(29) at 700 K. (D) Distribution function of the average population of all available Ti sites by the two excess electrons obtained from the full simulation underlying (B); inset provides layer-average populations. (E) Electronic density of states (up spins: red (black) lines), peaks in the band gap correspond to reduced Ti sites.

Reproduced with permission from Ref. [203]. Copyright 2010 American Physical Society.

energy ordering among the e-polarons at different Ti sites are similar. The most stable site also occurs in the second layer beneath a Ti_{5c} row. Because of the small effect of OH_{Br} on the polaron stability, the electron associated with an OH_{Br} is not restricted to the direct vicinity of the OH_{br}. Therefore, this computational result also supports the independence of e-polaron distribution on chemical entities. The small trapping energy differences among different Ti sites indicate the Boltzmann population of e-polarons at room temperature.

The static DFT calculation performed at 0 K cannot disclose the dynamic population of e-polarons at different Ti sites. The e-polarons would hop among different sites and follow a thermodynamic statistical distribution at a non-zero temperature. The dynamic population of V_o donated excess electrons was studied by temperature-induced GGA + *U* ab initio molecular dynamics (AIMD) in a recent research, as shown in Fig. 13(A) [203]. Two initial populations of the e-polarons induced by removing a bridging O on a r-(110) surface were considered, i.e., the localization of electrons at the second sub-surface Ti(24) and Ti(11) sites and the localization of electrons at first layer Ti(11) site and sub-surface layer Ti(29) site. The dynamic change of the statistic fractional occupation of various Ti3d orbitals showed high mobilities of electrons that visit almost all available Ti sites (Fig. 13(B) and (C)). The dominant contribution to population function arises from the second sub-surface sites which do not belong to bridged O rows (Fig. 13(D)), in good accordance with some static DFT calculations [197,200]. The dynamic electron population results in a dynamic change of the Ti3d gap states (Fig. 13(E)). The electron occupation at Ti(24) and Ti(13) exhibits a degenerated gap state, whereas it splits into two when the electrons move to Ti(21) and Ti(15), or Ti(30) and Ti(40) sites. The computed result shows that thermal fluctuation drives the excess electrons to populate various local minima in the potential energy surface of e-polaron states, and thus to explore different electronic structure topologies, leading to an average dynamic "effective delocalization".

The localization of electrons is different from surface to surface due to different chemical structures. A recent DFT + *U* calculation studied the electron localization at all inequivalent Ti sites on different surfaces of r-TiO_2 [204]. For bulk-like Ti sites, electron localization is accompanied with an average elongation Ti–O bonds by 0.08 Å. The electron spin density is localized in $3d_{x2-y2}$ orbitals. The electron localization at a r-(100) surface is highly unfavorable relative to the bulk sites. It was shown that the variation of trapping energy for different Ti sites are mainly determined by electrostatic potentials, in accordance with other research [188]. The Ti sites at the r-(001) surface have the highest affinity toward electron localization, and is accompanied with a 0.14 Å Ti–O bond elongation. Electron trapping is most favorable at sub-surface sites below Ti_{5c} rows for the r-(110) surface. The r-(101), r-(100), and r-(111) surfaces were found to repel electrons. The residence of electrons at the

Ti sites of r-(001) and r-(111) surfaces is found to be more favorable than one would expect based on an electrostatic potential energy, so the strain required to distort lattice is considered to contribute to the localization of electrons at TiO_2 surfaces in addition to the Hartree potential [196].

3.1.3. Hole polarons and hole-electron pairs

Photo-excitation generates both electrons and holes in n-type TiO_2 materials. Localization of photoinduced electrons is almost the same as the defect induced ones so they are self-localized at regular Ti sites to form Ti^{3+}-featured e-polarons [205]. The localization of photoinduced holes in the TiO_2 lattice has different features depending on bulk and surfaces. The photoinduced hole located at O2p orbital can be trapped at a lattice O site to form a h-polaron, accompanied by a lattice distortion, together they form a hole polaron (h-polaron). The h-polaron and e-polaron can bind together to generate an exciton by electrostatic attraction, which is usually called on hole-electron pair in the photocatalytic literature.

Based on a spin-polarized B3LYP hybrid functional DFT calculation, the hole-electron pair was systemically studied by Valentin et al. for both the bulk and the hydroxylated a-(101) surface cases [206]. The ground and photoinduced states were described as the lowest energy closed-shell singlet (S0) and open-shell triplet (T1) spin configurations. The electron and hole in the triplet configuration become localized after relaxation. The electron localization at a Ti site (with a d_{xy} feature) is similar to the above studies. The energy for self-trapping a single hole in bulk is as high as 0.74 eV due to the highly localization (~85%) at a single lattice O site, resulting in a typical small h-polaron. The h-polaron elongates the axial and equatorial Ti-O bonds by ~12% and ~5.6%, respectively. Full relaxation of the excited triplet state leads to self-trapping of the electron-hole pair with an energy gain of 0.58 eV. This energy is less than the sum of the self-trapping energies of the corresponding single electron and single hole, indicating the formation of an exciton. The photoinduced electron and hole are largely localized at a normal Ti site and a normal O site. The Ti-O bond in the exciton is elongated by ~3.0%.

For a clean a-(101) surface, the extra electron is localized at a Ti_{5c} site with an energy gain of 0.62 eV. The extra hole is highly localized at a bridged O with the energy gain of 1.45 eV, leading to strong elongation of Ti-O_{2c}-Ti moiety. Therefore, the Ti_{5c} and O_{2c} surface sites are better traps for photoinduced electrons and holes, respectively. For the electron-hole pair, the hole is 94% localized at a bridged O, resulting in an elongated Ti-O_{2c}-Ti bond length by 11%; the electron is 81% localized on a sub-surface Ti site, not directly connected to the surface bridged O. The e-polaron and the h-polaron induced gap states are ~1 eV below the CB edge and 2.3 eV above the VB edge, respectively. By supposing that water dissociation heterolysis produces a terminal OH and a bridged OH, the intra-pair and the split-pair configurations were considered by Valentin et al., as shown in Fig. 14(A) and (B). The hole localizes on a bare surface bridged O away from the hydroxyl groups in the intra-pair case (Fig. 14(A)). By contrast, localization of the hole in the O of Ti-OH_t groups is preferred in the split-pair case (Fig. 14(B)) with a trapping energy of 0.95 eV. For the hole-electron pair, the hole is localized at a bare bridged O atom, with the electron being at the neighboring Ti site for the intra-pair case. By contrast, the electron and hole are localized at the Ti atoms and the O atoms of the Ti-OH_t group in the case of the split-pair OH_s, forming a strongly bound exciton trapped at Ti-OH_{br}. The one-electron energy level associated with the Ti^{3+} ion is 1.24 eV below the CB edge, and the hole state associated with the (OH_t is 2.67 eV above the VB edge. This calculation result supports the hypothesis that the hydroxyl free radical ((OH) is the main reactive oxidation species in photocatalysis.

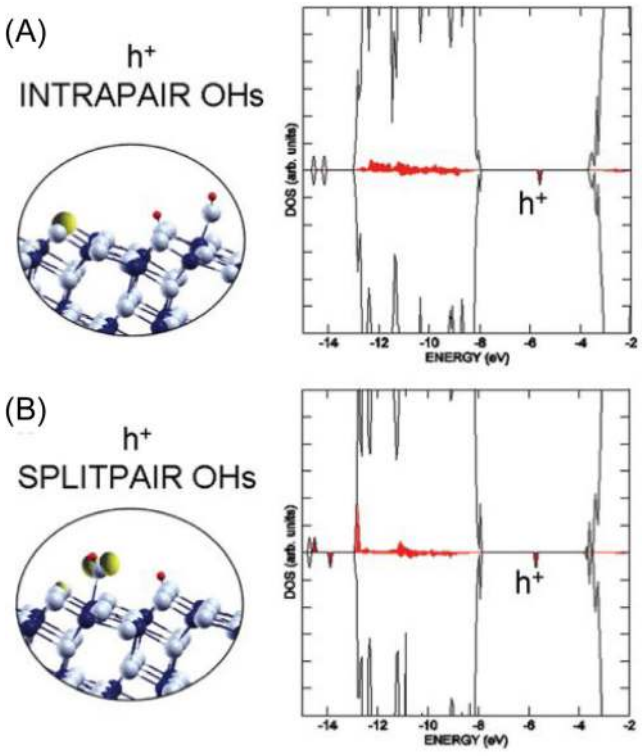

Fig. 14. Spin density contours and total and projected density of states of one extra hole on the hydroxylated a-(101) surface: (A) intrapair and (B) splitpair. Projection is onto the trapping atomic species (O_{2c}^- or (OH_t). Black and gray spheres represent Ti and O atoms, respectively. Small spheres represent H atoms.

Reproduced with permission from Ref. [206]. Copyright 2011 American Chemical Society.

3.1.4. Charge carrier localization at nanoclusters and boundaries

The valency of Ti atoms on a perfect TiO_2 surface are either 5 or 6 coordinated. Tetrahedral (4-f) or lower coordinated Ti sites commonly exist on nanocluster surfaces [207], step edges/corners [208], and boundaries [209]. The local chemical environment induced by a lower coordination is different from a normal surface, hence altering the localization of excess electrons. It is shown that Ti_{4c} sites are critical active sites for CO_2 reduction [210]; the low coordinated Ti edge/corner sites can also promote water dissociative adsorption [211]; the low coordinated sites are also important for the charge carrier kinetics because of their roles in effectively trapping the photoinduced electrons and holes.

In recent research, TiO_2 nanoclusters generated from a Monte Carlo low energy search [212–214] were used to study the localization of photoinduced electrons and holes at the singly coordinated terminal titanyl O, 3- and 4-f Ti atoms by a DFT computation, as shown in Fig. 15 [212]. In all nanoclusters, the electron is localized at the Ti3d orbital of a single Ti_{3c} or Ti_{4c} sites and tends to form Ti^{3+} species due to high electron localization, and accompanied with a Ti-O bond elongation. Except for the Ti_4O_8 and $Ti_{30}O_{60}$ nanoclusters, the hole is strongly localized at the titanyl O with a high e-magnetization, also accompanied with a Ti-O bond elongation that is in line with a small h-polaron. The hole is spread over two O_{2c} atoms in Ti_4O_8, whereas it spreads over a single O and its nearest O_{2c} neighbor in $Ti_{30}O_{60}$. The strong localization of an electron and a hole at uc-Ti and uc-O indicates that sub-nm nanoclusters are important in designing novel photocatalysts. It was also reported that low chemical coordination also causes the empty Ti_{3c} 3d-featured gap states at the edge of anatase $(TiO_2)_{38}$ stoichiometric clusters [215], partially due to the effective sub-nanocluster on overall cluster edges.

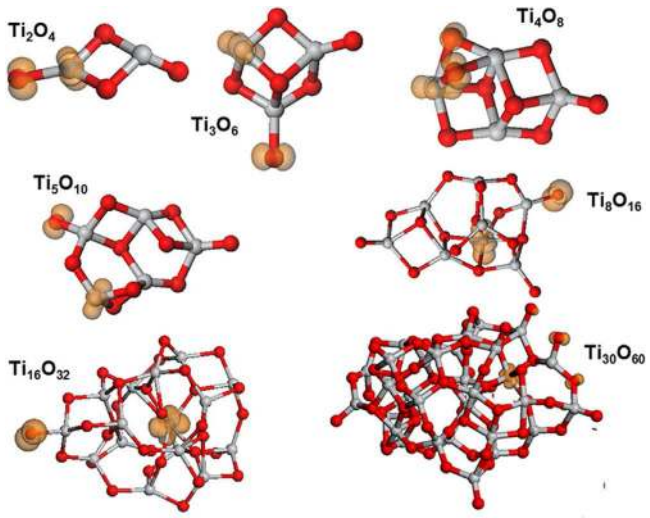

Fig. 15. Spin density plots for the free TiO_2 nanoclusters in the excited state. The spin density isosurfaces are orange and enclose spin densities of up to 0.2 eV/Å^3. Reproduced with permission from Ref. [212]. Copyright 2014 American Chemical Society.

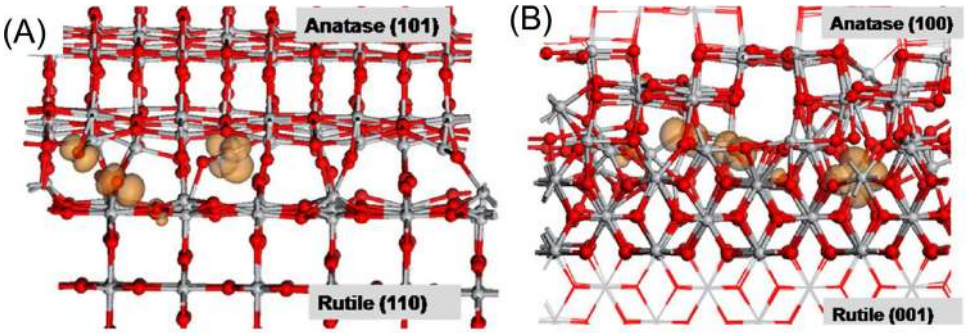

Fig. 16. (A) Spin density plot of the interface in the triplet model for the r-(110)/a-(101) interfacial structure. (B) Spin density plot of the interface in triplet model for the r-(001)/a-(100) interfacial structure. Spin density isosurfaces enclose volumes of up to 0.02 eV/Å^3.
Reproduced with permission from Ref. [216]. Copyright 2016 American Chemical Society.

Low-coordination number Ti and O atoms are also prevalent at boundaries due to lattice mismatches and strains. DFT studies provide some meaningful points for spatial distribution of polarons at boundaries. Deskins et al. firstly used near coincidence lattice theory (NCSL) to construct r-(110)/a-(101) (Fig. 16(A)) and r-(001)/a-(100) (Fig. 16(B)) boundaries; these two boundary models were then used for DFT + U computations [216]. A disordered interfacial region is present at the a-TiO_2/r-TiO_2 junction after geometrical relaxation. The r-(110)/a-(101) interfacial region contains full-coordinated Ti atoms, Ti_{5c} atoms, and Ti_{4c} atoms. The calculated results show that the electron is localized at a Ti_{4c} site originally coming from the a-TiO_2 phase for a r-(110)/a-(101) interface, resulting in a Ti3d-featured e-polarons with a Ti-O bond elongation. The hole spreads over two interfacial O atoms (Fig. 16(A)) originating from the a-TiO_2 and the r-TiO_2, respectively. The partial localization of a hole over two O atoms is accompanied with a Ti-O bond elongation, showing the formation of a h-polaron. For the r-(001)/a-(100) interface, the electron is localized on a Ti site originating from the r-TiO_2, while the hole spreads over two interfacial O atoms originating from the r-TiO_2 (Fig. 16(B)). The significant relaxation within the interface plays a determining role in the eventual location of the electron and the hole.

The charge carrier localization in a large r-(001)/a-(100) boundary was also studied by a DFT calculation (Fig. 17(A)) [217]. Similarly, the r-(001)/a-(100) boundary region also contains Ti_{4c}, Ti_{5c}, and Ti_{6c} atoms. The result shows that the boundary region contributes to a gap state arising from electron localization at these Ti sites. Several electrons are localized at some Ti_{5c} sites (Fig. 17(B)) with a large e-spin density; much less electron density is observed on other type Ti atoms. It was also found that the mere presence of Ti_{4c} atoms cannot guarantee electron localization at Ti_{4c} sites because not all Ti_{4c} atoms can localize electrons; this shows that electron localization is dependent on structures. For a slab having a net charge of -1, the Ti_{4c} sites have a strong ability to localize the electrons even without a U correction. The co-existence of an interface and a surface was also modeled by adding a vacuum layer on the r-(001)/a-(100) slab (Fig. 17(C)). The computation results show that the unpaired electrons are more stable within the surface boundary region than the pure phase alone. Fig. 17(D) shows the Ti atoms in the boundary region and the spin density isosurfaces containing the spin-up and spin-down electrons, which shows that the main localization of electrons are on the Ti_{5c} and Ti_{4c} sites. The lattice distortion also seems to favor the stability of unpaired electron on these uc-Ti atoms.

In other work, the spatial and energetic distribution of electronic states in the (101) and (001) paired nanoparticles were calculated by hybrid DFT, GGA-DFT or DFTB calculations [218]. Fig. 18 shows the truncated bipyramidal particle ((A)-a) with the constructed paired particles attached on (001) and (101) facets ((A)-b and (A)-c). Different from the above interfaces, the (001)/(001) and (101)/(101) interface does not include the uc-Ti and uc-O. However, the calculation results still showed the localized gap states with energies

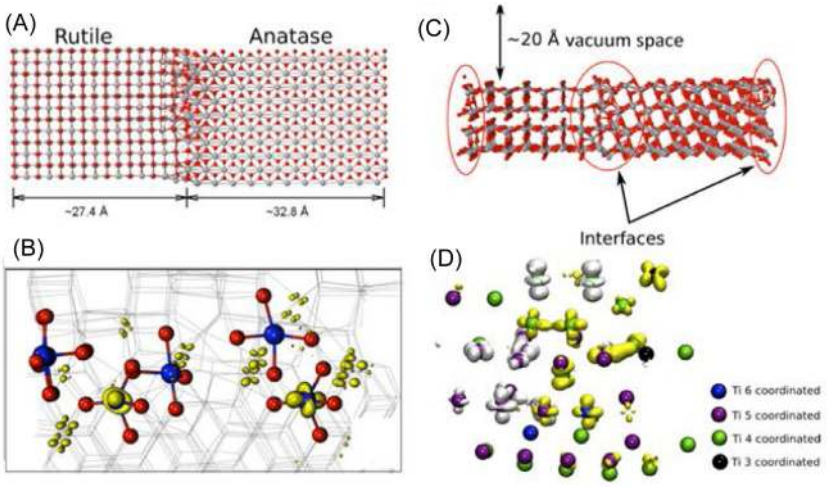

Fig. 17. (A) Slab model of the interface between bulk materials formed by bringing together the r-(001) and a-(100) surfaces. The red spheres represent O, the gray spheres represent Ti. The vacuum region is along the x direction and extends ~20 Å beyond the edges of the r-TiO_2 and a-TiO_2 materials. (B) Electron spin density plot of electrons localized in the 3d orbitals of Ti_{5c} atoms in the interfacial region for a neutral slab. (C) Slab model of the mixed phase exposed surfaces. Two interfaces exist for this slab and the a-TiO_2 and r-TiO_2 surfaces are both exposed to vacuum, including the interfacial region. (D) Electron spin density plot of the interfacial region for a slab with vacuum-exposed surfaces.

Reproduced with permission from Ref. [217]. Copyright 2015 AIP Publishing.

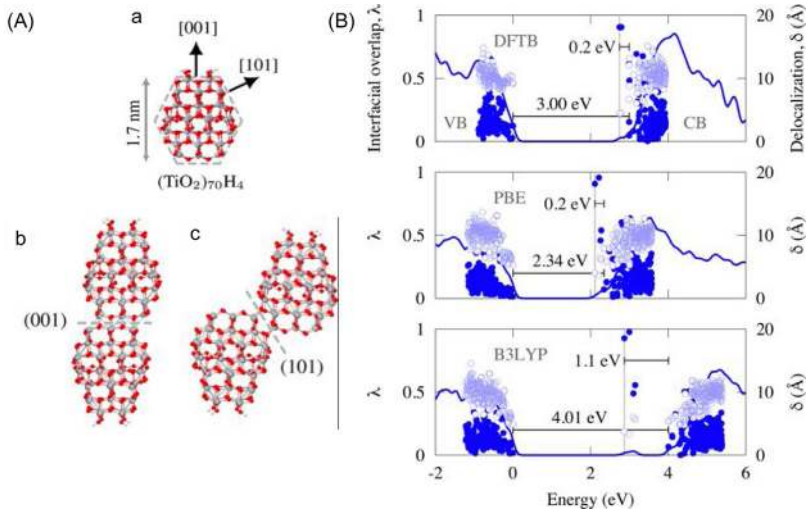

Fig. 18. (A)-a Truncated bipyramidal particle used to construct the two systems. (A)-b paired particles attached on (001) facets. (A)-c Paired particles attached from (101) facets. Ti, O, and H atoms are red, gray, and white, respectively. Comparison of calculations from three levels of theory (DFTB, PBE, and B3LYP//PBE) on the paired particles attached on (001) facets. Each plot includes the DOS curve and values of λ (filled markers) and δ (open markers) from the highest 200 occupied and lowest 200 unoccupied canonical orbitals. The predicted band gap and the depth below the CBM of the lowest excess electron are reported.

Reproduced with permission from Ref. [218]. Copyright 2017 American Chemical Society.

near the CB edges. All the hybrid DFT, GGA-DFT and DFTB calculations revealed that the gap states are localized at a (001)/(001) interfacial at a deeper position in energy than the gap states localized at a (101)/(101) interface between the same two particles. The trap depth predicated by hybrid DFT (1.1 eV below the CB edge) is deeper than that predicated by DFT and DFTB (~0.2 eV below the CB edge), as shown in Fig. 18(B).

3.1.5. Localization of electrons and holes at TiO_2/aqueous interface

Photocatalytic reactions and photoelectrochemical processes usually involve TiO_2/water interfaces. The presence of aqueous water has a great effect on the spatial localization of charge carriers on TiO_2 surfaces. The aqueous a-(101) surface consists of a first layer of interacting adsorbed water molecules on Ti_{5c} sites and a second layer of molecules bonding with bridged O atoms by H-bonds [219]. In recent research [220], the dynamic localization of H ad-atom donated electrons at a solvated a-(101) interface [221] was studied by a DFT + U FPMD method [222]. The computation results show that the electron is subject to a localization at surface Ti_{5c} sites next to the OH_{br} (Fig. 19(A)); this is different from the DFT + U studies of an a-(101)/vacuum interface. A bulk impurity (Nb) was also involved to gain an insight into the effect of aqueous water on electron localization because its attraction potential limits the electron movement to the surface. The results show that the electron is highly mobile and tends to spread over several Ti sites when the slab is in vacuum (Fig. 19(B)), whereas it rapidly reaches the surface because of the trapping by water dissociation when the system is solvated (Fig. 19(A), (C), and (D)). Reducing the U value does not affect the main electron localization at surface Ti sites associated with a solvated water dissociation (Fig. 19(C) vs. Fig. 19(D)). When a bulk Nb dopant is present, the surface layer can

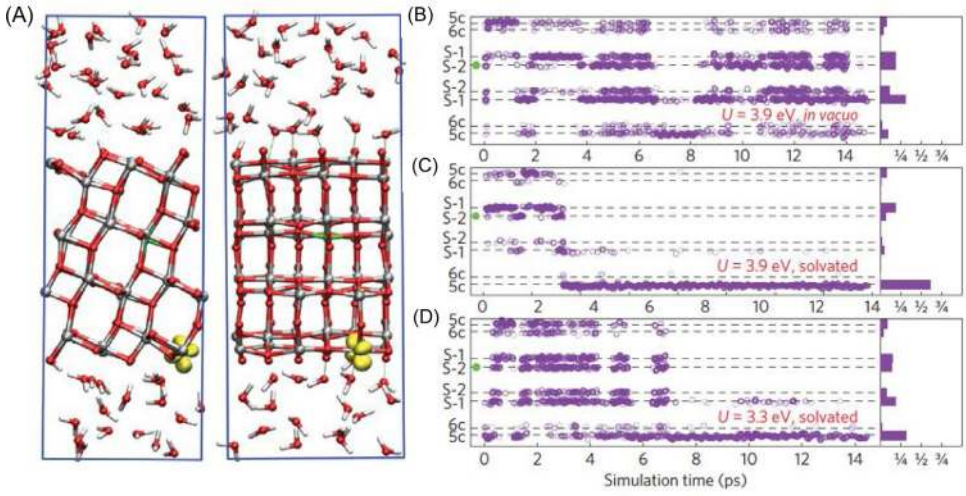

Fig. 19. FPMD simulations of Nb-doped a-(101) surface. (A) Side views of a Nb-doped a-(101) slab immersed in water from two different perspectives. Nb is shown in green. (B)–(D) Statistics from FPMD simulations at 400 K with different *U* values and environments. Left panels show the location of the excess electron in the direction perpendicular to the surface during the simulation, and the right panel corresponds to distribution. Layers below the surface are labeled S-1 and S-2, and the green circle marks the layers with Nb atoms.

Reproduced with permission from Ref. [220]. Copyright 2016 Nature publishing.

feel the attractive potential of both Nb and OH_{Br} in a thinner slab, resulting in favorable surface localization. In the thicker layer that the Nb impurity is several layers away from the aqueous interface, electron localization to form a large bulk polaron is more favorable. This electron associating with a shallow impurity below the surface are unlikely to form a trapped surface Ti^{3+}-OH_{br} species. It was shown that the electron strongly avoids the hydroxylated a-(001) surface and tends to remain in sub-surfaces and inner layers. The electron forms a quasi-2-dimensional localized state within an a-(001) plane that dynamically switches from one plane to another. They suggested that this 2-dimensional electronic state should be delocalized rather than form a large polaron. Higher energy of the surface 5-f Ti3d atoms in a-(001) prevents the electron from residing on a-(001) surface. Therefore, it is concluded that the a-(001) surface is strongly repulsive for electrons and attractive for holes in an aqueous solution, in line with the conclusion that a-(001) surfaces play the role of oxidative surfaces in photocatalytic reactions [223–225].

In addition to electrons, the localization of holes at TiO_2 aqueous interface was also studied by using a Born–Oppenheimer first principle MD based on the HSE06 hybrid functional [226]. The r-(110) aqueous interface was modeled on a TiO_2 tri-layers slab solvated with water molecules. An electron and a proton are simultaneously removed to simulate hole trapping. It was shown that the initial extended hole is quickly localized at a lattice O site in the bulk, instead of a surface O_{2c} site or the terminal OH_t, not in agreement the static DFT calculation [215]. The hole density must be increased by further de-hydrogenating water molecules to obtain a surface trapped hole. When creating four holes, one hole can be trapped on the surface with the other three localized at lattice O atoms in bulk. The hopping of a bulk trapped hole is a fast process with small activation energy and the statistical population of h-polarons at different sites can be reached [227].

3.1.6. Defect-polaron and polaron–polaron interactions

The above studies focus on the electron localization at normal lattice Ti sites and the associated e-polaron states. Contributions of polaron-defect and polaron–polaron (p-p) interactions were considered to be low. A recent DFT study showed that such interactions cannot be ignored [228]. The bi-polaron associated with a $V_{O,Br}$ was proposed to exist at a r-(110) surface. The spatial relations between

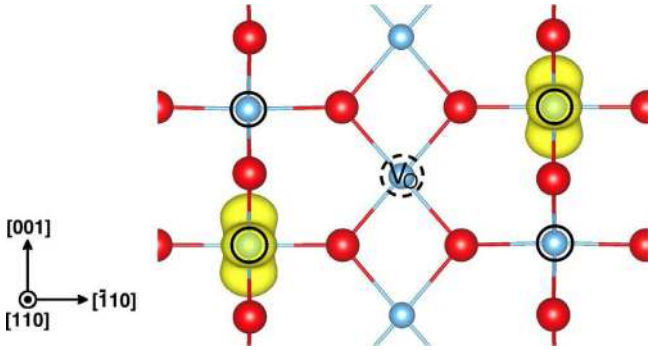

Fig. 20. Top view of neutral V_O surface. Here, only the second layers shown. Stable position of polarons and its symmetrically equivalent position are indicated by solid black circle. Two of them are already occupied by polaronic states (yellow). The dotted black circle shows the location of V_O.

Reproduced with permission from Ref. [228]. Copyright 2014 American chemical Society.

the polaronic sites and the $V_{O,Br}$ were calculated. In the case of an $V_{O,Br}$ with a near bi-polaron (p-p distance is 7 Å), the energy for the p-p interaction is calculated to be ~0.24 eV. The p-p interaction is ~0.23 eV when the bi-polarons is far away from a $V_{O,Br}$. The two polarons are electrostatically repulsive regardless of their distance to a $V_{O,br}$. The $V_{O,br}$-one polaron interaction is ~0.43 eV lower in energy, implying an attraction between them. Three-body interaction involving two polarons and a $V_{O,Br}$ was also studied by considering four configurations: (1) two polarons near a $V_{O,br}$, (2) one polaron near a $V_{O,Br}$ and one polaron far away, (3) two polarons far away from $V_{O,Br}$, (4) two polarons, infinitely separated and far away $V_{O,Br}$. The three-body interaction of case (1) has the lowest energy. The interaction energy of cases (2), (3), and (4) are ~ 0.19 eV, and ~0.85 eV, and 0.62 eV higher relative to the case (1). The competition between the $V_{O,Br}$–polaron electrostatic attraction and the p-p electrostatic repletion determines the energy stability of the two-body and three-body configurations. For all configurations, this research showed that the contribution of lattice distortions is very low. The $V_{O,Br}$ attracts a pair of polarons (one equivalent configuration) as shown in Fig. 20, a bipolaron, with an energy of ~0.85 eV, is the energetically most stable.

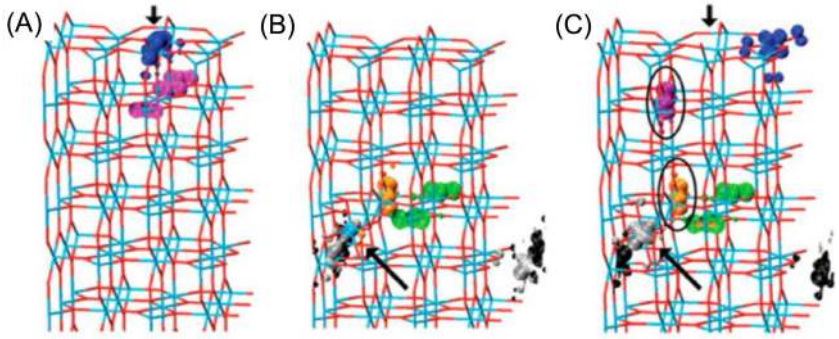

Fig. 21. Electronic charge density distribution in the 8 tri-layer r-(101) slab systems. (A) $V_{O,Br}$, (B) one Ti(i) between the fourth and fifth trilayers, (C) $V_{O,Br}$ modeled together with one Ti(i). Blue intersections indicate Ti atoms and red intersections O atoms. Ti(i) is shown as a blue sphere. The positions of $V_{O,Br}$ and Ti(i) are marked by the black arrows. Different colors have been used to distinguish between Ti(i)-donated (black, gray, green, orange), and surface $V_{O,Br}$ induced (purple, blue) states.
Reproduced with permission from Ref. [103]. Copyright 2010 National Academy of Sciences.

It is natural that both V_O and Ti(i) can commonly exist in TiO_2 materials; this leads to the interaction between the V_O-denoted electrons and Ti(i)-denoted electrons. It was seen that the number of adsorbate O (on Ti_{5c}) caused by O_2 dissociation is much higher than that predicated by a V_o-mediated mechanism, showing that more electrons than expected than V_os are initially present [229]. Therefore, it was proposed that more electrons localized at surfaces are induced by bulk Ti(i) species [179,230]. The DFT (LDA + U) calculation was performed to study the interaction between the V_o-induced and the Ti(i)-induced electrons in recent research [103]. The electrons are systemically at or immediately beneath the $V_{O,Br}$ in the case of isolated V_O (Fig. 21(A)). An asymmetric electron localization at the Ti(i) site and on other separate regular lattice sites (Fig. 21(B)) was obtained for an isolated bulk Ti(i), also correlating with another study [231]. Coupling between the $V_{O,Br}$- and the Ti(i)-denoted electrons is evidenced by the large change of electron localization spatial distributions. The presence of the Ti(i)-denoted electrons induced an electronic reorganization moving the electronic charge away from the $V_{O,Br}$ site and the corresponding O_b row (Fig. 21(C)). Hybridization makes the Ti(i)-denoted electrons available at the $V_{O,Br}$ site thus locally charging $V_{O,Br}$ with the electrons necessary to account for the additional adsorbed O_2, the same mechanism is also suggested for the interaction between the electrons denoted by Ti(i)s and OH_s.

3.2. Experimental studies of charge carrier localization

3.2.1. Polaron states

In addition to theoretical calculations, recent studies show that the localization of charge carriers on TiO_2 surfaces and in bulk can be seen in experiments; this provides direct proof for e-polaron formation. Because natural TiO_2 materials belong to n-type semiconductors, experimental studies mainly have focused on electron localization at Ti sites. The experimental techniques used to observe e-polarons include resonant PE diffractions (RPED), atomic-resolution STM (AR-STM), and EPR.

PE diffractions are used for recording the photoelectrons localized at different Ti3d-derived states associated with surface and subsurface sites, and featured a Ti-2p-3d resonance excitation that can strongly enhance the defect state PE [232]. The electron localization on the r-(110) surface of a single crystal that contains bridging V_O atoms was studied by this method [233]. RPED pattern was recorded for the PEs from gap states (e-polaron) at Ti-*L2* resonances ($h\nu = 462$ eV). The PE intensity (I) was firstly obtained as a function of polar angle θ and azimuthal angle ϕ, and then RPED patterns were plotted from the azimuthal anisotropy function over (θ, ϕ), as shown in Fig. 22. The positions of all major diffraction peaks (bright spots) agree well with the interatomic directions from the Ti sites. The peak positions of gap states associated with PED patterns match well the interatomic directions of Ti1-O1, Ti3-Ti2, and/or Ti4-Ti1, as well as Ti3-O2 (Fig. 22(A)). The PED patterns for emission from the six inequivalent Ti sites on the first three TiO_2 layers (marked in Fig. 22(A)) are labeled in Fig. 22(B); this shows that the inequivalent localizations of electrons at different Ti sites. The RPED for emissions from the six inequivalent Ti sites on the first three TiO_2 layers were modeled by including different Ti atoms. The models involving Ti1 to Ti4 (model1-4) and Ti1 to Ti6 (model1-6) fit well with the experimental results. The model1-4 predicted that more than 60% of the charge is localized at the Ti3 site. Molel1-6 predicts that nearly 35% of the charge localizes at the Ti3 sites and more than 25% of the charge localizes at the Ti5 sites. Therefore, the observed electron localization at the sub-surface sites was is in good accordance with the theoretical calculation [158]. The modeling also shows that Ti(i) entities are the minority defects at reduced r-(110) surface because Ti(i) denoted electron localization does not accord with the experimental results. The RPED was also used to study the difference between the localization of electrons denoted by surface sodium dopants and bridging V_O species [234]. The spatial distribution of electrons demonstrates the close similarity between the sodium and bridged V_o denoted e-polarons, in addition to the same conclusion that the excess electrons mainly reside on sub-surface Ti atoms [233]. These results show that the e-polaron spatial distribution is an intrinsic property of a r-(110) surface, independent of the way in which the excess electrons are introduced, also agreeing well with the theoretical analysis [197].

Some theoretical studies indicate the easy formation of e-polarons in r-TiO_2 [235], whereas the electrons in a-TiO_2 prefer in free states or large polarons [236]. The different electron localizations were also observed in experiments by a low temperature atomic-resolution STM on r-(110) and a-(101) surfaces, and a similar conclusion was drawn [237]. The empty-state STM images of r-(110) and a-(110) surfaces is shown in Fig. 23(A) and (B), respectively. Sub-surface V_o species were pulled to the top-surface by a STM tip [127,156]. The bright spots at a dark O_{2c} row marked with circles and arrows indicate the bridging V_O species. The filled local density of states (LDOS) at V_O sites is small for r-(110) surface (Fig. 23(C)). Most of the current comes from Ti rows, and becomes more apparent when scanning at very close tip-sample distance (lower part of Fig. 23(C)). In contrast, the electrons stay around the V_O, sites at a-(101) as suggested by the vanishing LDOS at rest of the surface (Fig. 23(D)). The line profiles (Fig. 23(E) and (F)) along the lines in Fig. 23(A) and (B) clearly confirmed the results. By combining this information with a molecular dynamic (MD) simulation, it was demonstrated that the e-polarons mainly locate at the subsur-

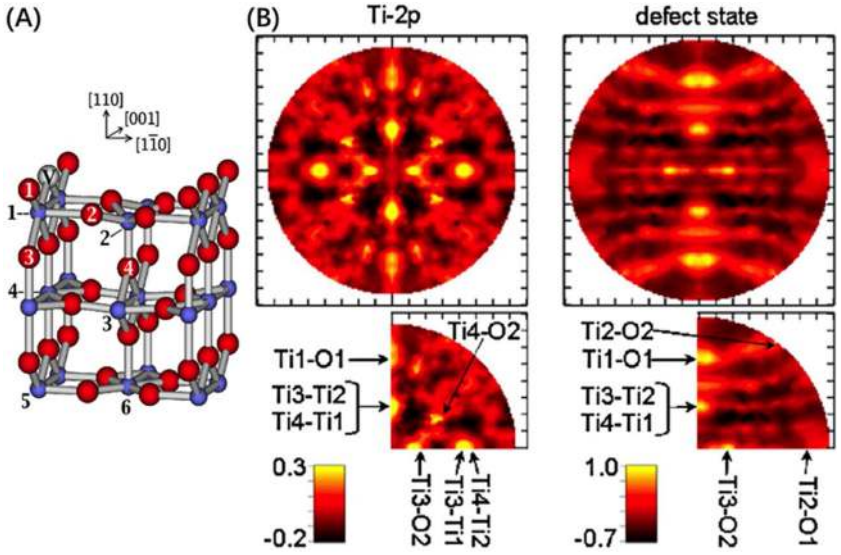

Fig. 22. (A) Ball and stick model of the r-(110) surface. Big red (small blue) balls are O (Ti) atoms. Vindicates a bridging oxygen (O1) vacancy. (B) Experimental photoelectron diffraction (PED) patterns $\chi(\theta,\phi)$. Left: Standard PED from the Ti-2p3/2 core level. Right: Resonant PED from the defect state. The projection is linear in θ with the surface normal ($\theta = 0$) in the center. Ticks are drawn at every 10°. $\phi = 0$ ($\phi = 90$) is found at 3 o'clock (12 o'clock) and corresponds to the [11–0] ([001]) direction.

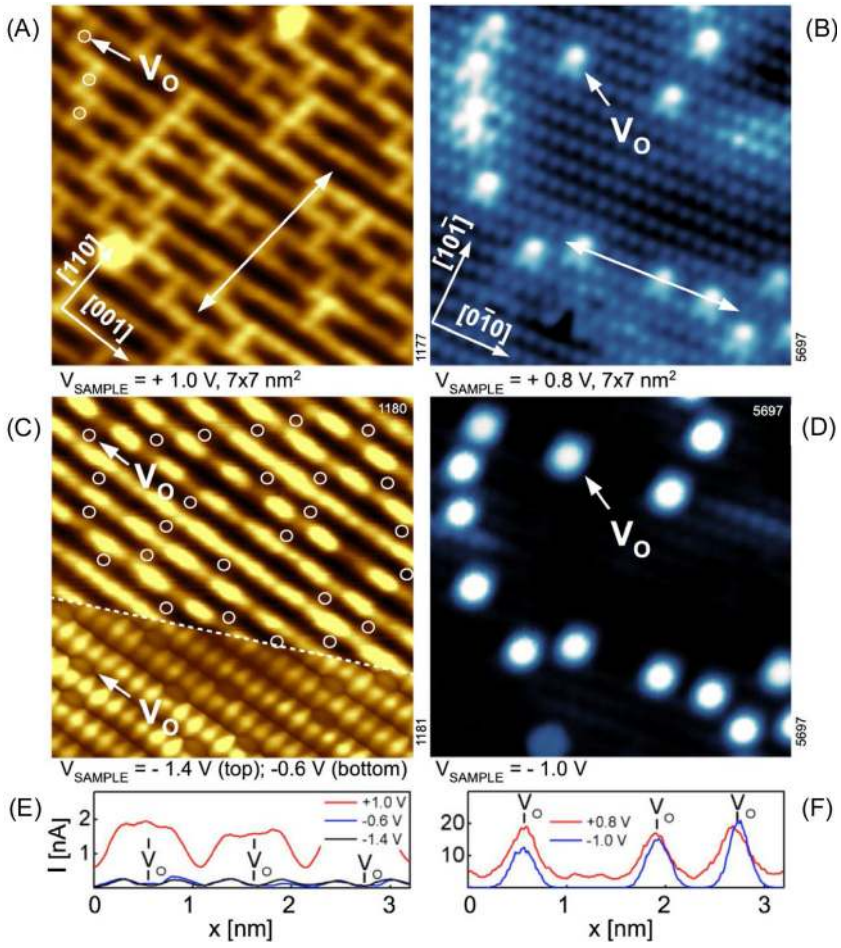

Fig. 23. Local electronic structure of r-(110) (left) and a-(101) (right) surfaces doped by surface O vacancies. Constant-height scanning tunneling microscopy images of r-(110) (A), a-(101) (B) empty states and (C), (S) filled states of the same areas. V_O marks surface O vacancies; they are also marked with circles in (C). (E), (F) Line profiles along the lines in (A) and (B), respectively.

face layer of r-(110), whereas the V_O species on a-(101) give rise to the immobile electrons pinned at Ti sites just near the V_O.

In an a-(101) sample containing ~1% Nb dopants, fairly extended bright regions (dashed rectangle) can be seen in the STM image, as shown in Fig. 24. Spatial STS images revealed a peak at (-40 ± 10) meV and the absence of any gap state at −1 eV. The bright regions are stable in time and do not migrate at temperatures ranging from 6 to 78 K; this suggests that the electron is stabilized at positively-charged sub-surface donors, most likely the Nb. It is proposed that the couple of the ionized donors and the lattice periodic potential creates quantum wells in which the electron occupies a single energy level. The electron wave function spreads over several unit cells around the donor and the anisotropic density distribution in STM images agree well with Frohlich's model for large polarons [238]. However, this state cannot move through the crystal like a true large polaron as predicted in theoretical calculations; this is different and the formation of e-polarons remains favorable for a Nb-doped r-TiO_2 because of its semiconductor-like conductivity [239]. The difference is attributed to the different stackings of octahedral coordinated Ti atoms in the two polymorphs. The resulted differences in electronic structure around the CB edge provide for a higher energy gain upon small polaron formation in r-TiO_2 than a-TiO_2.

The above research showed that the unfavorable formation of small e-polarons at the a-TiO_2 (101) surface. However, the photoemission always presents a significant gap state ~1 eV below the Fermi level, characteristic of a localized electron. it was revealed by Setvin et al. that the trapped electrons are located exclusively at the step edges of the a-TiO_2 surface by spatially resolved experimental techniques (STM, and scanning tunneling spectroscopy (STS)) [240]. Fig. 25 shows the STM and STS of an a-TiO_2 surface at negative bias voltage (filled states). The clean surface is almost free of localized density of states (LDOS). However, the STS spectra taken close to the steps, termed A, B, and C (Fig. 24(A)) show a significant LDOS within the band gap with a maximum peak ~1 eV below the Fermi level, similar to the photoemission spectrum. These gap states are directly at and up to two lattice constants away from the step edge at both the upper and lower terrace. However, the STS induced by surface V_o on a-TiO_2 (101) (dashed line) is completely different.

The spatial configurations and mobilities of small e-polarons on r-(110) surfaces were further observed by a STM study [242]. Yim et al. provided the evidence for e-polaronic features associated with bridged V_O species on a r-(110) surface at low temperatures. The empty-state STM image recorded at 78 K shows the presence of a V_O species on a bridging O row (Fig. 26(A)). The filled-state STM images of the isolated V_O depend on the recorded temperatures (Fig. 26(B)–(F)). At 78 K, all the V_O species have a four lobe electron distribution and featured a 2 mm mirror symmetry in the [001] and [$\bar{1}$10] directions around the bridging V_Os (Fig. 26(B)). Reducing the recorded temperature can change the electron distribution. At 16 K, although the electron distribution retains a four-lobe structure (Fig. 26(C)), two of the lobes appear much brighter, and the original mirror symmetry is broken. The symmetry still exists at 7 K (Fig. 26(D)–(F)), but only two bright lobes are present and these are oriented either directly across the row (Fig. 26(D)), along the row (Fig. 26(E)), or diagonally across it (Fig. 26(F)). Two e-polarons can be formed by one bridging V_O; they present as a four-lobe structure at 78 K and are reduced to two lobes at 16 K. This observation shows two defining properties: (1) polaronic trapping of electrons onto multiple local structural minima associated with their presence at different lattice sites; (2) thermally-activated hopping of polarons among different lattice sites. In contrast to charge carriers occupying delocalized states that are independent on temperature, the diffusion of self-trapped carriers increases with temperature.

Fig. 26(B)–(F) shows that the e-polarons are constrained to hop around the V_O site due to the electrostatic interaction with the positively charged V_O, which is also in line with a DFT study [227], but is opposite to a DFT + U study [197]. By assuming a 24 meV thermal barrier for the e-polaron hopping, the hopping frequency at 78 k is one thousand times higher than 7 K. Given that the timescale of the STM scans is in minutes, the spatial configuration of electrons around an isolated V_O at 78 K can create a perfect isotropic environment to be representative of a thermal population equilibrium among different structural local minima. On the other hand, the electronic distribution at 7 K is expected to arise from kinetic trapping of e-polarons in one of a number of symmetrically equivalent configurations. This asymmetric configuration also represents the sole ground state; the polaron distribution relaxes back to this sole ground state rather than being kinetically trapped in one of a number of degenerate ground states following STM manipulation pulses. It is observed that the e-polarons also accordingly move with the position displacement of a bridged V_o species manipulated with a STM tip, so as to remain their locations relative to the bridged V_O unchanged.

The localization of an electron onto Ti^{4+} site results in an unpaired Ti3d-featured e-polaron. Ti^{3+} ions belong to the paramagnetic centers for electrons that can be detected by EPR [243–245]. By using a reduced r-TiO_2 single crystal that contains Fe^{3+} and Cr^{3+} ions, the intrinsic small e-polarons localized at Ti sites were identified by an EPR study [246]. Sub-bandgap photons (442 nm laser) were used to excite electrons from the Fe^{3+} and Cr^{3+} dopant levels to the CB states of TiO_2. The electrons entering the CB states are then self-localized at regular unperturbed Ti sites at very low temperature. The photoinduced EPR spectrum shown in Fig. 27(A) presents the line at 340 mT representing the small e-polaron, i.e. the self-trapped electrons at regular Ti^{4+} lattice sites to form Ti^{3+} signals. The thermal stability of small e-polarons is so low that it can only be observed under low microwave power at temperatures below 20 K. The unpaired electron occupies the $|xy^2\rangle$ Ti3d orbital (d_{xy}) (Fig. 27(C)), where *x* and *y* are in the equatorial plane in a TiO_6 octahedral and y is in the [001] direction (Fig. 27(B)).

3.2.2. Optical transition of polarons

Ti ions occupy slightly distorted octahedral voids in TiO_2. The crystal field effect splits Ti3d orbitals into two distinct groups, a lower set of three orbitals (d_{xy}, d_{yz}, and d_{xz}) with a t_{2g}-like symmetry and an upper set of two orbitals (d_{x2-y2} and d_{z2}) with an e_g-like symmetry, as shown in Fig. 27(C). In stoichiometric TiO_2, the t_{2g}-like orbitals contribute mainly to the states near the CB edge. The excess electrons are localized at the t_{2g} orbitals on the hydroxylated or reduced r-(110). The t_{2g} configuration can also lead to a Jahn–Teller distortion to the Ti^{3+} states; this effect further splits the three t_{2g} orbitals into a low energy state with d_{xy} character and two high energy orbitals with d_{yz} and d_{xz} characters. The excess electrons donated by reduced defects fill the d_{xy} orbitals and give rise to the occupied polaronic state in band gap as summarized above. The d_{yz} and d_{xz} orbitals moving to a higher energy can give rise to the excited resonance at ~2–3 eV above the Fermi level. Therefore, the d_{yz}, d_{xz}, and d_{z2} states are regarded as the resonant excited localized states of d_{xy} gap states, which remain fairly localized despite being resonant. The transition of localized electrons from d_{xy} gap states to their resonant excited localized states has been identified in a two-photon photoemission spectroscopy (2PPE) study [247]. It was shown that the d-d excitation of localized electrons can also occur under illumination with visible photons, thus playing the important role in preparing Ti^{3+} self-doped TiO_2 materials with visible activity. This finding illustrated the visible absorption induced by e-polarons. Different from this polaronic resonant excitation at the same localization center, a recent study showed that an intra-polaron excitation cannot account for the experimental absorption

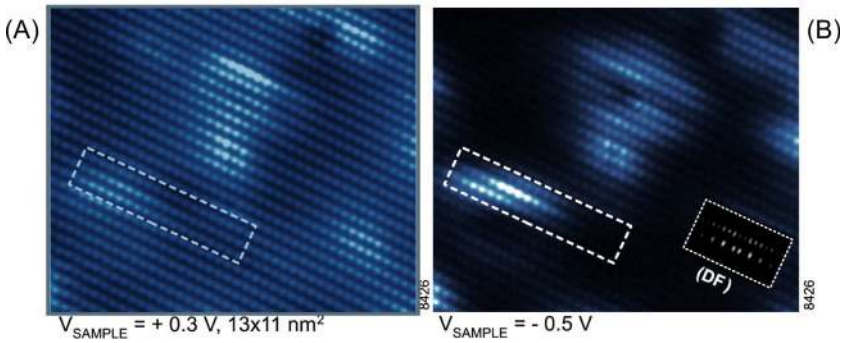

Fig. 24. Shallow donor state at Nb-doped a-(101) surface. (A) Empty and (B) filled states STM images taken at temperature of 6 K (constant height). The bright areas are in the vicinity to subsurface dopants (Nb). The inset "DF" in (B) shows a calculated STM image of the shallow donor state.
Reproduced with permission from Ref. [237]. Copyright 2014 American Physical Society.

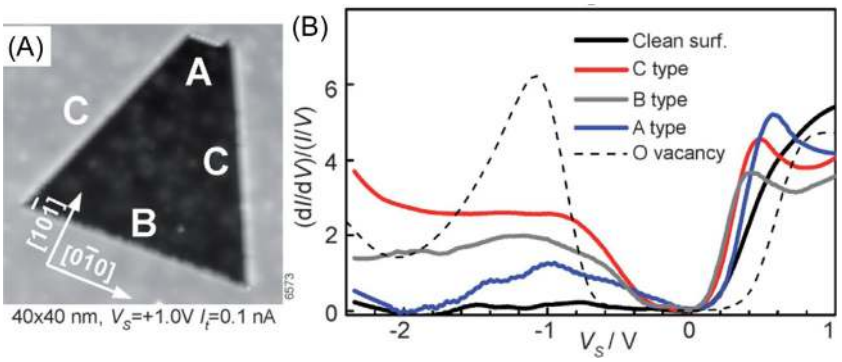

Fig. 25. (A) empty state STM image of a-(101) surface with a typical step edge configuration labeled A–C according to Ref. [241]; (B) STS spectra measured at the steps and at the flat surface of a-(101).
Reproduced with permission from Ref. [240]. Copyright 2014 Wiley-Blackwell.

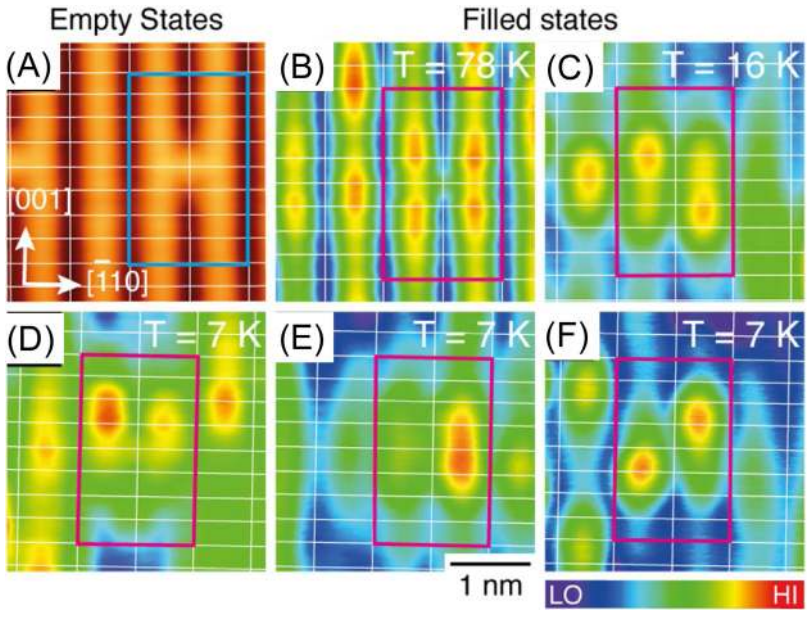

Fig. 26. 3.2 × 3.2 nm² representative STM images of isolated $V_{O,Br}$ on r-(110) recorded using (A) positive (empty states) and (B)–(F) negative (filled states) sample bias at different temperatures: (A), (B) 78 K, (C) 16 K, and (D)–(F) 7 K. Filled-state images in (B)–(F) were recorded in the vicinity of different isolated $V_{O,Br}$. Intersections of the white grids mark the positions of the O_b^{2-}. Rectangles are drawn around the $V_{O,Br}$ and mark the same areas between the empty- and filled-state images in (A), (B).
Reproduced with permission from Ref. [242]. Copyright 2016 American Physical Society.

of trapped holes [248]. Alternatively, the optical transition of h-polarons localized at O2p orbitals was calculated according to an inter-polaronic transition; this corresponds to an optical charge carrier transition from a small h-polaron state localized on one site to another state localized on a neighboring site. This theoretical calculation explained the observations in many transient absorp-

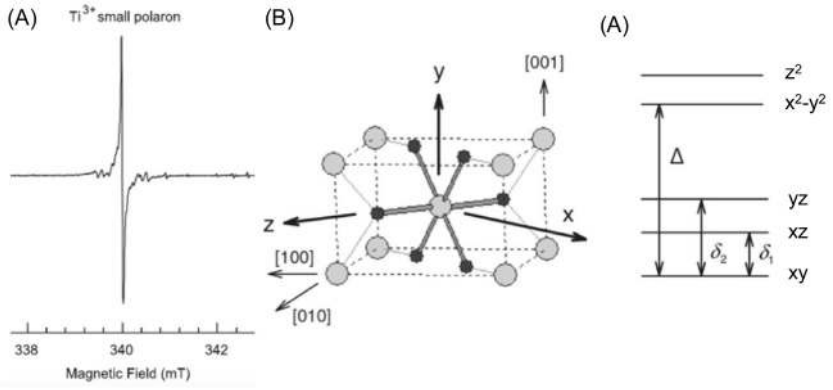

Fig. 27. Photoinduced EPR spectrum from a rutile crystal. These data were taken at 15 K during exposure to 442 nm laser light. (A) a distorted TiO_2 octahedron with the Ti^{3+} ion representing the self-trapped electron at the center. The labeled *x*, *y*, *z* coordinate system is used to describe the d orbitals. (B) Relative ordering in energy of the d orbitals on the Ti^{3+} ion.

tions arising from the holes trapped at regular O sites (h-polarons) [101]. It was shown that the inter-polaronic optical transitions of h-polarons in bulk, at a sub-surface, and on a surface absorb the photons at 550–880 nm, 430–550 nm, and below 450 nm, respectively.

3.2.3. Exciton states

In oxide semiconductors used for photocatalytic or photoelectrochemical applications, optical excitation generates the CB electrons and the VB holes. The above summaries show that the self-localization of photoinduced electrons and holes at normal lattice Ti and O sites leads to e-polarons and h-polarons, respectively. If an e-polaron and a h-polaron locate within the Coulomb interaction distance in space, the electrostatic attraction between them can result in a bound electron-hole pair state called exciton. The formation of excitons in a TiO_2 lattice has been theoretically predicted [197]. Accordingly, because the internal energy of excitons is lower than their counterparts, excitons can also lead to gap states within the TiO_2 forbidden band. The energy depth of an exciton in TiO_2 gap is determined by its binding energy and can be estimated from the hydrogen-like model.

$$E_b = \frac{m_{eh}}{s^2} Ry \tag{2}$$

where m_{eh} is the relative reduced pair effective mass, ε the dielectric constant, and 1 Ry is about 13.6 eV the hydrogen atom Rhdberg energy. m_{eh} relates to relative effective masses of the CB electron and the VB hole according to Eq. (3).

$$m_{eh}^{-1} = m_c^{-1} + m_v^{-1} \tag{3}$$

The presence of excitons in TiO_2 has been previously suggested [249]. An exciton can principally exist in free state and self-trapped state form in TiO_2 materials; these can be observed by photoluminescence measurements. The free excitons cannot be observed by a luminescence method. Under intra-band excitation, the typical low-temperature luminescence spectra of a single crystal anatase TiO_2 featured the luminescence peaked around 2.3 eV; this is attributed to exciton recombination. The 1.1 eV large difference from the 3.2 eV band gap of TiO_2 is ascribed to the stoke-shift. It was seen that the luminescence stimulated by a super-band excitation is independent of excitation energy, so this arises from the radiative recombination of self-trapped excitons in nature. The self-trapped exciton locates in one TiO_6 octahedral in space configuration. In addition to the direct formation of self-trapped excitons, the indirect formation caused by the interaction between electrons (or e-polarons) and holes trapped near crystal defects or impurities was also proposed. A transient luminescence study showed that the luminescence intensity undergoes an exponential decay with a time constant of about 2 μs within the 10 μs measurement timescale. For decay times longer than 10 μs, the luminescence intensity approaches a power law, $1/t^m$, where the value of *m* is nearly equal to 1. The exponential and the power-law decay components, observed by Watanabe et al., are ascribed to the direct and indirect self-trapped exciton recombination, respectively [249,250]. In addition to low temperature PL spectra, polarized absorption spectra can also be used to identify the self-trapped exciton in TiO_2 materials. On the single crystals synthesized from a chemical vapor transport reaction, based on the temperature of polarized absorption spectra near the band edge were well expressed by the Urbach rule; the exciton-photon coupling constant *g*, where $g = S/\sigma_0$ is calculated from a steepness index *S* and a coefficient of steepness parameter σ_0, is obtained to be 2.42 at $E \perp c$ configuration and 2.73 at $E \| c$ configuration. Both the g values are larger than the critical value of 0.937, so it was concluded that the exciton is relaxed to a self-trapped state [251,252].

4. General energy distribution and thermodynamic population of gap states

4.1. Continuous and mono-energetic gap states

In principle, gap states can locate at any energy position within the forbidden band of TiO_2 materials; this is mainly determined by the chemical entities and the charge self-localization illustrated in Sections 2 and 3. The theoretical calculations show that the gap states are in monoenergetic form in single-crystalline TiO_2 materials. In the case of nanostructured TiO_2 materials, gap states can also extend from the band edge into the gap in a continuous way in addition to monoenergetic ones. The monoenergetic gap states do not extend in a continuous way, but distribute in a range of several tens to one hundred meV and feature the most probable energy level. A phenomenological model predicated that the energy width of statistically-distributed monoenergetic gap states is around $2k_BT$, where k_B is the Boltzmann constant. Both the continuous and the monoenergetic states can play an important role in the physiochemical behaviors of charge carriers in TiO_2 materials.

UV–vis spectroscopic studies and electrochemical cyclic voltammetries show the presence of the continuous gap states in both nanostructured rutile and anatase TiO_2 [253–256]. The contin-

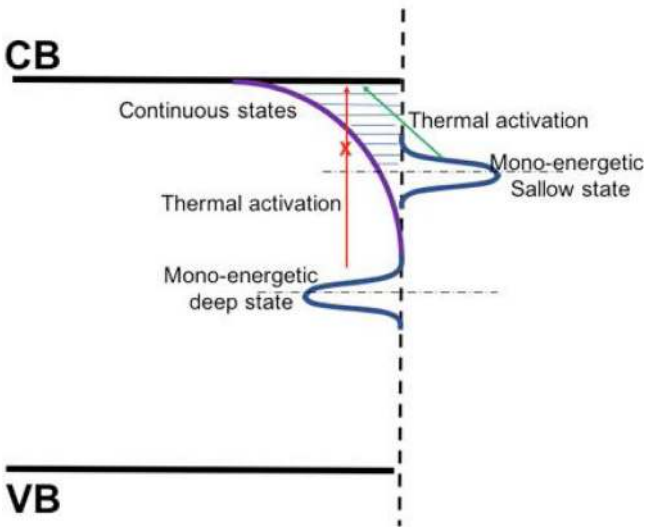

Fig. 28. Diagram of exponential continuous gap states, monoenergetic gap states, deep gap states, and shallow gap states.

uous states can be simply described with a form of an exponential model [257–260].

$$g(E) = \frac{N_L}{k_B T_c} \exp\left[\frac{E - E_c}{k_B T_c}\right] \quad (4)$$

where N_L, E_c, and T_c are the total density of gap states, the energy position of CB edge, and the parameter controlling the depth of a gap state distribution. The monoenergetic gap states in TiO_2 materials were revealed by electrochemical CVs and photoelectron (PE) emissions, which are usually have the form of a Gaussian function with a thermal fluctuation broadening σ [36,37,261,262].

$$g(E) = \frac{1}{\sqrt{2\pi\sigma}} \exp\left(-\frac{(E - E_0)^2}{2\sigma^2}\right) \quad (5)$$

where E_0 is the most probable energy of monoenergetic gap states. The diagram of exponential continuous gap states, monoenergetic gap states, and their relation to shallow gap states and deep gap states are also shown in Fig. 28. Exponentially-distributed gap states and monoenergetic gap states commonly exist in TiO_2 materials.

The physicochemical nature of monoenergetic gap states can be partially attributed to the charge carrier localization at lattice sites or existing defects. However, the physiochemical nature of the exponential continuous gap states is still unclear, and is usually assigned to structure disorder and uc-Ti atoms at the surfaces. The chemical entities that induce the exponential continuous gap states are also different from the V_O and Ti(i) species summarized in Section 3, because they mainly result in singe-level monoenergetic states with Ti3d features occupied by electrons. The exponentially-distributed band-tailed gap states are partially empty under the condition of thermodynamic equilibrium. A recent DFT and DFTB (DFT tight-binding) calculation [263] shows that the 4-f Ti atoms lie at the (100) edges found at the intersection between the (101) cleavage planes and contribute to the exponential band-tail of the continuous empty states. Fig. 29(A) shows that the calculated DOS (density of states) can fit well with Eq. (4). The gap state distribution factor α (T/T_c) was determined to be 0.13; this value is at the lower edge of measured data (0.2–0.5) [60]. Fig. 29(B) shows that the lowest unoccupied states, i.e., the empty states, is present with t_{2g} character located within the entral part of the nanocrystal. The same conclusion for the gap state distribution is also drawn for other nanocrystal boundaries of a-(101)/a-(101), a-(101)/a-(001), a-(001)/a-(001)) and a-(100)/a-(001).

In addition to the above 4-f Ti sites, another possibility is also proposed. The presence of isolated Ti^{3+} bands raises the Fermi level of electrons, and a sizeable fraction of Ti^{3+} states are thermally ionized at room temperature, and are denoted as Ti^{4+*}; this results in a measurable room-temperature conductivity for a-TiO_2 and a corresponding number of positively charged ionized donor sites [Ti^{4+*}]. Therefore, it is thought that these [Ti^{4+*}] states may contribute to the exponentially-distributed band-tailed states [252]. In addition, the disorder structure can induce free electron localization or back-scattering for nanostructured TiO_2 materials. This can result in an anomalous behavior of the low-frequency conductivity that can be understood in terms of Anderson localization [264]. This localization predicts that a system will exhibit the localization of a one-electron wave function if they are in disorder, so strongly disordered systems feature a continuous distribution of gap states below the CB edge. These gap states are responsible for the thermally hopping charge transport behaviors at low frequencies. The diagram for the exponentially-distributed band-tail states in disordered materials is shown in Fig. 30. For a nanostructured TiO_2 materials with very small particles, atom arrangements on surface regions tend to be more or less disordered; this accordingly results in the band-tail states to be exponentially-distributed in energy. Recently, disorder engineering is proposed to modulate the electronic structure of a TiO_2 material by creating localized band-tail states near both the CB edge and VB edge, and typical applications

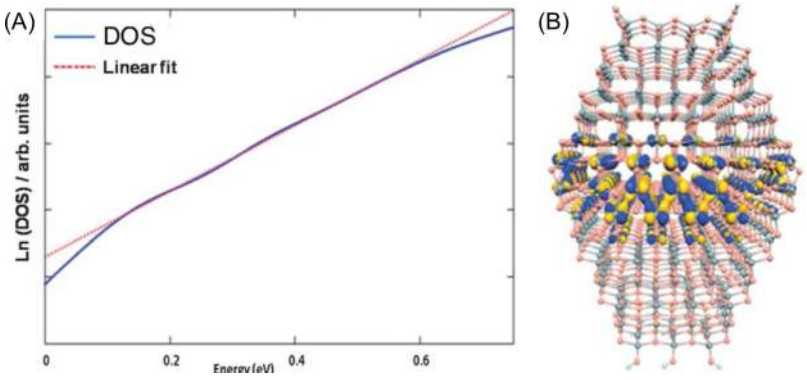

Fig. 29. (A) Linear fit of log data obtained from the DOS of nanocrystals obtained from a PBE/PW calculation. The zero of the energy is set at the LUMO. (B) Representative unoccupied states characterizing the LUMO (left).
Reproduced with permission from Ref. [263]. Copyright 2013 Royal Society of Chemistry.

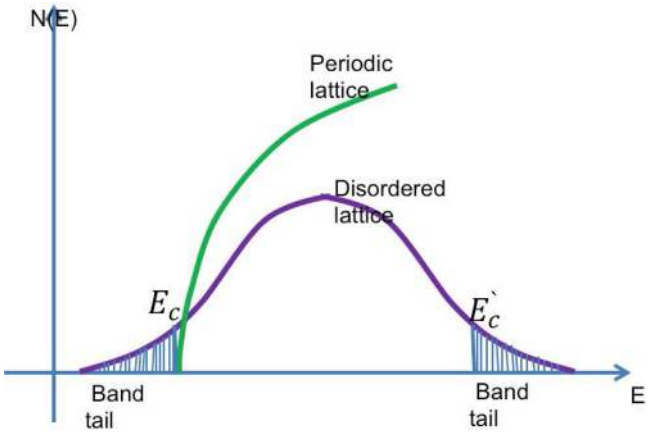

Fig. 30. Diagram of disorder-induced band-tailed continuous states as compared with that induced by a periodic lattice.

include hydroxylated TiO_2 that is highly-attractive in visible light driven photocatalysis [265].

4.2. Shallow vs. deep gap states

The above discussion shows the complicated distribution of TiO_2 intermediate gap states in energy. The gap states locating near the edges of their corresponding extended bands (the CB and the VB) that can interact with the band states under thermal fluctuation and are broadly considered as shallow gap states (SGS). However, the gap states located deep into the forbidden band cannot interact with the band states and are generally considered as deep gap states (DGS). Charge carriers are usually localized at DGS for long period time because of the unavailability of thermal-activation to the CB or the VB states.

As a matter of fact, there is no definite energy level that can be defined to separate the shallow with deep gap states because of the dynamic change of gap sates with experimental conditions, material structures, and observation time (τ_o). Taking a lattice phonon-induced thermal activation into consideration, the electron emission rate from the gap states to the CB states of TiO_2 materials can be described as follows [266–268].

$$\tau_r = (k_B T N(E_c) \upsilon_c \sigma_c)^{-1} e^{(E_T - E_c)/k_B T} = \upsilon_{th}^{-1} e^{(E_T - E_c)/k_B T} \quad (6)$$

where $N(E_c)$ is the density of states at the CB edge, υ_c is the free-carrier vibration velocity of electrons, σ_c is the capture cross-section of the trap, and E_T is the energy of the gap states. The detail balance principle requires that the $k_B T N(E_c) \upsilon_c \sigma_c$ must equal to the attempted-escape frequency (υ_{th}, 10^{12} to 10^{13} s^{-1}). In a given observation time (τ_o), the electrons can be under a distribution of thermal equilibrium among the gap states and the CB states if the emission time τ_r is less than the τ_o. The gap states can then be regarded as shallow gap states in this case. On the contrary, the gap states must be considered as deep gap states if theτ_r is longer than the τ_o. For example, in the study of an electrochemical filling/emptying of exponentially-distributed gap states, a demarcation energy level (E_d) is defined to separate the shallow and deep gap states [269]. The E_d is not pinned at a given energy level, but varies with the experimental conditions, such as the electrochemical potential scanning speed and temperature.

4.3. Statistical population of charge carriers at gap states and quasi-Fermi level

Under thermodynamic quasi-steady state, population of gap states of TiO_2 materials with electrons is determined by a quasi-Fermi level (quasi-E_F) that relates with the Fermi-Dirac statistical distribution of electrons at the gap states [270–272].

$$f(E_T) = \frac{1}{1 + e^{(E_T - E_F)/k_B T}} \quad (7)$$

where E_F denotes the quasi-Fermi level. In a general case, the gap states with an E_T energy lower than the Fermi level of several $k_B T$ are almost completely-filled with electrons. In contrast, the gap states with an energy higher than the Fermi level of several $k_B T$ are almost empty. For the gap states with energy of E_T and DOS of N_T, the densities of occupied gap states and empty gap states are $N_T f(E_T)$ and $N_T(1 - f(E_T))$, respectively. The empty and occupied gap states can play a role in trapping electrons and holes in photocatalytic process. In addition to the intrinsic defects (V_Os and Ti(i)s), the electrons can also be introduced to TiO_2 materials by an electrochemical reduction and light excitation. If the injected excess electrons by these methods cannot not relax to a thermodynamic steady-state condition within an observation time, the electron distribution at gap states cannot be described by a statistical Fermi-Dirac function [270]. For example, our recent Monte-Carlo study indicated that the extrinsically-injected electrons may not reach a thermodynamic equilibrium distribution in the exponential continuous gap states before they transfer to O_2 [36]. The simulation of transient photocurrents with a random-walk model also showed the presence of non-thermalized electrons that contribute to photocurrents in a dye-sensitized nc-TiO_2 film [270].

The Fermi-Dirac population of gap states with electrons can be switched by the non-equilibrium electron filling/emptying (electrochemical reduction and photon excitation) that would lead to material polarization [271–273]; this was shown to be important in charge carrier kinetics of TiO_2 materials and related to photocatalytic or photoelectrochemical properties. In an electrochemical system, the thermodynamic of electrons in TiO_2 can be changed by applying a bias potential between the reference electrode and the TiO_2 electrode. In principle, the applied potential will drop onto the TiO_2/electrolyte interface that includes a diffusion layer in the electrolyte, a compact Helmholtz layer, and spatial charge layer in TiO_2. In the general case of a depletion layer formed in TiO_2, the bias potential mainly drops on the TiO_2 material, which leads to the change of thermodynamic of electrons in a TiO_2 electrode. For a nc-TiO_2 material surrounded by a highly-concentrated electrolyte, the applied bias potential leads to a corresponding change of electron Fermi level, as shown in Fig. 31(A). The shift of Fermi level destroys the thermodynamic equilibrium on TiO_2/electrolyte and results in Faradic reactions. In the presence of gap states, the Fermi level shift can change the electron population in them, and eventually influence the charge carrier kinetics mediated by gap states. Fig. 31(A) shows that a thermodynamically empty gap state is populated by electrons under Fermi level up-shift due to negative bias potential, which can allow electron transfer from gap states to oxidation species in electrolytes. Differently from the bias potential polarization, as shown in Fig. 31(B), the light illumination simultaneously creates the CB electrons and the VB holes, which leads to a quasi-Fermi level ($E_{F,n}$) for electrons and a quasi-Fermi level ($E_{F,p}$) for holes. The shift of these Fermi levels changes the corresponding populations of electrons and holes at gap states, which allows for further interfacial transfer of electrons and holes to oxidation and reduction species in electrolytes. Therefore, the quasi-Fermi level is an important parameter that determines the chemical potential of electrons and holes populating at gap states to participate in photocatalytic reactions.

The energy distribution and thermodynamic occupation of gap states can be determined by many experimental techniques: including the electrochemical cyclic voltammetry; electrochemical spectroscopy; photoelectron emission spectroscopy; optical spec-

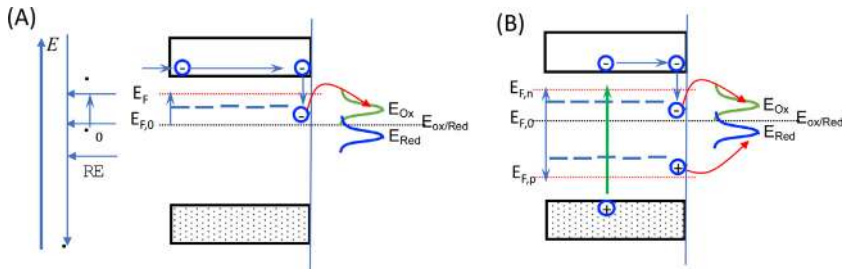

Fig. 31. (A) Diagram for changing the population of electrons at gap states induced by a bias potential; (B) diagram of changing the population of electrons and holes at gap states induced by a super bandgap light illumination.

troscopy; and others, because of the effects of gap states on the physiochemical behaviors relating to these techniques.

5. Experimental studies of the gap states and the association with chemical entities and charge carrier localization

5.1. Photoelectron energy spectroscopy (PES)

The energy distribution and the density of occupied gap states locating at surfaces or sub-surfaces can be detected by PES measurements, because the gap state induced photoelectron (PE) peaks are frequently present on the PES valence spectra of TiO_2 below the Fermi level. In Section 2, the defect chemical entities inducing the PES peak were partially summarized in order to elaborate the chemical entity roles in forming gap states. In this sub-section, we mainly illustrate the energy distribution and the density of gap states as indicated by the PES results. Generally, the V_o-induced gap states detected by the PES were determined to contain a Ti3d feature. For clearly probing the Ti3d states by using PES, TiO_2 surfaces must be pre-treated to create Ti3d states by high energy particle bombardment and UHV annealing, because normal TiO_2 surfaces cannot generate strong PE signals due to the low density of gap states.

The Ti3d-featured gap states on r-(110) surfaces were extensively studied by using PES. The Ar^+ bombardment of a r-(110) surface can create clear Ti3d gap states by removing bridging O atoms, appearing as a PE peak located ~0.7 eV below the Fermi level (near the CB edge) and having a monoenergetic distribution, with an energy width of ~0.1 eV [138]. Further exposure of the above reduced TiO_2 to an O_2 atmosphere results in a quenching of the Ti3d-featured peak due to oxygen residing or dissociating at V_o sites. Similar results were also observed by other authors [274]. In other research [90], the r-(110) surface were reduced by electron bombardment. The UPS spectra measured across gap state regions show that the Ti3d derived gap states locate ~0.9 eV below the Fermi level. It was shown that the density of the Ti3d gap states increases with the increase of V_os by increasing electron bombardment time due to an increase of gap states. In addition to the rutile phase, the a-(101) and a-(001) surfaces after Ar^+ bombardment and UHV annealing were also studied by PES. Clear Ti3d derived monoenergetic gap states appear at 1.1 eV below the Fermi level. The decrease of Ti3d gap state density by O_2 exposure supports that this gap state is ascribed to the V_O species. The positions of PE peaks agree well with the STS studies, which also shows that the gap states are 1.1 eV below the Fermi level.

PES was also used to compare the V_o-induced Ti3d gap states of different TiO_2 materials. This compared the gap states of an in situ cleavage single crystal a-(101), and atomic layer deposited (ALD) amorphous TiO_2 (α-ALD-TiO_2) coating, a screen-coated anatase TiO_2 nano-porous (nc-TiO_2) film, and a calcined ALD TiO_2 (c-ALD-TiO_2) film [275]. The α-ALD-TiO_2 shows a strong PE emission contributed from deep gap states around 1.2 eV below the Fermi level. which can be greatly reduced when subject to further annealing (Fig. 32(A)). Differently, annealing increased the shallow gap states that locates below the Fermi level and extends to ~0.6 eV binding energy (BE). The c-ALD-TiO_2 has the gap states that are similar to the nc-TiO_2 and the cleaved a-(101). Synchrotron radiation increases the density of deep gap states in the α-ALD-TiO_2 films (Fig. 32(B)) and the cleaved a-(101) surface (Fig. 32(C)), whereas shallow gap states in them are less affected. The deep gap states are assigned to the 0-dimensional point defects mostly presenting in and near a-(101) surfaces. The shallow gap states are attributed to the excess electrons present at Ti_{4c} atoms (1-dimensional line defects) that are either step edges or imperfections of a cleavage plane, but are also inherent to the 3-dimensional crystallites. The gap states induced by Ti_{4c} atoms extends below the CB edge into the deep energy gap. Because they are below the Fermi level, these gap states are occupied under thermodynamic equilibrium. The fitting of shallow gap states with the combined Gaussian function and Fermi-Dirac statistics further shows that the thermal broadening of this energy distribution and their occupation relies on the Fermi level.

5.2. Electrochemical techniques

In electrochemical techniques, the energy distribution and the density of gap states are obtained by measuring the gap state relating the chemical capacitance (C_{ch}) by removing the Faradaic effect. The contribution of gap states to the C_{ch} is described as [276,277]

$$C_{gs} = e^2 \frac{dN_L}{dE} \tag{8}$$

where e is the elementary charge and N_L is the density of gap states at energy E. It was observed that the gap states contribute to the typical capacitive responses of nc-TiO_2 electrodes in an aqueous electrolyte [278]. Fig. 33(A) and (B) shows a typical CV curve of a nc-TiO_2 film electrode and the corresponding chemical capacitance. It can be seen that the main component arises from a CV feature that increases exponentially from the accumulation onset toward more negative potentials [279,280]; this feature is associated with a charge accumulation/extraction for short resistance time of the exponential continuous gap states (Eq. (4)). The exponential distribution of DOS with respect to energy ($N(E)$) can be obtained by fitting this accumulated CV feature with Eq. (1). The fitted parameter α_c (T/T_c) that determines the distribution depth of gap states usually values between 0.2 and 0.7. Near the onset of this reversible capacitive region, an additional capacitive cathodic peak was often present due to the charge filling/emptying of the monoenergetic gap states. This feature is a characteristic of nc-TiO_2 film electrodes because it is absent on the CVs of structurally well-defined single-crystal electrodes. Therefore, it is assigned to the gap states on the boundary interface. Similarly, the Gaussian-distribution of DOS ($N(E)$) can be partially obtained by fitting this peak with Eq. (5). It is worth saying that the absolute energy position of gap states relative

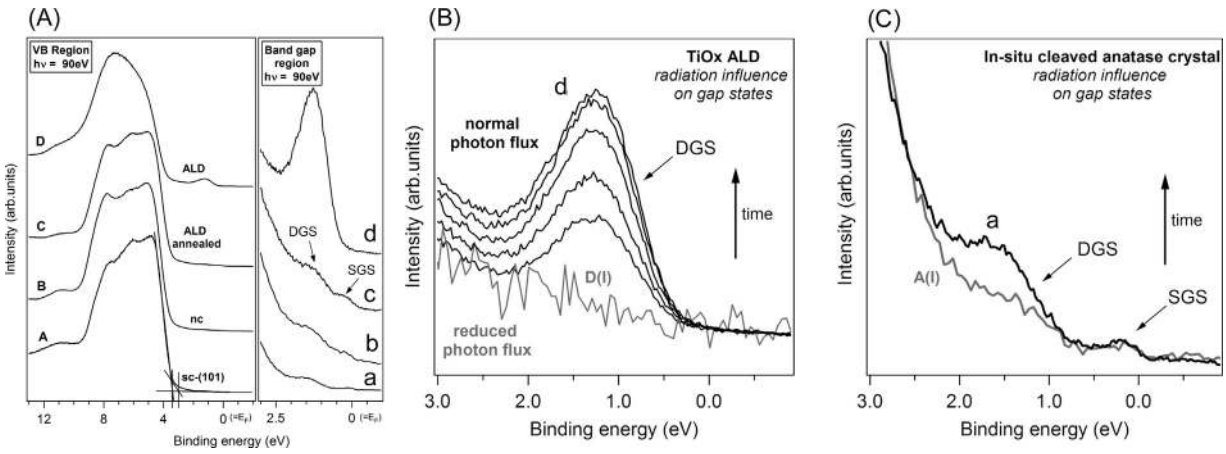

Fig. 32. (A) Valence band spectra (left) and enlarged band gap regions (right) of (a) in situ cleaved single crystal a-(101) surface, (b) sintered mesoscopic anatase film, (c) annealed ALD titania film, and (d) the ALD titania film prior to annealing. Development of gap state emission with increasing exposure time to 90 eV synchrotron radiation for ALD titania (B) and the single crystal TiO_2 (101) cleavage plane (C).

Reproduced with permission from Ref. [275]. Copyright 2015 American Chemical Society.

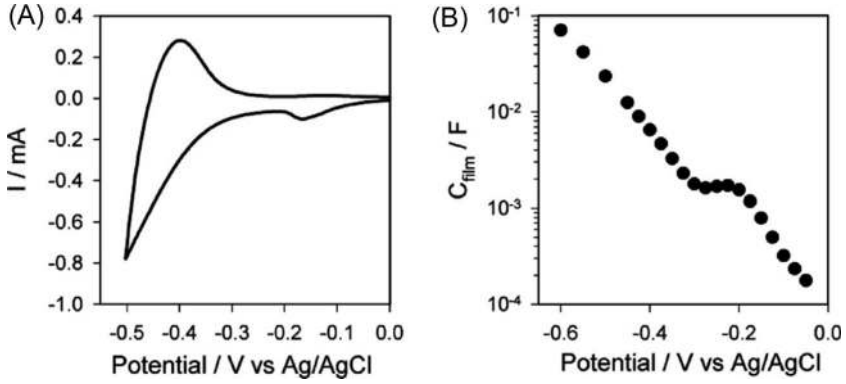

Fig. 33. (A) CV of TiO_2 film in aqueous solution at pH 2 presenting a surface state peak (B) capacitance of the same sample. The exponential growth of the capacitance is modified by the presence of the surface state.

Reproduced with permission from Ref. [278]. Copyright 2008 Elsevier.

to the band edge cannot be directly determined from the peak position because of the sensitivity of CVs to experimental conditions, such as the scanning speed, pH value, and electrode pre-treatments, and needs a further assistance, for example from Mott–Schottky curves.

The CV studies revealed the dependence of energy position of TiO_2 gap states on crystalline phases. Fig. 34(A) shows the CVs of anatase and rutile nanowires [279]. A linear fitting was performed to $\ln(C) - E$ for the rutile nanowires according to Eq. (4). The slope corresponding the α_c was determined to be near 1, showing that the exponential feature in CVs originates from the electron accumulation/extraction of the CB states. However, for the anatase nanowires, the $\ln(C)$ vs E plots do not show a slope close to that contributed by the CB states, giving an α_c value of ~0.27, in good agreement with another study [281]. This result shows the presence of an exponential continuous surface gap states distributed below the CB edge in anatase nanowires. For rutile nanowires, the pair of capacitive peaks are separated from the accumulation region, whereas that of anatase nanowires are located at the onset of the accumulation region. The energy width of these capacitive peaks in basic conditions for the rutile and anatase nanowires are about 64 and 54 mV, suggesting their correspondence to monoenergetic gap states. The gap states of anatase and rutile nanowires is sketched in Fig. 34(B). In summary, the CV studies show that the presence of monoenergetic gap states for anatase and rutile was at different potentials together with an exponential surface state distribution just below the CB for anatase.

The analysis of CV responses also revealed a strong dependence of gap-state density on morphological structures of the films. In a research conducted by Berger et al. [282], three different films of oriented rutile nanowires, random rutile nanoparticles, and r-(110) single crystals were investigated with CVs, as shown in Fig. 35. They observed that monoenergetic capacitive features form with an energy width of 50 and 100 meV on the CVs of nanoparticle and nanowire films. A significant difference between them consists in the density of gap states, as tracked by the pair of capacitive peaks. The density of gap states in the nanoparticle TiO_2 film (per cm^2 of projected area) is almost 15 times higher that of the nanowire film. The pair of capacitive peaks contributed by gap states is absent in a well-defined r-(110) single crystal. The energy distribution of gap states in an anatase nanotube arrays was also studied by CVs, which gave results similar to anatase NWs [283]. The combination of impendence spectroscopy and CVs also revealed the existence of exponential band tailed states in a-TiO_2 nanotubes with high density [284]. The higher density of deep trap stated in the TiO_2 nanotube arrays can allow the trapping of up to 5×10^4 electrons in a single nanotube at negative bias [285]. A recent study revealed that the deposition of Pt nanoparticles on TiO_2 nanotube arrays prepared from anodization can have a great effect on the exponentially-distributed continuous gap states and the monoenergetic gap states [286] because their density can be tuned by the

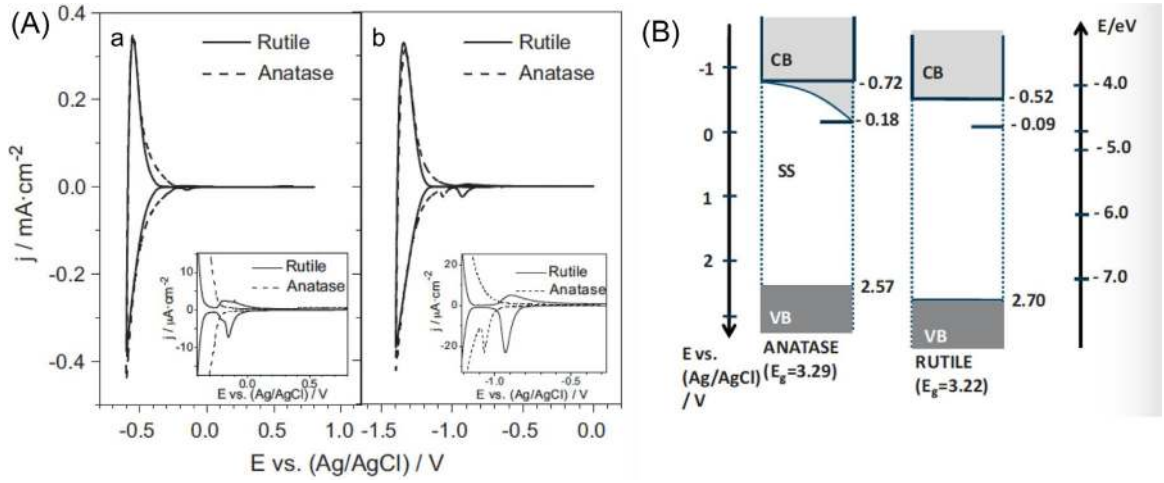

Fig. 34. CVs for a-TiO_2 and r-TiO_2 nanowire electrodes in the dark. Working solution: N_2-purged 0.1 M $HClO_4$ (A), and 0.1 M NaOH (B) (scan rate: 20 mV s^{-1}). Inset: detail of the peaks associated to grain boundaries. (C) Schematic illustration of the electronic band structure for a-TiO_2 and r-TiO_2 NW thin films.
Reproduced with permission from Ref. [279]. Copyright 2012 Elsevier.

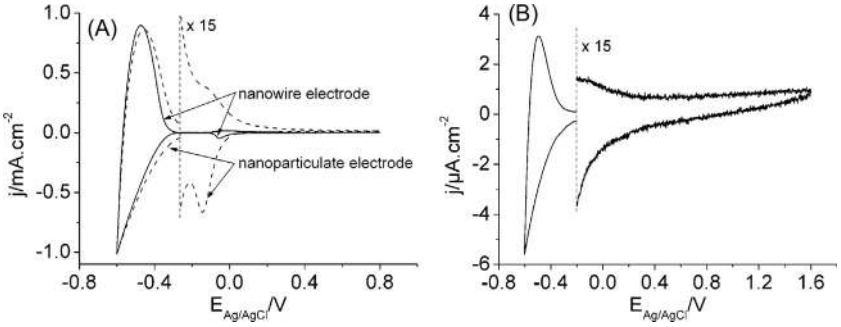

Fig. 35. (A) CVs for a nanowire electrode (solid line) and a nanoparticulate electrode (dashed line). (B) r-(110) single-crystal electrode; electrolyte: 0.1 M $HClO_4$; scan rate: 20 mV s^{-1}.
Reproduced with permission from Ref. [282]. Copyright 2007 American Chemical Society.

amount of Pt nanoparticles. Under the dark and illumination conditions, it was shown that the density of sallow traps (N_L) can be increased by tens to several thousand times. When many Pt nanoparticles were deposited, the density of deep monoenergetic gap states (N_t) is reduced by several times. In a recent study, we also revealed by using electrochemical CVs that thermal-deposited Au nanoparticles created more additional monoenergetic gap states associated with V_o species around the Au/TiO_2 perimeter region on TiO_2 nanorod surfaces [287], which was also supported by conductivity, spectroscopy, and Mott–Schottky measurements [288–290].

In addition to CVs, the chronoamperometry was also developed to study the energy distribution and the density of gap states of TiO_2 materials [291]. The cathodic charges accumulated at different potentials were obtained by integrating the current–time curves in this method. Assuming that the accumulated charge, Q, by trap-filling reflects the density of gap states that play a role of electron traps, they can be described by the following equation.

$$Q = q\int_{E_F^0}^{E_F} N_{Trap}(E)\mathrm{d}E \tag{9}$$

where $N_{trap}(E)$ is the gap state density as a function of energy, E_{Fo} denotes the dark Fermi level at the initial potential U_{Fo} well below the gap states investigated, E_F is the Fermi level at the present potential U, and q is elementary charge. Since $E_F - E_{Fo} = -q(U - U_{Fo})$, the density of gap states can be expressed by

$$N_{trap}(U) = -\frac{1}{q}\frac{dQ}{dU} \tag{10}$$

Eq. (10) shows that the density of gap states is proportional to dQ/dU, which provides a direct measure of the trap distribution.

By using this technique, the dependence of gap state density of nc-TiO_2 films on pH values was studied [291]. Fig. 36 shows the Q accumulated at different potentials as derived by integrating the current-time curves in solutions at pH 13 (A) and 4.7 (B). The derivative of Q vs the U (insert) shows the monoenergetic feature of gap states. In the case of pH = 13, most traps located at potentials more positive than −0.9 V, and the total trap density is 5×10^{13} cm^{-2}. For a pH of 4.7, the saturation of accumulated Q at potentials was more negative of −0.3 V and indicates that most traps locate at potentials more positive than −0.3 V. The gap states distribute mainly from −0.3 V to −0.4 V, and the total density of traps was estimated to 4×10^{11} cm^{-2}. This result is line with that obtained from intensity-modulated photo-voltages [292], photocurrent spectroscopies [293], and electrochemical spectroscopy [294]. The dependence of gap state density and distribution on the pH values was also studied by linear voltammetries (*LV*s) by relating the cathodic peak with the $N_{trap}(U)$ according to following equation.

$$N_{Trap}(U) = \frac{1}{q}\frac{j}{v} \tag{11}$$

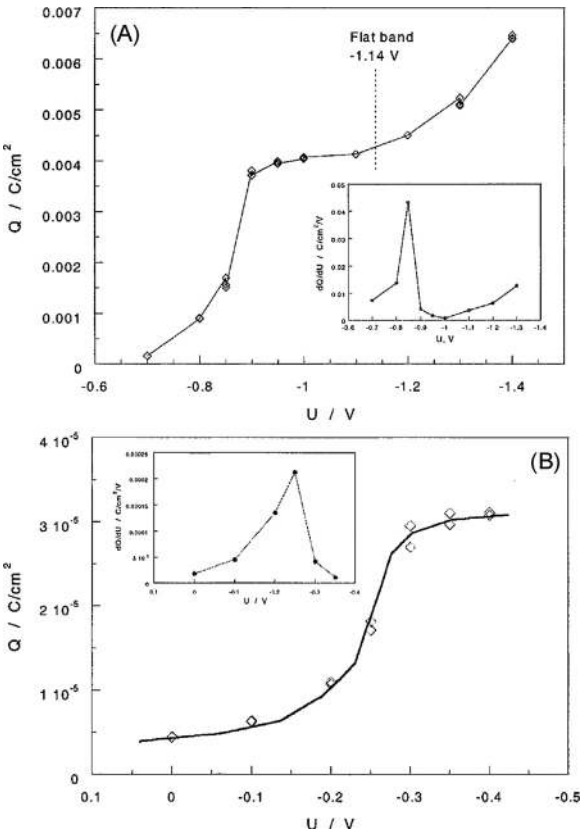

Fig. 36. (A) Cathodic charges accumulated at different potentials as derived by integrating the current-time curves in 0.1 N NaOH solution. The insert shows charge distribution against potential. The electrolyte was purged with nitrogen gas and heavily stirred. (B) integrating the current–time curves in the solution at pH 4.7. The electrolyte was purged with N_2 and heavily stirred. The insert shows dQ/dU distribution against potential.

Reproduced with permission from Ref. [291]. Copyright 2001 American Chemical Society.

where j is the current density, $\nu(dU/dt)$ is the scanning rate. The LVs of nc-TiO_2 film electrodes in cases of different pH values shows the pH-dependence of $N_{trap}(U)$ in a form of $Q \approx 3.0 \times 10^{-6} e^{0.53pH}$ [C cm^{-2}]. The pH dependence of the distribution and density of gap states in nc-TiO_2 films shows the location of gap state on surfaces that are accessible to protons.

Bertoluzzi et al. [295] pointed out that the apparent chemical capacitance associated with the exponential continuous deep gap states may also reach a peak when charging the material and remains zero when subsequently discharging. In the dynamic region, deep traps, unlike the shallow exponential-type traps, exclusively depend on the trapping rate and are therefore in dependence on the energy level of the localized states. Therefore, the monoenergetic capacitive peak in the CVs may contain two contributions from the deep exponential continuous gap states and the real deep monoenergetic gap states.

A theoretical model was proposed to separate the density of these deep localized states by using the voltammetric measurements. For the scanning speed of $\nu(dV/dt)$, the E_d level that separates the deep gap states with the shallow ones is defined in a CV measurement according to

$$E_d = k_B T \ln\left(\frac{\nu}{\nu_0}\right) + E_{F0} \tag{12}$$

with $\nu_0 = k_B T/(q\tau_0)$. τ_0 is defined as the average trapping lifetime of free electrons under the condition of thermal equilibrium according to

$$\tau_0 = \left(\beta_n N_{CB} \exp\frac{(E_{F0} - E_C)}{k_B T}\right) \tag{13}$$

where β_n is a time constant per unit volume for capturing electrons, usually given in terms of the thermal velocity of electrons (ν_{th}) and the capture cross section (σ_{nc}) in a form of $\beta_n = \nu_{th}\sigma_{nc}$ [56]. The peak position of capacitive current induced by the exponentially-distributed deep gap states varies with the scanning speed according to

$$e - \frac{qV_{peak}}{k_B T} = \frac{\nu}{\nu_0} \tag{14}$$

Therefore, the total chemical capacitance for both the deep gap states of the exponential DOS and the monoenergetic level (N_t traps per unit volume) can be recovered by assuming that E_d (E_v (the potential position of the VB)

$$C_{deep}^{peak} = \frac{1}{e}\frac{q^2 L}{k_B T}\left[N_{L0}\left(\frac{\nu}{\nu_0}\right)^{\alpha} + N_t\right] \tag{15}$$

where $\alpha = T/T_0$, $N_{L0} = N_L \exp\alpha(E_{F0} - E_c)/k_B T$, and $e = \exp 1$. The first term on the right side of the equation is from the deep exponential gap states that increases with scan rate and the second term is from the monoenergetic level of states that is independent of scan rate. For the sub-μm particles on a FTO substrate (Fig. 37(A)), the chemical capacitance associated to the deep gap states were measured by CVs (Fig. 37(B)). It was seen that the peak position and the intensity increase with scan rate, which fit well with Eqs. (14) and (15), as shown in Fig. 37(C) and (D). The density of exponential continuous gap states (N_L) and the density of monoenergetic levels are 8×10^{18} cm^{-3} and 2×10^{16} cm^{-3}, respectively. The N_t is much smaller than the N_L, so this research drew a conclusion that the electrons are mainly trapped in the exponential deep gap states, rather than the monoenergetic ones. Using the small perturbation technique, an impendence spectrum can be directly used to determine the chemical capacitance induced by monoenergetic gap states. This shows that the nc-TiO_2 electrodes present much higher density of monoenergetic gap states than that of a micro-crystalline TiO_2 electrode.

The above research took the band edge pining at surface as granted. However, it is also shown that this assumption is sometimes untrue for more negative applied potentials because of the unneglected potential drop in the Helmholtz layer, which can result in the Fermi-level pinning case [296,297]. The shift of band edge in the course of CV scan leads to a different estimation of gap state distributions and spatial location. Mandal et al. restudied these problems by including the case of band edge unpinning [298]. Eq. (4) describes the exponential distribution of continuous gap states assumed in the case of band edge pinning. The parameter $\Delta E_{CB}/q$, i.e. the potential drop across the Helmholtz layer, needs to be included in the equation for the band unpinning, so Eq. (4) is re-written as

$$g(E) = \frac{N_L}{kT_C}\exp\frac{(E_F - E_{CB} - \Delta E_{CB})}{kT_c} \tag{16}$$

to describe the effective density of gap states as a function of applied potentials. The ΔE_{CB} was determined from the blue-shift of band gap absorption induced by the electron filling at the CB states. The band edge corresponding a no shift is estimated from a linear extrapolation of the apparent band gap shift with applied potentials. Based on Eqs. (4) and (16), the difference between the cases of band pinning and band unpinning can be compared. It is shown that the case of band edge pinning predicts the main location of gap states at surface for a nc-TiO_2 electrode. For the unpinning case, the

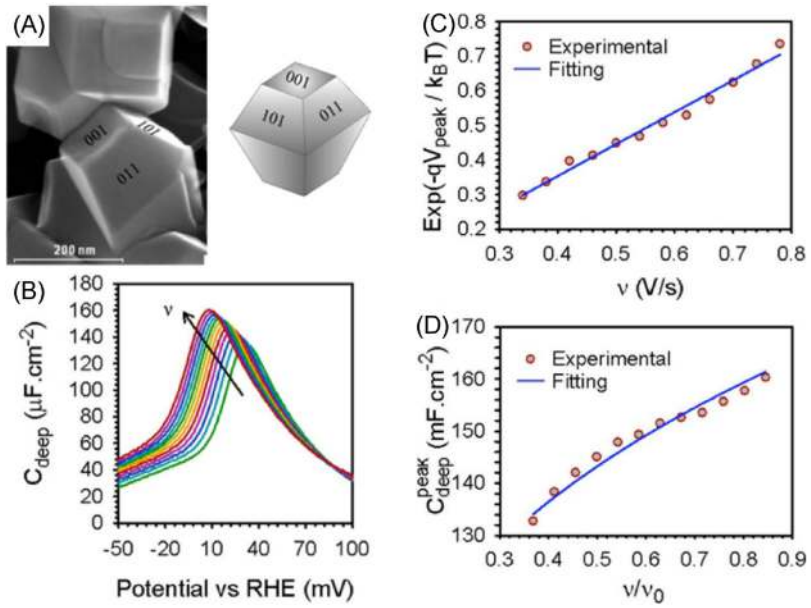

Fig. 37. (A) HR-SEM top-view image of a low surface area sub-μm a-TiO_2 electrode. (B) Evolution of the deep gap trap chemical capacitance with varying scan rate for the TiO_2 sub-μm particle; (C) Boltzmann type exponential factor calculated at the voltage of the deep trap capacitance peak versus scan rate; (D) deep trap capacitance peak versus normalized scan rate/the dots indicate the experimental data, while the blue solid lines correspond to the fitting.
Reproduced with permission from Ref. [295]. Copyright 2014 American Chemical Society.

density of surface gap states was estimated by using the magnitude of band edge shift related by the following equation.

$$\frac{\Delta E_{CB}}{q} = \frac{qn_s}{C_H} \quad (17)$$

where C_H is capacitive of the Helmholtz layer. The bulk gap state density was obtained by subtracting n_s with the total density of trapped electrons. The densities of bulk traps and surface traps obtained by this method are 1.4×10^{21} cm^{-3} and 2.4×10^{19} cm^{-3}, respectively. Therefore, the band edge unpinning case leads to a conclusion that the gap states mainly locate in bulk, instead of on the surfaces, in contrast to the above band edge pinning case.

To avoid surface contamination from sample preparation in air, Takata et al. took an ultra-high vacuum electrochemistry approach to study gap states of r-(110) [299]. A set of Mott–Schottky plots of this TiO_2(110) surface were obtained for various modulation frequencies before and after UV illumination, as shown in Fig. 38(A). The nonlinear Mott–Schottky plots were observed in an electrode potential range of −0.25 to +0.25 V vs. Ag/AgCl for the as-prepared clean TiO_2(110)-(1×1). This is attributed to deep-surface gap states, whose frequency dependence indicates that the trapping–detrapping process of the deep-surface states seems not to be able to response at frequencies above 1000 Hz. After UV illumination at +0.6 V vs Ag/AgCl for a while, the nonlinear parts in the Mott–Schottky plots completely disappeared due to a photoetching effect, showing almost no frequency dependence as far as measured in the experimental frequency range. The density of these surface gap states was estimated by using the Tomkiewicz model, which show that the gap states locate at around −0.14 V vs. Ag/AgCl and the density before UV light illumination was calculated to be 6.4×10^{14} cm^{-2}, in good accordance with other reports [286] 6×10^{14} cm^{-2} and 9.6×10^{13} cm^{-2}. Because the surface used in electrochemical measurement is prepared under oxidizing conditions and immersed in water solution, the contributions from bridging V_os and hydroxyl groups cannot be important, so they suggested that these surface gap states are highly likely to be induced by Ti(i) atoms in sub-surface regions. The schematic band diagram is plotted as Fig. 3(B) to show the energy distribution of surface band gap states at TiO_2/electrolyte interface.

5.3. Transient optical absorptions

In addition to PE and electrochemical behaviors, population of electrons at gap states can result in optical absorptions. The wavelength range of optical absorptions and their features can to some extent also provide effective information for energy distribution and density of gap states. The trapped electrons and the trapped holes in TiO_2 have the characterized absorptions that are usually called as “finger” absorptions [300]. Such a concept was firstly proposed by Bahemman et al. in their work that studied charge trapping in TiO_2 colloid sols [301]. When a TiO_2 sol merely containing polyvinyl alcohol for hole scavengers was flashed by a laser light, the adsorption with a maxima at 650 nm was present immediately and did not exhibit a decrease in the observation timescale of several ms. Because this transient absorption decays when the O_2 or other electron scavengers are present, it is attributed that the long-lived electrons are probably trapped close to surface defects. The positively-charged TiO_2 colloid sol containing methyl viologen as an electron scavenger shows a broad band with the highest absorption at 475 nm. Depending on the concentration of hydroxyl groups that are consumed in the measurement, this absorption is attributed to excess holes trapped at colloidal particle surfaces. It can be shown from their broad transient absorption that the gap states for trapping electrons and holes may have a wide distribution locating deep within the TiO_2 forbidden band with respect to energy.

Depending on the methods of electron injections, the spectroscopic absorptions include electrospectroscopic absorption and light induced transient absorption. Electrochemically-induced electron population of gap states can cause optical transition from the gap states to the CB states of TiO_2 materials. Under Fermi-level control, it is seen that the electrons accumulated in TiO_2 can result in typical light absorption in energy ranging from the mid-IR to the UV region (0.1–3.3 eV); this allows for the detection of electronic transition in a region between the fundamental absorption

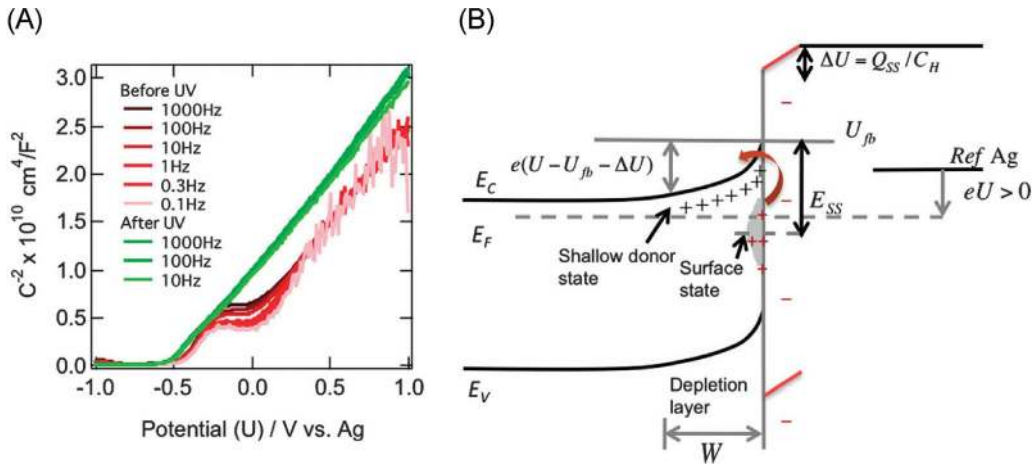

Fig. 38. A set of Mott–Schottky plots of a r-(110) surface were obtained for various modulation frequencies before and after UV illumination, based on the equivalent series RC circuit (A), together with a schematic of the band diagram to illustrate the surface state in the band gap at the TiO_2/electrolyte interface (B).
Reproduced with permission from Ref. [299]. Copyright 2014 Royal Society of Chemistry.

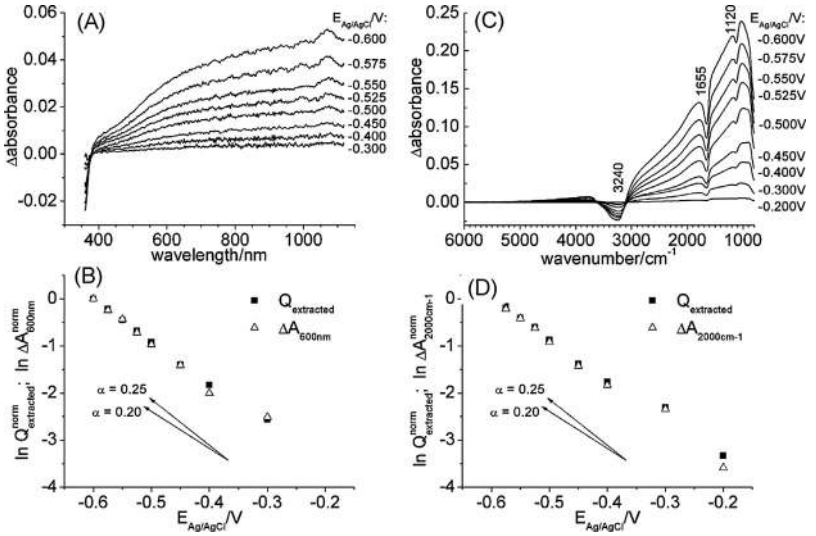

Fig. 39. UV/vis/NIR (A) and middle IR spectra (C) of a-TiO_2 nanocrystal electrodes at different electrode potentials (polarization time: 240 s). The reference spectra were taken at $E_{Ag/AgCl}$ = 0.4 V. (B, D) Semi-logarithmic plot of absorbance and extracted charge vs electrode potential. Arrows indicate the slopes corresponding to different α values (T = 298 K). Electrolyte: N_2-saturated 0.1 M $HClO_4$ aqueous solution; charge extracted upon back polarization from −0.6 to 0.4 V.
Reproduced with permission from Ref. [280]. Copyright 2012 American Chemical Society [280].

threshold and the onset of lattice adsorption. Upon cathodic polarization of the nc-TiO_2 electrode, Fig. 39(A) shows an absorption signal develops in the UV/vis/NIR wavelength that is reversible with respect to an anodic back polarization [280]. The localization of electrochemically injected electrons at regular Ti sites result in Ti^{3+} ions, so this broad absorption has been attributed to the d-d transition of Ti3d-featured gap states [245]. The DFT and the PES studies reveal that the narrow Ti3d gap states locating 0.8–1.2 eV below the CB edge, so it is uncertain if the d-d electronic transition may not cover wide wavelengths. Therefore, thus light absorption relating to gap states is also attributed to the electron transition from Ti^{3+} states to the CB states of TiO_2, as observed in the Ti^{3+} self-doped TiO_2 materials [302–304]. Because the optical absorption range is dependent on both the initial gap states and final wide CB states, the observation of such broad absorption is reasonable.

Broad mid-IR absorptions are also developed upon cathodic polarization (Fig. 39(C)); this shows an increase with an increase of negative potentials and a monotonical increase toward lower wavenumbers. It is suggested that this broad mid-IR absorptions can be ascribed to many reasons that include the excitation of the electrons trapped at shallow gap states to the CB states and the intra-band transition of free electrons associated with photon absorptions. It is thought that the polaron excitation within a 2-dimensional plane may also have a contribution [305,306]. The sharp absorbances cut-off around 1000 cm^{-1} were also partially attributed to the transition associated the electrons trapped at shallow gap states, possibly arising from the combination of electrons and protons, i.e., $(e^-)(H^+)$ pairs [307].

The normalized change of visible absorptions at 600 nm in Fig. 39(A) ($\Delta A600$) and the extracted charge (determined by electrochemical CVs) were plotted in a semi-logarithmic form with respect to the electrochemical potential, as shown in Fig. 39(B). The semi-logarithmic plots of normalized IR absorptions at 2000 cm^{-1} and the extracted charges are shown in Fig. 39(D). Fitting these lines with Eq. (4) results in a $\alpha(T/T_0)$ of 0.23; this indicates that these gap states contribute to UV/vis/NIR and mid-IR absorptions are closely associated with the exponential continuous gap states distributed below the CB. The density of these gap states is indicated by the absorption extinction coefficients and the extracted charge. By assuming spherical particles with a radius of 10 nm, a

particle volume of 0.5, and a coating thickness of 2.3 μm, the number of electrons accumulated in a particle is predicted to be 650 when the electrochemical induced absorption is saturated. Similar results were also obtained by correlating the IR absorptions at 2000 cm^{-1} and the extracted charges.

other research observed different results for the electrochemically induced absorption in a nc-TiO_2 film electrode [308]. Fig. 40(A) shows the potential-dependent absorption spectra at potentials that are more positive than the flat potential V_{fb} (−0.73 V at pH 6.2). It is seen that a weak absorption in the UV–vis region is firstly developed as the electrochemical potentials shift to the CB edge and which becomes the clearest at −0.30 V (bold black line). This absorbance is the strongest at 400 nm and gradually decreases to zero at 600 nm. When the potentials are over −0.40 V, significant changes occur such that the absorption increases throughout the whole visible region, while the absorbance in the UV region is slightly bleached. Fig. 40(B) shows the absorbance change as accumulated charges increase, which show that the absorption at 400 nm is markedly different from that at 700 nm. The initial slope of 400 nm is very high, whereas that of 700 nm is zero. After passing of about 0.4 mC cm^{-2}, the slope at 400 nm decreases, whereas the slope of the 700 nm trace increases. Therefore, it is proposed that the 400 nm adsorption induced by electrochemical doping arises from gap states in TiO_2, while that of 700 nm originates from an intra-band absorption of the CB free electrons. From this viewpoint, the 400 nm absorptions indicate the presence of shallow gap states that are very near to the band edge. It is also estimated that the saturated absorption at 400 nm corresponds to about 12 trapped electrons per particle. Assuming the gap states in bulk will result in an unrealistically density of 10^{19} cm^{-3}. 3×10^{12} cm^{-2} of gap state density was obtained if the gap states locate on surface, also in good accordance with other results [292].

Different from the electrochemical doping that mainly injects electrons into the TiO_2 lattice, the super bandgap photo-excitation creates both holes and electrons in TiO_2 materials. The photoinduced electrons and holes trapped at gap states can be detected by optical spectroscopies. In principle, photoinduced absorptions are similar to that induced by an electrochemical doping. However, the involvement of electrolytes in electrochemical doping has an effect on an induced optical absorption for example, the H^+ absorption/insertion to TiO_2 materials may lead to a new gap state. The photoinduced light absorption can be conducted in many environments. In the vacuum condition, it was seen that the majority of electrons in a super band-gap excited a-TiO_2 exists in the form of free states, which gives rise to a broad featureless absorption with its intensity proportional to wavelengths that accords with the Drude theory ($A(\lambda) = C\lambda^p$, where λ is the wavelength (in μm), and C is a proportionality constant ranging from 1.5 to 3.5 [293]. The featureless absorptions in the IR region were also observed at low temperature and are also attributed to the intra-band free electron transitions [309]. In addition to this featureless IR absorption that is proportional to wavelengths, an additional broad peak at 3380 cm^{-1} was revealed by Yamakata et al.; this was attributed to the electron transition from an occupied monoenergetic surface gap state located 0.42 eV below the CB edge to a CB state [310] because the clearly defined peak shape is inconsistent with the notion of a continuum of exponential trap states below the CB edge [311].

In aqueous solutions, the electron charging of a nc-TiO_2 material associates with proton participations, so observing gap states by optical absorptions is affected by proton intercalation. McQuillan et al. found a pH-dependent mid-IR absorption peaked at 880 cm^{-1} in an aqueous solution under excitation with UV light illumination [312]. This peak does not correspond to the Drude-like free electron absorption and the phonon modes of TiO_2. It has been previously suggested that such broad IR absorption may originate from the transition of electrons from shallow gap states ~0.1 eV below the CB edge to the CB states, simultaneously accompanied by proton intercalation. They saw that the IR absorbance intensity rises with $[H^+]$, resulting in a near linear relationship between the peak maximum and the pH value when the pH is below 5 (Fig. 41(A)). The intensity and the persistence of this absorbance is greater at lower pH after terminating UV irradiations; this shows the important role of protons in forming the gap states that contribute to the absorbance. The presence of a low concentration formates, which captures the holes, greatly enhances this absorbance because of the increase of proton intercalation by more accumulated electrons. By considering that the gap state is formed by the electron localization coupling with the proton intercalation, a proton intercalation induced mechanism was proposed in Fig. 41(B). The physiochemical reason for this gap state is that the electron resides in a 3d orbital to form Ti^{3+} if localized. The charge-compensation effect drives the protonation of lattice Ti sites and further results in the stabilization of trapped electrons. Therefore, the chemical entity of this gap state, called the $(e^-)(H^+)$ pair, is slightly different from that illustrated in Section 3. With respect to the energy, they may partially contribute to the exponential band-tailed states below the CB edge because such states are located just 0.1 eV below the CB minimum. Intrinsically, it can be shown that the $(e^-)(H^+)$ pairs belong to the proton-assisted e-polarons, as revealed in another study [313] although the proton role in forming e-polarons is not obvious in the framework of polaron theory.

Simultaneous measurements that cover visible and mid-IR regions (400 nm to 10 μm) were performed on a-TiO_2 and r-TiO_2 powder to provide the information on the energy distribution of gap states, as well as the assignment of their chemical entities [314]. The super bandgap excitation of an a-TiO_2 produces the light absorption ranging over the entire region from 25,000 to 1000 cm^{-1} (Fig. 42(A)). The monotonic absorptions from 4000 to 1000 cm^{-1} are assigned to the intra-band transition of free electrons at CB extended states due to their accordance with Drude theory. In addition, the polarons are activated to be under thermal equilibrium with free electrons because of their small trap depth (0.1 eV), so the direct transition of shallow e-polarons at the free CB states can also contribute to this featureless absorption. On the other hand, the broad absorption ranging from 25,000 to 13,000 cm^{-1} was ascribed to absorption by electrons and or holes trapped at deep gap states. The spectral shape was almost independent on the a-TiO_2 types. By using O_2 and methanol to capturing electrons and holes, respectively, the decay processes were used to assign the physiochemical nature of these absorptions. The absorption at 2000 cm^{-1} is mainly attributed to free state electrons. The absorptions at 18,000 cm^{-1} and 22,000 cm^{-1} result from both the holes and electrons trapped at deep gap states, in line with other reports that the trapped holes and trapped electrons in a-TiO_2 present very broad absorptions [315].

The transient absorptions of a r-TiO_2 material is completely different from those observed for an a-TiO_2 material. It was seen that the absorption intensity increased with the wavenumber from 1000 to 25,000 cm^{-1}. There are two broad peaks at 22,000 cm^{-1} and 13,000 cm^{-1} (Fig. 42(B)). The low absorption below 4000 cm^{-1} indicates that the number of free or shallowly trapped electrons surviving on the μs time scale was much smaller than an a-TiO_2 material. The absorption at 13,000 cm^{-1} reflects the number of deeply trapped electrons that cannot be captured by O_2 atoms. The absorption at 22,000 cm^{-1} reflects the number of trapped holes. Different from a-TiO_2 materials, most of the electrons in r-TiO_2 materials were trapped at deep gap states; this leads to low reactivity as compared to the free or shallowly trapped electron generated in a-TiO_2. It is proposed by this research that the lower limit of the electron trap depth in a r-TiO_2 is 0.9 eV, much deeper than the 0.1 eV in a-TiO_2. This result is in good accordance with the electron localization at Ti sites form the small e-polaron in r-TiO_2 and the large

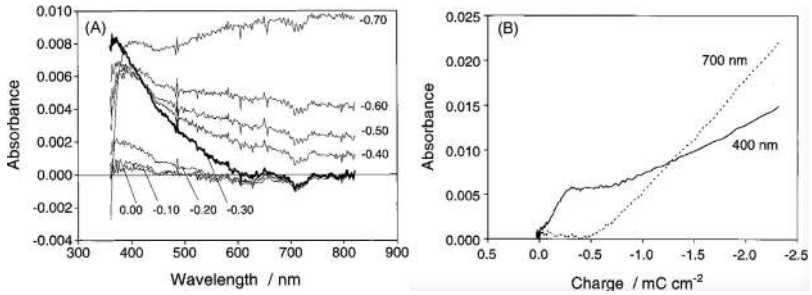

Fig. 40. (A) Absorption spectra of nanocrystalline TiO_2 as function of applied potential. Electrolyte: aqueous $LiClO_4$ (0.2 M), pH 6.2. Spectra are recorded after polarization for 5 min at the indicated potentials. The spectrum measured after stabilization for 15 min at +0.8 V has been subtracted. (B) Change in absorbance as function of accumulated charge.

Reproduced with permission from Ref. [308]. Copyright 1999 American Chemical Society.

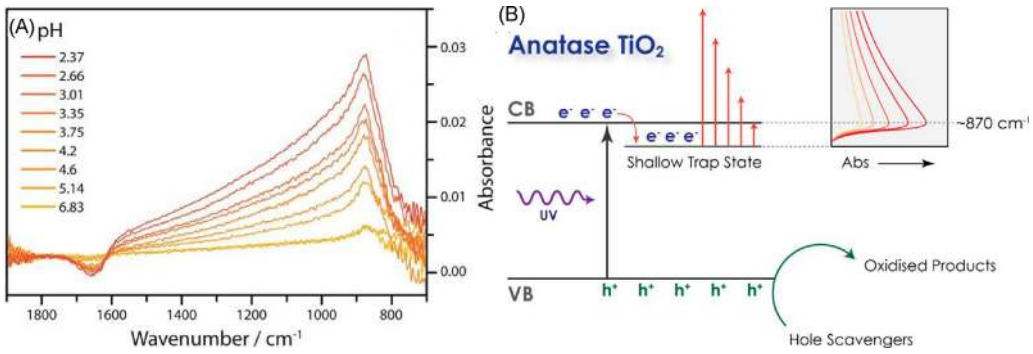

Fig. 41. (A) Spectral changes produced by UV irradiation of a-TiO_2 film with decreasing pH, backgrounds from the film in the dark at each respective pH. The spectra are offset to give equal absorbance at 1800 cm^{-1}. (B) Schematic mechanism for production of a proton-stabilized shallow electron trap state giving rise to the broad infrared absorption (STIRA).

Reproduced with permission from Ref. [312]. Copyright 2013 American Chemical Society.

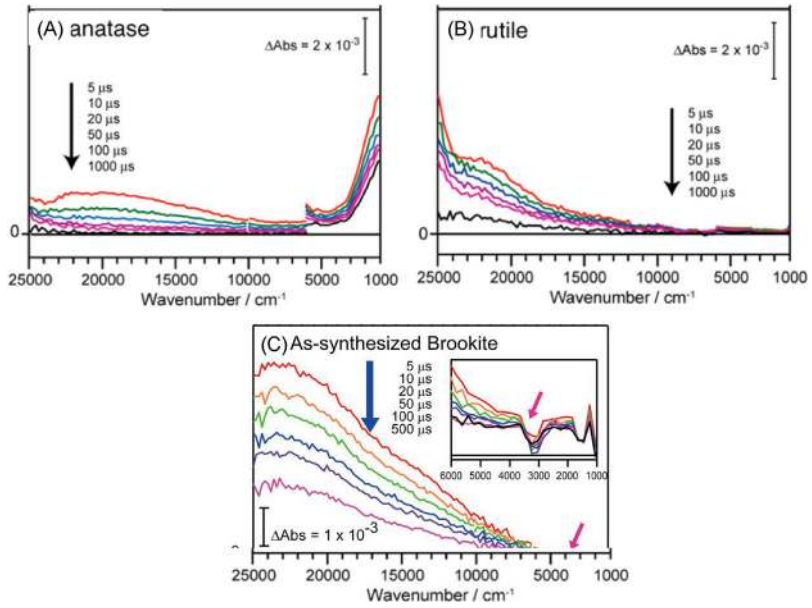

Fig. 42. (A) Transient absorption spectra of a-TiO_2 powder irradiated by UV laser pulses (355 nm, 6 ns duration, 0.5 mJ per pulse, and 5 Hz). (B) Transient absorption spectra of r-TiO_2: irradiated by UV laser pulses (355 nm, 6 ns duration, 0.5 mJ per pulse, and 5 Hz). Reproduced with permission from Ref. [314]. Copyright 2015 American Chemical Society. (C) Transient absorption spectra of r-TiO_2: irradiated by UV laser pulses (355 nm, 6 ns duration, 0.5 mJ per pulse, and 5 Hz). Reproduced with permission from Ref. [316]. Copyright 2017 American Chemical Society.

e-polaron or delocalized state in an a-TiO_2. Electron localization in r-TiO_2 is more stable than a-TiO_2 due to the large lattice distortion, which is the physical reason that the polaron localization in r-TiO_2 is deeper than a-TiO_2.

In addition to anatase, the transient absorptions are also measured to study the gap states in brookite TiO_2 (b-TiO_2) over a wide wavelength range from visible to the mid-IR [316]. Fig. 42(C) shows a broad adsorption over the entire wavenumber region from 25,000

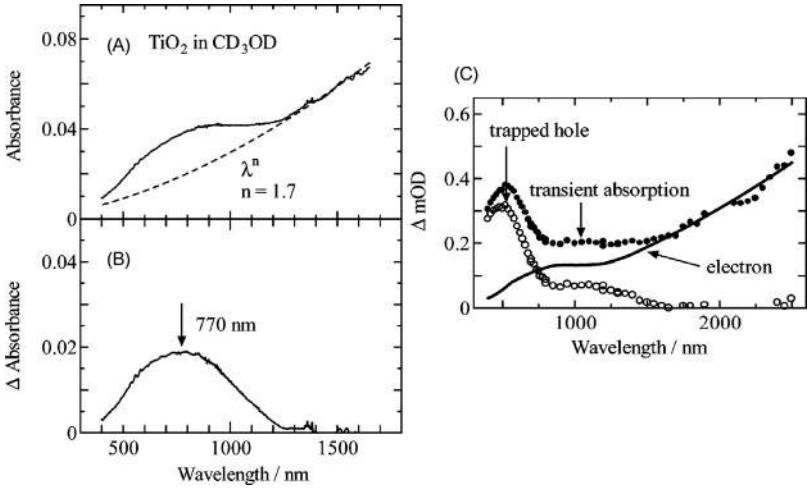

Fig. 43. (A) Absorption spectrum of a TiO_2 film in N_2-saturated CD_3-OD after irradiation with UV light for 30 min. The dashed line represents the theoretical curve λ^n, where $n = 1.7$. (B) Subtraction spectrum; (C) transient absorption spectrum of a TiO_2 film in N_2-saturated D_2O (•). The solid line (—) represents the absorption spectrum of electrons normalized in the near-IR wavelength range. The open circles (○) represent the subtraction spectrum.
Reproduced with permission from Ref. [317]. Copyright 2004 American Chemical Society.

to 3000 cm^{-1}. There are also two broad peaks appearing at 22,000 and 13,000 cm^{-1} that are assigned to electrons trapped at deep gap states. The little adsorption intensity below 3000 cm^{-1} also suggests low number of surviving free electrons on a μs timescale. Therefore, similar to a-TiO_2, most of the photoinduced electrons in b-TiO_2 are subject to trapping at deep gap states. The absorption edge is positioned at ~3500 cm^{-1} estimates that the gap states are mainly located 0.4 eV below the CB edge and have a wide distribution, which is almost insensitive to the particle morphologies and sizes. The influence of O_2 on transient absorption tends to become smaller and smaller with an increase of the wavenumber; this shows that the reactivity of electrons becomes lower and lower as the electron trap depth becomes larger. Because the absolute absorption at high wavenumbers is stronger than low wavenumbers, the density of deep gap states should be larger than the shallow gap states.

The gap states for trapping holes and those for trapping electrons were also clearly illustrated in a transient absorption study of nc-TiO_2 coating placed in heavy water and methanol-d4 (CD_3OD) [317]. Fig. 43 shows the transient absorption spectra of nc-TiO_2 film in N_2 saturated D_2O and the reproduced absorption spectrum of electrons normalized in the near-IR wavelength ranged above 1500 nm. An immediate reaction between the photoinduced holes and the methanol retains the electrons in nc-TiO_2 particles. The electron absorption spectrum cannot be simply explained by the free-electron spectrum. The broad free-electron absorption consists of the background of the absorption spectrum that was fitted with Drude theory (dashed line). Fig. 43(B) shows the broad spectrum obtained when the dashed line was subtracted from the solid line. The peak at 770 nm is assigned to the absorption band due to the locally trapped electrons other than the free electrons, in good agreement with other research [301]. The subtraction of transient absorption in the D_2O with that in the CD_3OD leads to the absorption of trapped holes, which has two peaks at 520 and ~1200 nm, as shown in Fig. 43(C). The peak position reflects the depth of gap states for trapped holes, and the holes with an absorption peak at 520 nm were trapped deeper than those with the peak at 1200 nm. In summary, the result shows that one monoenergetic gap state and two monoenergetic gap states contribute to the electron and hole trapping, respectively.

5.4. Photoluminescence (PL) spectroscopy

Radiative recombination of the photoinduced electrons and holes emits photons that can be detected by PL spectroscopy. The photoinduced holes and electrons are usually rapidly localized at gap states (traps) after their generation; this significantly limits the recombination of free holes and electrons, so the recombination in nc-TiO_2 materials mainly contributes to the trapped luminescence. Trapped electrons usually cannot recombine with trapped holes because they are immobile. The trapped holes and trapped electrons can form excitons if they are adjacent to each other (bound e-polaron and h-polaron). The resulting excitonic recombination mainly happens in a single-crystal TiO_2 and at low temperature. Therefore, the recombination in nc-TiO_2 materials is dominated by that between the trapped carrier and the free counterparts. Different recombination leads to luminance at different wavelength, which can also be partially used to indicate the energy distribution of gap states to some extents. A series of steady-state PL studies performed by McHale et al. proposed two types of recombination via traps in a-TiO_2 nanomaterials, as shown in Eq. (18) (type 1) and Eq. (19) (type 2) [318,319].

$$e^-_{CB} + h^+_{trapped} \rightarrow h\nu_{green} \quad (18)$$

$$h^+_{VB} + e^-_{trapped} \rightarrow h\nu_{yellow/red} \quad (19)$$

The green PL peaks (Eq. (18)) results from the recombination between free electrons and trapped holes, and two distributions of trapped electrons recombine with free holes to give yellow and red PLs (Eq. (19)).

These PL signals are broad and overlap each other. It was suggested by McHale et al. that the gap states for hole trapping locate 1.8–2.5 eV below the CB edge, and are also below the Fermi level as expected. The gap states for electron trapping are located 0.7–1.6 eV below the CB edge, also above the Fermi level as expected. This assignment of visible PL of nanoparticulate a-TiO_2 is generally in line with the research performed by Pallotti et al. [320]. As shown in Fig. 44, it is further suggested by Pallotti et al. that the yellow/red PL of a-TiO_2 can be excited by the intra-band gap excitation from the VB states to the shallow states, while the green PL cannot be obtained. They also proposed that partial electron-filling gap states

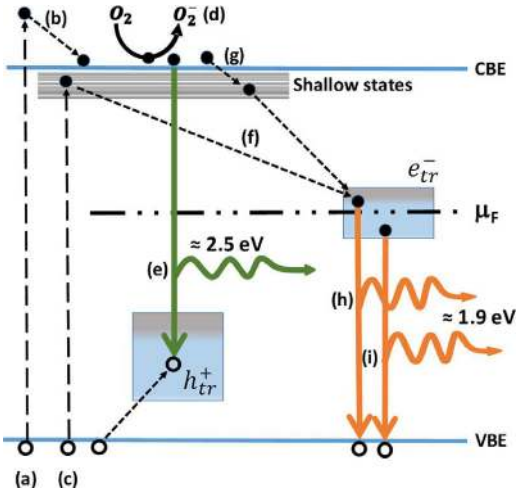

Fig. 44. Summary of anatase PL mechanisms of a-TiO_2: (a) band-gap excitation of hot carriers (b) hot electron relaxation; (c) excitation of band-tail states; (d) scavenging of free electrons by O_2; (e) recombination of CB electrons with trapped holes, with emission of green PL; (f, g) population of available electron trap states through relaxation of shallow states and CB states, respectively; (h, i) radiative recombination between trapped electrons and valence band holes. The red-PL emission can be caused by recombination of electron in states populated via relaxation (h) and by recombination of photogenerated holes with electron occupying state below the Fermi level before the laser excitation.

Reproduced with permission from Ref. [320]. Copyright 2017 American Chemical Society.

involved in Eq. (19) can energetically position below the Fermi level and are under a thermal-equilibrium with the empty ones, and thus occupied before optical excitations. Other initial empty gap states above the Fermi level can contribute from exponential band-tail states. The recombination of thermal-equilibrium electrons with free holes is as expected, not affected by O_2 adsorption, while the recombination of electrons above Fermi level can be clearly affected by O_2 adsorption.

The r-TiO_2 does not present visible luminescence, but emits a relatively narrow near-IR under band-gap illumination. It is also seen that the PL wavelength is dependent on surfaces. The (110) surface emits a NIR PL peak maxima at 810 nm and the (100) surface emits the NIR PL peak maxima at 840 nm [91]. For r-TiO_2 nanomaterials, the NIR PL peak emissions are usually between 810 and 840 nm because of many surface contributions [316,321]. It is shown by MacHale et al. that the emission of conventional r-TiO_2 powders slightly decreases after exposing to O_2 [322], but they also observed that a great increase of PL intensity for r-TiO_2 nanorod arrays occurs when exposed to air [323]. Pallotti et al. further saw that the change of PL intensity is irreversible on O_2 exposure. The trapping of charge carriers at gap states contributes to the NIR PL emission of r-TiO_2. It is suggested by MacHale et al. that the hole gap states are located ~1.5 eV below the CB edge and around the Fermi level, so the "type 1" recombination is possible in r-TiO_2, in line with the research [323]. However, Pallotti et al. considered that it is more plausible for the "type 2" recombination between free holes and the trapped electrons at the filled gap states ~1.5 eV below the CB edge. Therefore, the assignment of PL chemical nature is indirect and differs for the different studies. The PL spectra of P25 samples, or mixed r-TiO_2 and a-TiO_2 phases shows PL features that are different from the pure phase materials because of the mutual quenching of PL from red-emitting a-TiO_2 traps and near-IR rutile traps, which results from an inter-phasal electron transfer from a-TiO_2 to r-TiO_2 [320].

The chemical entities of gap states (hole and electron traps) were also indicated by investigating the change of PL spectra with some environment and morphological factors. For example, the intensities of "type 1" and "type 2" PL of a-TiO_2 nanomaterials both greatly decrease in the presence of O_2 due to the capturing of electrons. The exposure to O_2 changes the surface chemistry because O_2 would heal the V_O in a dissociative adsorption mode. The UV-induced free electrons can also provide some active sites for O_2 dissociative adsorptions. Such dissociative adsorption heals the surface of TiO_2 and decreases the V_O induced gap states. Based on these assumptions and the observation of irreversible quenching of PL for "type 1" emission, it is suggested that the hole traps are trapped at the V_O sites or the Ti sites adjacent to the V_O species. Therefore, it is considered that the green PL emission ("type 1") results from the hole trapped at surface Ti^{3+} adjacent to bridging V_O sites. Pallotti et al. attributed to the yellow "type 2" emission of a-TiO_2 nanomaterials to the electrons trapped at V_O, sites below the surfaces, whose photoinduced filling is supposed to be less likely than the surface V_O sites. It was also proposed that the NIR PL of r-TiO_2 may originate from the Ti(i) in r-TIO_2 materials. Based on the recombination mechanism shown in Fig. 44, the recombination of CB free electrons with the holes localized on 3-f O atoms (h-polarons) is also possible. In addition to O_2, the "type 1" PL and "type 2" PL emissions of a-TiO_2 nanomaterials are also sensitive to EtOH, MPN, and DMF, H_2O, and H_2O_2, showing the location of emission centers on surface regions. However, the r-TiO_2 PL emissions are less dependent on these solvents, indicating the location of emission centers below surfaces [84]. By studying the dependence of PL emissions on the morphologies of a-TiO_2 nanomaterials [324], the "type-2" red PL signals are further assigned to the radiative recombination between the trapped electrons on 5-f Ti sites (e-polarons) on the minority {001} surface with the VB free holes, and the hole trap PL emission ("type-1") is associated with the V_O species on the {101} exposed surfaces.

In the presence of electrolytes, the interactions between gap states and electrolytic ions have an effect on the redox potentials of gap states and the CB edge. The research performed by Knorr et al. studied the gap state activity of TiO_2 electrodes in an aqueous electrolyte as a function of pH and Fermi level control [325]. The potential-dependent PL spectra of an a-TiO_2 nanomaterial is shown in Fig. 45(A). The negative potential shift leads to an increase in the PL intensity and the shift of PL spectra to a short wavelength. The PL spectra change from the main "type 2" PL to "type 1" with a maximum emission at 530 nm when the potential was shifted from -0.2 V to 0.7 V vs. Ag/AgCl. The pH-dependences of a-TiO_2 PL intensities at 610 nm (Fig. 45(B)) show the proton-coupled Nernstian behaviors with the onset of PL emissions at 610 nm shifting to more negative potential as the pH increased. This PL results also show that the trapping process at gap states is coupled with the proton intercalation due to the pH-dependence of the PL onsets. These results support the assignment that the red PL emission is due to recombination of the trapped electrons with the VB holes, which is the reverse of the Urbach tail absorptions. The pH-dependent voltage at which the red PL emissions increase is accounted for by proton intercalation/absorption [326].

The red-emitting electron trapping gap states locate ~0.26 eV below the CB edge, possibly in the form of Ti^{3+} ions. The wide breadth of the red-PL results from the reorganization energy for the recombination of the trapped electrons (Ti^{3+}) with the VB holes, with possible contribution of the Jahn-Teller splitting of Ti^{3+} ions [327]. The Gerischer model associating the gap states with $Ti^{4+/3+}$ is used to estimate the gap state distribution. The density of gap states (N_t(E)) is taken to be a Gaussian distribution for which the standard deviation is $(2k_BT\lambda)^{1/2}$

$$N_t(E) = \frac{N_L}{(4\pi k_B T\lambda)^{1/2}} \exp\left[-\frac{(E - E_{F,redox\text{-}\lambda})}{4k_B T}\right] \quad (20)$$

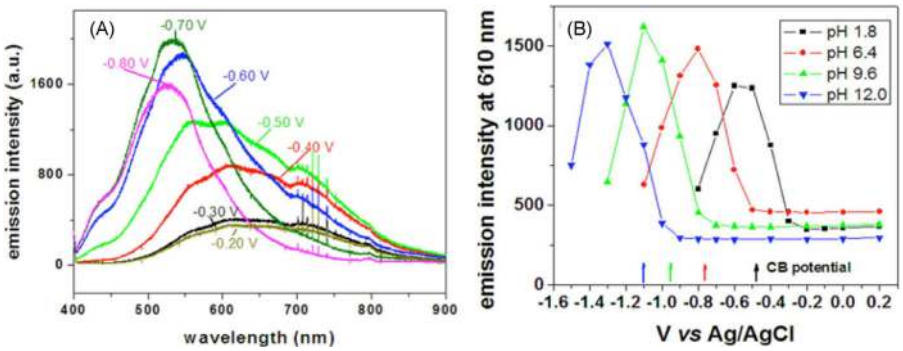

Fig. 45. (A) PL spectra nc a-TiO_2 at pH 1.8 in 0.2 M $NaClO_4$, excited at 350.7 nm at different applied potentials. (B) PL intensity of (a) a-TiO_2 at 610 nm and as a function of applied potential and at different pH (The excitation wavelength is 350.7 nm and the electrolyte is 0.2 M $NaClO_4$. The arrows denote the values of the CB potentials.
Reproduced with permission from Ref. [325]. Copyright 2013 American Chemical Society.

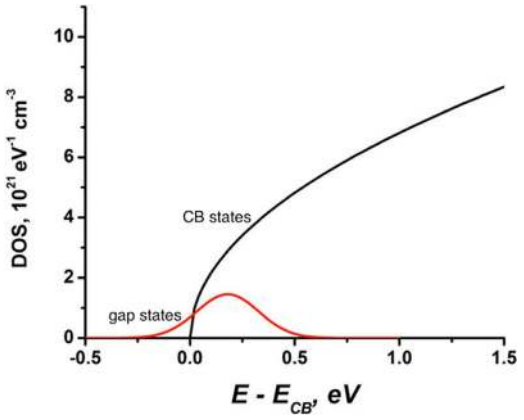

Fig. 46. Density of states (DOS) for conduction band (black) and trapped (red) electrons, estimated by using the data from Fig. 45(B) for the pH 9.6 sample as explained in the text.
Reproduced with permission from Ref. [325]. Copyright 2013 American Chemical Society.

where λ is the reorganization energy for the reduction of Ti^{4+} to Ti^{3+}, $E_{F,redox}$ is the Fermi level of redox couples, and N_L is the total energy density of gap states for trapping electrons. Taken an a-TiO_2 materials and pH = 9.6 into consideration, $E_{F,redox}$ is estimated from the voltage at which the intensity of red PL reaches half its maximum value, ~0.26 eV below CB edge. The λ is estimated from the width of half-heights of voltage-dependent PL intensity, 0.44 eV for the a-TiO_2 nanomaterials at pH value of 9.6. The total density of gap states is taken as $N_L = 2 \times 10^{20}$ cm^{-3}, in line with other study [318]. The center of the trap state distribution ($N_t(E)$) is at $E_{F,redox} + \lambda$; this moves the peak of $N_t(E)$ into the range of CB states. The distribution of CB edge states is described in a parabolic mode according to the following equation.

$$N_{CB}(E) = \frac{(2m^*)^{3/2}}{2\pi^2\hbar^3} E^{1/2} \quad (21)$$

where the effective mass m^* was taken to be equal to the mass of free electrons for simplification. The energy distribution of gap states and the CB states are shown in Fig. 46; this reveals that the partial gap state distribution below the CB edge is similar to an exponential band tail distribution. The assignment of such exponential band tail to Ti^{4+}/Ti^{3+} monoenergetic state distribution is different from the study, in which the exponential band tail is attributed to the uc-Ti atoms on surface [263]. This chemical nature assignment of the exponential band tail seems to be in coincidence with the study, in which it is attributed to shallow trapped states or polarons, coupled with H^+ intercalation. The spectroelectrochemical photoluminescence of a-TiO_2 nanosheets with more exposed {001} facets were studied and similar results were obtained besides that the red PL emissions make a much larger contribution at less negative bias because the red traps (electron traps) are favored on the {001} surface [328,329]. Many first-principle calculation and experimental studies show that the {001} surfaces resist electrons residence due to their high surface energy. This PL study gives an interesting result that electrons can also be trapped on {001} surfaces if more defect-induced gap states are implanted. Different from the a-TiO_2 nanomaterials, it is also seen that the near-IR PL of r-TiO_2 nanowires does not shift with electrochemical potentials, indicating their location in bulk [321].

Although the studies of facet-dependent redox behaviors suggest that the preferential occurrences of electron transfer and hole transfer on a-{101} surfaces and a-{001} surfaces, respectively [330,331], the role of spatially-distributed isolated trap sites (gap states) on these surfaces is still uncertain. The above PL spectroscopical study proposed that the primary localization of the electrons and the holes occurs on {001} facets at Ti_{5c} sites and on {101} at V_O sites, respectively [324]. In recent research [332], imaging PL emissions of single μm-scaled a-TiO_2 crystals was used to study the spatial-distribution of trapped sites for electrons and holes. The a-TiO_2 microcrystal (Fig. 47(A)) with both exposed {101} and {001} surfaces were synthesized by a HF assistant hydrothermal method [333]. The {001} surfaces of un-annealed sample were capped with F^- cations that can be further removed by a post-annealing at 600 °C. Fig. 47(B) shows the PL spectra of un-annealed single crystals that feature the PL emissions of a-TiO_2, involving both "type 1" and "type 2" recombination, which was further enhanced 5 times by post-annealing. Fig. 47(C) and (D) shows the PL spatial distribution of annealed and unannealed samples. It was seen that the post-annealing changes the main spatial distributions of PL emissions from the edges to center of a (001) surface. The luminescence imaging of grouped particles for the un-annealed and annealed samples also revealed the appearance of remote PL particles away from the excited point due to the presence of inter-particle charge carrier transport. Because the PL of un-annealed particle groups occurs most strongly from edges and corners, the spatial distribution of PL is affected by a directional charge carrier transport and a spatial distribution of radiative recombination sites (gap states) which favor edges and corners. Based on these observations, it was further explained that the broad red PL emissions mainly result from the recombination between the VB holes and the electron trapped at surface Ti_{5c} sites. The passivation of these traps by fluorine cations on the as-prepared samples effectively prevents these sites from trapping the electrons. The post-annealing removed the surface capped fluorine cations and may induce the (1×4) reconstruction to {001} surfaces; this may create more gap

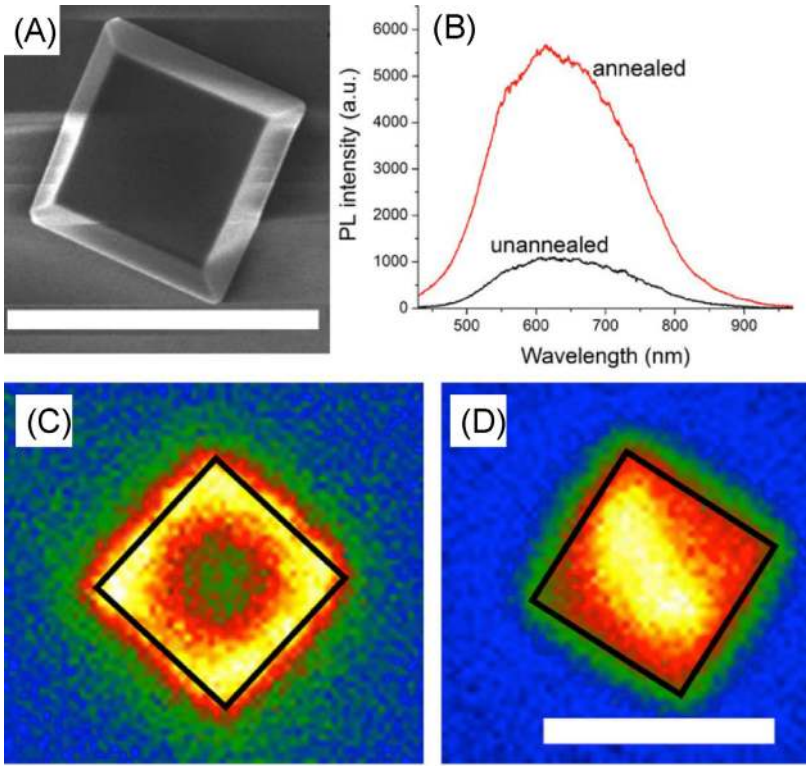

Fig. 47. (A) SEM micrograph of a-TiO_2 micro crystal (the scale bar is 5 μm); (B) PL spectra of an unannealed and annealed a-TiO_2 samples under wide-field 350 nm excitation. Unannealed crystal (C) and annealed crystal (S) illuminated by wide-field 350 nm excitation. The scale bar indicates 3 μm.
Reproduced with permission from Ref. [332]. Copyright 2015 American Chemical Society.

states available for electron trapping and result in the Gaussian distribution of PL light.

6. Intermediate gap state mediated charge carrier kinetics

The overview of charge carrier kinetics mediated by the gap states in TiO_2 materials is illustrated in Fig. 48. Different from single-crystalline materials that are free of defects, the dominant function of gap states in charge carrier kinetics is their role in trapping electrons and holes; this can have a significant effect on the transport of charge carriers, their interfacial transfer, as well as the recombination. The above section illustrates the function of gap states as trapping centers of charge carriers and some induced physiochemical properties. This section mainly elaborates on the kinetic features of the trapping and the associated transport, recombination, interfacial transfer, as well as photocatalytic activities.

6.1. Charge carrier relaxation and trapping

After super bandgap excitation, the photoinduced charge carriers (the electrons and the holes) are firstly located at high energy levels of the CB states and the VB states and quickly relax into their corresponding band edges by interacting with the TiO_2 lattice. Further relaxation of these to gap states happens over a longer time period and is called a trapping. The gap states play a significant role in trapping both the electrons and the holes. Trapping processes can take place at real defect induced gap states, for example these intrinsic defects of the V_O, Ti(i), and OHs entities, as summarized in Section 2. In many cases, self-trapping of charge carriers at corresponding regular lattice sites of TiO_2 materials can naturally lead to the formation of gap states, as illustrated in Sections 3 and 4. The trapping processes are found to be dependent on the crystalline structures of the TiO_2 materials, the gap state location, the gap state energy distribution, and the surface chemical environments [334–336].

Trapping time is usually used as a main physiochemical parameter to characterize the trapping processes; this is found to be dependent on a specific trapping process. A recent review paper summarized the lifetimes of electron trapping and hole trapping in TiO_2 materials [9]. Trapping of the VB free holes mainly happens on surfaces on a femtosecond (fs) timescale, while trapping of the CB free electrons was found to be dominant in bulk and differs for shallow trapping in a timescale range from several hundred fs and several tens of picosecond (ps), respectively. The electrons tend to be firstly trapped at shallow gap states due to their high density, and the further relaxation of shallow trapped electrons to deep gap states needs a much longer time. For example, our recent random walking model indicates that it is unlikely for a photoinduced electron to relax to a thermodynamic distribution at deep gap states before interfacial transfer to O_2 [37], which is supported by a result that observed a contribution of non-thermalized photoinduced electrons to the anodic photocurrents [263].

Ultra-fast transient absorption spectroscopy is the main method that is used to study charge carrier trappings in TiO_2 materials. The trapping times are obtained by analyzing and modeling the dynamic decays of transient optical absorptions induced by trapped electrons, trapped holes, and free electrons. It was shown by analyzing transient absorptions that the electron trapping in TiO_2 materials is dependent on crystalline polymorphs due to the different depth of gap states [316]. Fig. 49(A) shows that the trapping of free electrons from the CB extended states to the gap states in b-TiO_2 powders leads to a simultaneous decrease in free electron absorption at 2000 cm^{-1} and an increase in trapped electron absorptions at 22,000 cm^{-1} and 14,300 cm^{-1}, respectively. This correlation shows fast trapping of free CB electrons on a ps timescale, resulting in a thermal statistical distribution among the trapped

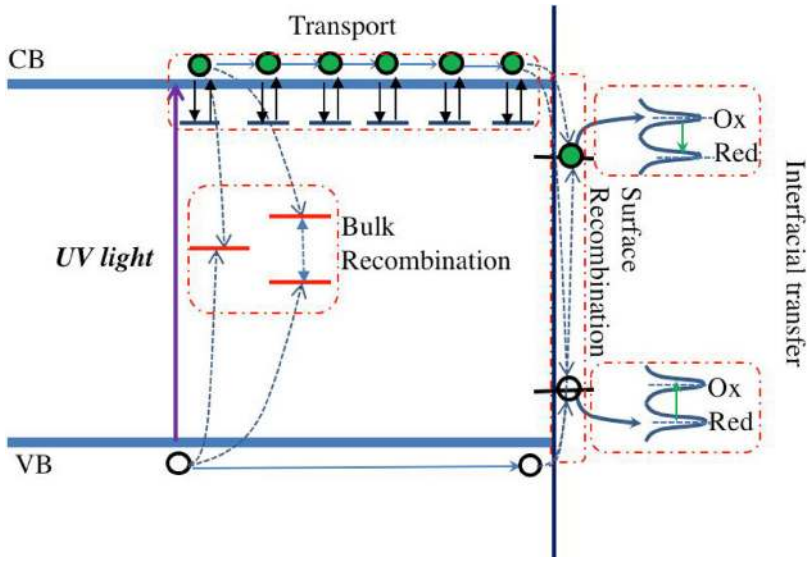

Fig. 48. Schematic illustration the roles defect-induced energy levels in charge carrier kinetics.

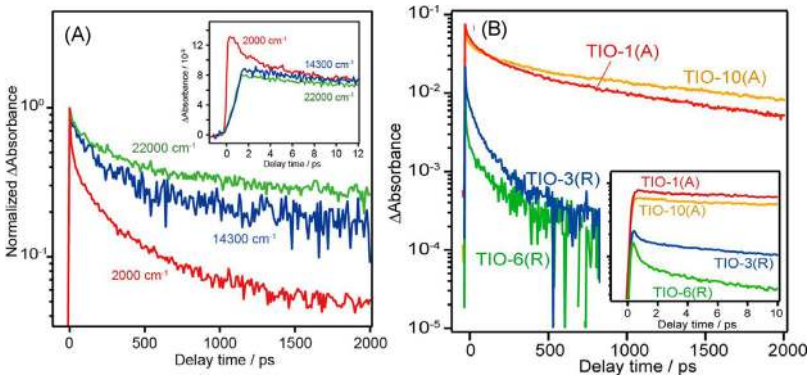

Fig. 49. (A) Decay curves of free electrons (2000 cm^{-1}) and deeply trapped electrons (14,300 and 22,000 cm^{-1}) in as-synthesized b-TiO_2 powders measured by UV laser pulse irradiation in vacuum Reproduced with permission from Ref. [316]. Copyright 2017 American Chemical Society. (B) Decay curves of free electrons in polycrystalline a-TiO_2 and r-TiO_2 samples measured in vacuum at 2000 cm^{-1}. Reproduced with permission from Ref. [314]. Copyright 2015 American Chemical Society.

and the untrapped electrons. Fig. 49(B) shows the transient decay of the free CB electron absorptions at 2000 cm^{-1} for r-TiO_2 and a-TiO_2 powders. The density of free electrons in a-TiO_2 is much higher than that in r-TiO_2, and the decay rate of transient absorption for free CB electrons is the same as that of the electrons and the holes trapped at deep gap states of a-TiO_2 due to fast shallow trapping, which allows a long lifetime of free CB electrons to the ms region. Differently, the transient decay of free CB electron absorption is mainly dominated by the rapid trapping at deep gap states on a ps scale in r-TiO_2. This is similar to the case of b-TiO_2, but the trap depth is deeper in r-TiO_2 than b-TiO_2 [316]. The trapping effect leads to a result that the recombination between the free CB electrons with holes cannot dominantly happen in a direct way because of the faster decay of free electrons than holes. In addition, the free electrons in a-TiO_2 have a high probability to participate in photocatalysis due to their long lifetime, resulting in the generally-observed higher activity of a-TiO_2 than the other polymorphs.

Such ultra-fast electron trapping is considered to mainly take place at shallow gap states of TiO_2 materials, and a similar result was also observed for the hole trapping [337]. In addition to these ultra-fast trappings, the further trapping of electrons from shallow gap states to deep ones needs much longer times (~500 ps) [338]. By involving these ultra-fast trappings and the subsequent slower ones, the overall trapping processes and the energy levels of associate gap states were shown in Fig. 50. The electrons trapped in bulk and the holes trapped on surfaces can separate in space and have long lifetimes, which helps to increase the photocatalytic activity of TiO_2 materials to some extent. A similar conclusion was also drawn in this research that the immediate trapping of free CB electrons occurs at surface gap states and the rest trapped at shallow and deep bulk gap states are under thermal equilibrium at room temperature.

In addition to these trapping processes within a ps timescale, recent research observed an interesting ultra-slow electron trapping process in TiO_2 colloids containing methanol as the hole capturers by combining EPR and UV-Visible spectroscopy [339]. Under super bandgap light excitation, two electron trapped gap states, totally denoted as TiO_2/e^-, were revealed, as shown in Fig. 51(A). One is the photoinduced "red" electron absorption at 1.67 eV (red/e^-); the other is the "blue" absorption at 2.66 eV (blue/e^-). They are attributed to the d-d optical transitions observed at Ti^{3+} ions and the intervalence charge transfer within Ti^{3+}-containing materials. Importantly, the reversible shift of the trapped electrons from the "blue" to the "red" trapped states was seen to happen when the temperature increases, which has an enthalpic difference of 0.13 eV (Fig. 51(B) and (C). The transfer of electron trapping between the above two trapped states at different temperatures is very slow and lags several minutes to hours behind

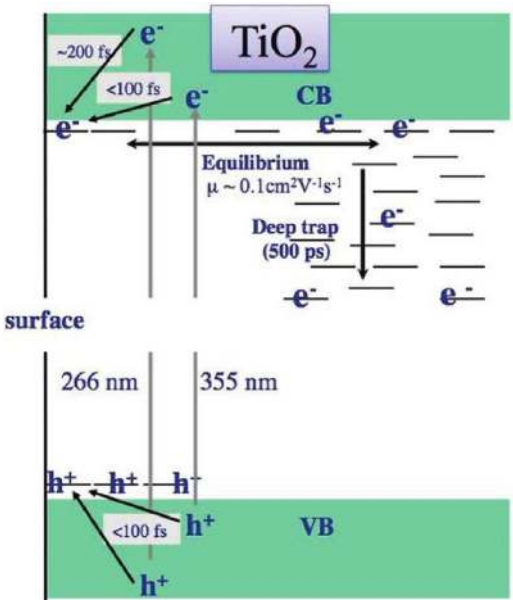

Fig. 50. Scheme to explain the trapping and relaxation dynamics of electrons and holes in TiO_2 excited at 266 and 355 nm.

Reproduced with permission from Ref. [338]. Copyright 2009 American Chemical Society.

changes in sample temperature. Such slow electron re-trapping at different gap states can allow a corresponding lattice change, so this finding indicated that the lattice structural change at different gap states should be involved in this electron re-trapping, whereas the ps timescale re-trapping from shallow gap states to deep gap states is too fast to have a lattice contribution.

The gap states on surfaces are sensitive to different chemical environments, so the charge carrier trapping on the surface is found to be dependent on surface chemistry. In recent research, the transient IR absorptions of free CB electrons were monitored to investigate the role of water molecular adsorption in trapping photoinduced holes [340]. It was shown that the photoinduced electron IR absorption firstly increases and then decreases with water-vapor partial pressure and changes in the layers of water on the TiO_2 surfaces. By combining a steady IR analysis and a first principle calculation, they concluded that the first layer water molecules strongly interact with TiO_2 surfaces and are capable of trapping photogenerated holes. The further adsorption of a second layer water reduces the hole trapping due to the weakening of the interaction with first-layer water on the TiO_2 surfaces. The water adsorption depletes the electron density at Ti_{5c} sites and accumulates along the H bonds between the H of water and the surface O. Therefore, it is probable that the excess electron density in H bonds is the origin of trapping of generated holes. The trapping of photoinduced holes at H bonds is also on the ps timescale.

The super bandgap light illumination creates both electrons and holes. The trapping of photogenerated electrons and holes as excitons was also seen in TiO_2 materials in addition to the individual trapped species. In a study of frequency- and time-resolved microwave conductance (FTMC) measurements on TiO_2 nanotube arrays prepared by anodizing a titanium plate, it was seen that a second photo-physical product characterized with a large imaginary photoconductance was required to model the $\Delta P(\omega,t)/P$ contour plots; this was contributed to excitons. Based on the FTMC measurements, a relaxation of free CB electrons and VB holes at exciton states was proposed. Firstly, the initial photo-excitations generate hot excited states ($(TiO_2)^*$) with an energy exceeding the band gap of TiO_2, which are then thermalized to energies near the band gap, yielding the states of relaxed $(TiO_2)^*$. It was proposed that this relaxed state corresponds to an electron and a hole residing within their mutual Coulomb potential. The reversible shift between a free state and the self-trapped exciton state can be modulated by changing temperatures. It was revealed that the relaxation of a free state to a self-trapped excitonic state happens on a sub-ns timescale, which has a longer lifetime on a ms timescale before recombination with a hole [341].

6.2. Trapping limited charge carrier transport

It was reported that the electron transport in nc-TiO_2 materials is mainly dominated by a diffusion modulated by gap state trapping, so it is much lower than that in a form of the free CB state [342]. At the same time, charge carrier transport is also accompanied with the loss of charge carriers due to recombination and interfacial transfer. In nc-TiO_2 materials, the drift mobilities of charge carriers driven by a microscopic electric field is found to be unimportant due to the small size of nanoparticles and the screening effect of the electrolyte, so the electrons mainly move in a diffusion-dominated way that is driven by the gradient of the electron Fermi level [343,344]. By involving the trapping effect of gap states, the thermodynamic driving force for electron transport in nc-TiO_2 materials were investigated by a theoretical analysis [344].

The dynamic characteristic parameter that is used to describe the electron diffusion is the chemical diffusion coefficient (D_n), which were defined from phenomenological approaches [345]. The D_n of electron transport in free states is independent on charge carrier densities and generally large. However, the trapping effect

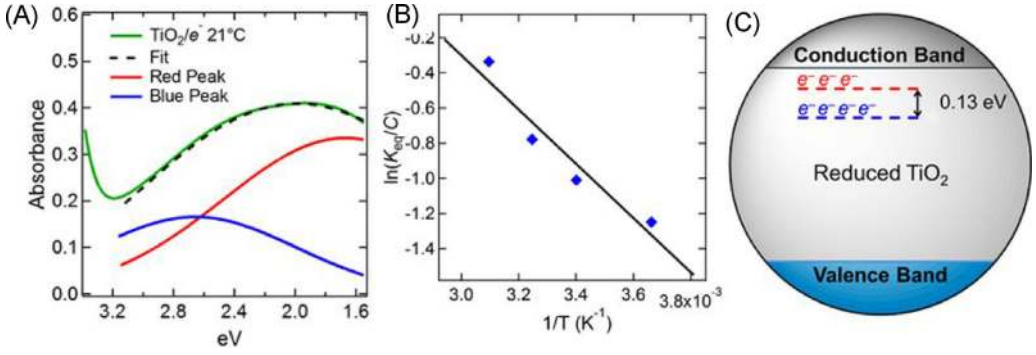

Fig. 51. The spectrum of TiO_2/e^- at 21 °C plotted vs eV (green) and the optical fit (black, dashed) composed of two broad Gaussians (red and blue). (B) van't Hoff plot of K_{eq}/C determined from the ratio of the Red/e^- and Blue/e^- EPR components of TiO_2/e^- samples preequilibrated to 0–50 °C. (C) A simplified band diagram showing Red/e^- and Blue/e^- as intraband gap states.

Reproduced with permission from Ref. [339]. Copyright 2017 American Chemical Society.

of gap states limits the electron transport kinetics in a nc-TiO_2 network. The D_n was also found to vary with the density of electrons [346,347]. Several models involving the roles of gap states were proposed to describe electron transport in nc-TiO_2 networks, which mainly include the multi-trapping model that includes the CB extended states [348,349] and the hopping model that does not include the CB extended states [350]. Assuming the multi-trapping of electrons occurs within the frame of multiple trapping model with an exponential density of band gap states, the D_n can be expressed in terms of the total photoelectron density (N_e) and the effective density of trap states (N_{CB}) at the transport edge (CB edge).

$$D \approx D_0 \left(\frac{N_e}{N_{CB}}\right)^{((T_0/T)-1)} \quad (22)$$

where D_0 is the diffusion coefficient of freely mobile electrons at or above the transport edge of the nano-TiO_2 materials. Based on the multi-trapping or the hopping mechanism, continuous time random walking models were also developed to simulate the electron dispersive transport in nc-TiO_2 materials by Nelson, us, and the other researchers [351,352]. Under a reasonable assumption that the time of electron transport in the CB extended states is much shorter than a trapping time, Tachiya and co-workers developed a random flight model, where the probability for a de-trapped electron to be trapped by an empty gap state is not limited within nearby traps [353]. They established numerical and approximate analytical solutions that fitted well with the experimental data observed by Haque et al. [354].

The thermodynamic small perturbation, such as the intensity modulated photocurrent spectroscopy (IMPS), is an usual method to study multi-trapped electron transport in nano-TiO_2 materials. For example, an IMPS study conducted by de Jongh et al. showed that the electronic transport in nc-TiO_2 is limited by the multi-trapping at gap states with high density exponentially distributed with respect to the energy [355]. For the IMPS, the light intensity absorbed in nc-TiO_2 consists of a background intensity (Φ) and a small amplitude harmonic component ($\Phi(\omega)$), which gives rise to a steady state photocurrent density Δ(i) and a harmonically varying photocurrent density (Δ(i)(ω)), respectively. The frequency at which the imaginary component of Δ(i)(ω) shows a minimum is denoted by ω_{min}. The ω_{min} is proportional to the reverse of transit time (τ_d) of an electron crossing over a nc-TiO_2 network, which can be further used to estimate the D_n. A linear increase of τ_d with the square of Φ, shows the trapping of photogenerated electrons at gap states in the course of electron transport. In research performed by Chen et al., the IMPS was used to study the electron transport in an O-deficient TiO_2 nanorod array obtained from a hydrothermal method and a further reduction. The D_n was determined and its dependence on light fluxes are shown in Fig. 52(A). The results revealed two electron-transport modes, a trap-free transport mode at the core and a trap-limited transport mode near the surface, are present for the O-deficient TiO_2 nanorod array, while the pristine TiO_2 nanorod array only show a single trap-limited mode. This difference in electron transport is ascribed to the different distribution of oxygen defect induced gap states along the radial-direction in TiO_2 nanorods, as shown in Fig. 52(B) [356]. Because oxygen defects are the main chemical entities of gap states, the charge carrier transport can be modulated by engineering their spatial distribution. Dai et al. studied the effect of surface state modulation on the electron transport time in a TiO_2 sub-microsphere electrodes by combining an electrochemical CV and an IMPS. It was found that the addition of ammonia in hydrothermal reactions can increase electron transport speed due to its role in decreasing surface state density of TiO_2 sub-microspheres [357]. Villanueva-Cab used temperature-dependent IMPS to determine the trap-free electron diffusion coefficient in nanotube array and nanoparticle TiO_2 by removing the trapping effect of the gap states, i.e., the D_0 in Eq. (22). Although the D_0 is independent on gap states, it is also affected by structural disorder, such as crystalline size and crystallite interconnection. According to Eq. (22), the D_0 of TiO_2 materials can be obtained by extrapolation of the power-law dependence of D on N (electron density) at different densities. Fig. 53(A) shows the determination of D_0 of TiO_2 nanoporous films sealed in a dye-sensitized solar cells according to the above method. The D_0 is estimated to be 1.4×10^{-3} cm^{-2} s^{-1} for the 15 nm nc-TiO_2 film containing 60% nanopores. They found that the D_0 increases with grain size in a square-foot law (Fig. 53(B)) and tends to the D_0 of single-crystalline material for an infinite grain. The D_0 of nanotube TiO_2 was also determined according to the same method (Fig. 53(C)), which is found to be 1.4×10^{-1} cm^2 s^{-1}, much higher the particle TiO_2. It is considered that the structural disorder associated with the individual particles determine the different D_0 of nanotube TiO_2 and particle TiO_2 nanoporous films [358].

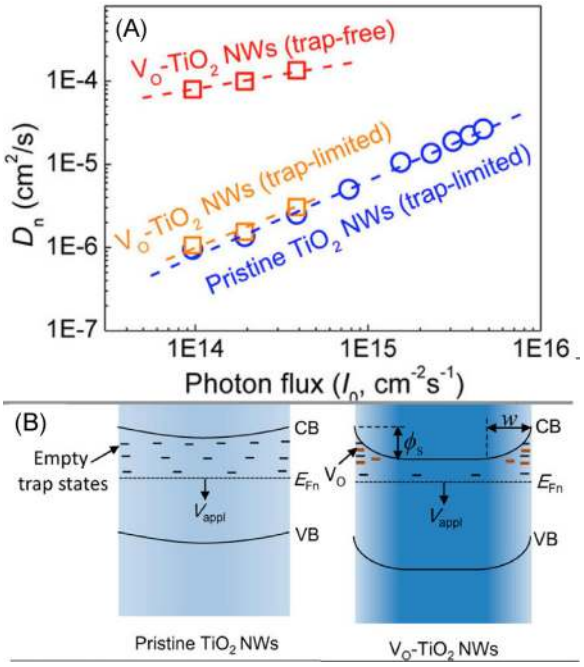

Fig. 52. (A) Extracted D_n from the IMPS complex plane plots. (B) Schematic energy diagrams and trap state distributions of pristine TiO_2 NWs and (D) V_o-TiO_2 NWs. Reproduced with permission from Ref. [356]. Copyright 2014 American Chemical Society.

A quasi-continuous wave (cw) optical absorption measurements while simultaneously electronically measuring the conductivity through in-plane devices was developed to probe the electron transport in a dye-sensitized nc-TiO_2 films. The density of electrons injected from dye to nc-TiO_2 was determined by optical bleaching of dye absorption. The photoconductance was determined by conductivity measurement. The electron mobility was estimated according to $\mu = \sigma/ne$, where σ and n are the photoconductance of nc-TiO_2 film and the density of electrons in nc-TiO_2. Their experiments revealed a special result that there exists a strong electron density dependence which diminishes when the temperature is reduced from 295 K. However, the electron mobility becomes almost independent on electron density at temperature below 260 K. This leads to the fact that the mobility firstly increases and then decreases with reducing temperature. By combining the Monte-Carlo simulation within multi-trapping model, it is possible that the average trap depth becomes deeper and the density of states become more disordered with an increase of temperature [359].

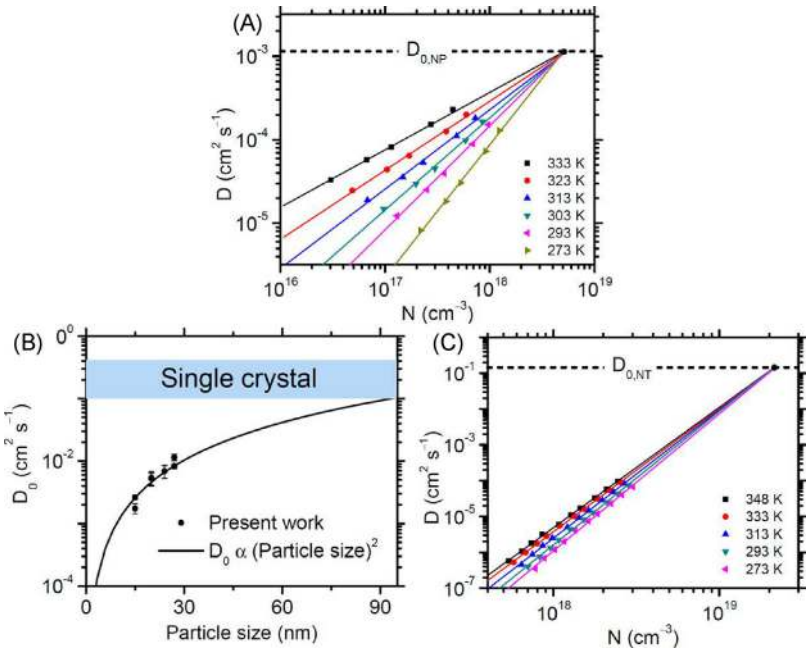

Fig. 53. (A) Temperature dependence of the electron diffusion coefficient on the photoelectron density in a DSSC containing a TiO_2 nanoparticle film. The average crystallite size is 15 nm, and the film porosity is 60 ± 2%. (B) Effect of the average crystallite size on the trap-free electron diffusion coefficient D0 in nanoparticle films used in various DSSCs. The average crystallite size ranges from 15 to 28 nm, and the porosity of the films is 60 ± 2%. (C) Temperature dependence of the electron diffusion coefficient D on the photoelectron density in a DSSC containing a TiO_2 nanotube film.
Reproduced with permission from Ref. [358]. Copyright 2014 American Chemical Society.

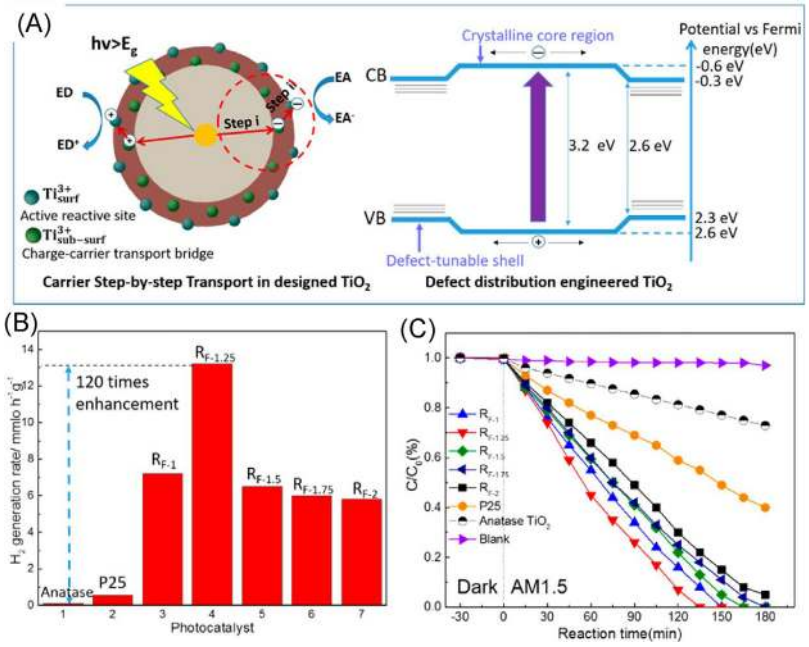

Fig. 54. (A) Carrier step transfer mechanism in designed TiO_2 with band alignment and shallow traps; (B) photocatalytic hydrogen generation (B) and methyl orange degradation for samples with different ratios of sub-surface to surface Ti^{3+} cations, which 0.18, 0.34, 1.2, 1.46, and 1.6 for the samples R_F-1, R_F-1.25, R_F-1.5, R_F-1.75, and R_F-2.
Reproduced with permission from Ref. [360]. Copyright 2017 American Chemical Society.

The limitation by trapping in electron transport may limit photocatalytic processes, so the photocatalytic activity can be changed by modulating the multi-trapping transport. By tailoring defect distribution to create a crystalline core/defect-tunable shell structure through a F anion induced dynamic reaction method, it was proposed that the moderate shallow gap states caused by sub-surface defects bridge electron transfer from bulk to surfaces, which was called a step-by-step transport, as shown in Fig. 54(A), left. It was suggested that controlling the defect distribution on surfaces and sub-surfaces can establish a special band matching (Fig. 53(A), right). This gradient band alignment favors a fast charge transfer from bulk to surfaces and subsequently results in a much higher photocatalytic hydrogen evolution and methylene blue degradation than the crystalline anatase TiO_2 under solar light illumination when ratio sub-surface Ti^{3+} to surface Ti^{3+} is 0.34 (Fig. 54(B) and (C)). This research showed that engineering the defect distribu-

tion to modulate electron transport is an effective way to increase photocatalytic activity [360].

The trapping effect of gap states on electron transport can be altered by manipulating the pre-occupation of electrons at gap states. The multi-trapping model shows that the probability for trapping the free CB electrons at gap states can be lowered by filling deep electron traps. The general methods used for pre-occupation include a continuous bias light illumination and an electrochemical electron Fermi level control [361]. The apparent diffusion length can be increased by two times as much as that without additional bias light, which allows electrons to have a bigger change to reach the collection electrodes for reductions. The apparent diffusion length was increased by about five times by a decrease of the electrochemical potential from +0.5 V vs SCE to −0.2 V vs SCE. Moreover, it was also found that the trapping effect on electron transport can be altered by coupling with some small cations, such as H^+ and Li^+, because the diffusion of these small cations alongside the electrons is beneficial to stabilize the shallow trapping sites, and eventually facilitate electron diffusion in TiO_2 materials [362].

The trapping effect also let the gap states play an important role in electron interparticle transport in TiO_2 materials. It is usually considered that the photoinduced electrons simultaneously transfer from anatase to rutile particles for mixed phase TiO_2 materials, such as commercial P25, which is driven by a higher CB edge position of anatase than rutile. By selectively exciting rutile by visible light illumination, an EPR study provided solid proof for electron transfer from rutile to anatase [363]. Because the high-energy CB edge position of anatase does not allow electron transfer by band states, it was proposed that the electrons may transfer to the gap states of anatase phase that are relatively lower than the rutile CB edge. Such rutile-to-anatase electron transfer was also supported by another study [364]. In addition, a theoretical study showed that the localization of electrons at grain boundaries is favorable in energy, so it was considered that the boundary gap states are important in limiting electron transport [365]. By combining a first principle modeling and a kinetic Monte-Carlo (KMC) simulation, the effect on trapping and mobilities was studied in a rutile $\Sigma(210)[001]$ tilt grain boundary. The result showed that the perturbations in electrostatic potentials are responsible for a high density of strong trapping sites at grain boundaries, which was stated to be the main reason hampering electron interparticle transport. By pre-filling the boundary sites by an electrochemical reduction, the photocurrents were greatly increased due to an increase in electron transport along a nc-TiO_2 electrode [366].

The multi-trapping and hopping model suppose the importance of gap states. However, what kinds of gap states are involved are not illustrated. Based on the discussion in above Sections, it seems that both real defects and polarons can contribute to the gap states. A few researchers have indicated that the polarons may play the role of trapping for charge carrier transport in TiO_2 materials. The summaries in section 3 show that the electrons and the holes can be self-trapped as small polarons in a perfect stoichiometric TiO_2 lattice. The small polarons are mobile along different lattice directions under thermal activation. Fig. 55 shows the mechanism of electron transport in a lattice via polaron hopping in a potential energy landscape with local minima originating from self-trapping lattice sites [368]. It was showed that an e-polaron is ∼2 times larger than its hole counterpart for TiO_2, so the hopping diffusion of e-polarons is faster than the h-polarons. A recent luminescence imaging on the F-{001} caped single anatase crystal revealed the possible e-polaron hopping through neighboring Ti lattice sites [342], and it was speculated that the e-polaron hopping is somewhat more favorable along the equivalent crystallographic *a* and *b* directions than in a diagonal direction owing to the shorter near-neighbor distance, resulting in a fourfold symmetry of PL images [342]. It was also thought that the small polaron transport may be important for metal oxide photoanodes for water oxidations in other publication [368].

In addition to polarons, the transported mobility of charge carriers limited by exciton-like gap states was also suggested by a sub-ps time-resolved terahertz spectroscopic (TRTS) study [264]. This study revealed that the low electron mobility of TiO_2 nanotube arrays cannot be attributed to a trapping effect that is related to a single trap, but to a bound exciton. A distinct resonance at ∼7.5 meV appears in the terahertz conductivity spectrum of TiO_2 nanotubes and was attributed to an exciton-like entity because it fitted well with a single classical Lorentz oscillator. The hydrogenic model estimated an excitation binding energy of 11.2 meV. The transition energy from the ground state to the first excited state is 8.4 meV for the exciton, in good agreement with the experimental value. Under the photoexcitation of dye-sensitized TiO_2 nanotubes, because more electrons were injected from dyes to TiO_2, the significant increase of bound exciton states can lead to a stronger resonant feature in the frequency-dependence photoconductivity.

The trapping modulated mobilities (μ) or chemical diffusion coefficient (D_n) of charge carriers in TiO_2 materials were determined by many studies. Based on the TRTS spectra of P25 nc-TiO_2 electrode [369], it was shown that the ac electron mobility is about 15 $cm^2\,V^{-1}\,s^{-1}$, and the dc electron mobility is 10 times less than the ac mobility, which is about 1.5 $cm^2\,V^{-1}\,s^{-1}$. Both of them are much lower than that of a single-crystalline r-TiO_2 (50 $cm^2\,V^{-1}\,s^{-1}$). Because the TRTS study also revealed a much higher electron mobility in the inside of nanoparticles, the low electron mobility is ascribed to disorder induced trapping on surfaces or boundaries. It was also determined by a TRMC measurement that the maximum mobilities of electrons in the P25 and the Solarnix TiO_2 nc-TiO_2 electrodes are ∼0.08 and 0.3 $cm^2\,V^{-1}\,s^{-1}$, respectively [370]. An electrochemical study also showed that the electron mobilities in a large single TiO_2 crystal and a nc-TiO_2 thin film were ∼15 and 1.9 $cm^2\,V^{-1}\,s^{-1}$, respectively [371,372]. An analysis of the transient absorptions of bulk trapped electrons in nc-TiO_2 estimated a bulk electron mobility of 0.1 $cm^2\,V^{-1}\,s^{-1}$, relatively close to that of CB free electrons in nc-TiO_2 films at 300 K (0.4 $cm^2\,V^{-1}\,s^{-1}$) [373]. The diffusion coefficient can be calculated from the Einstein–Nernst relation ($D = \mu k_B T/e$), which predicts that the transit time of free electrons from the center to surface of 10 nm nanoparticle is within 250 fs [373]. Although these values of charge carrier mobilities are different for the different methods, the same conclusion that was drawn that the trapping effect greatly limit the carrier mobilities in nc-TiO_2 networks because of the presence of gap states caused by the various causes that were summarized in the above sections.

6.3. Trapping limited recombination

Because charge carrier transport can be terminated by recombination, the recombination would be subject to modulation by trapping if the gap states are present in TiO_2 materials. For example, it was seen that the recombination between holes and electrons follows a power-law kinetic, an indicator to the limitation on electron multi-trapping migration. Many techniques, including transient absorption (TA), transient PL, transient EPR, and transient photoconductances can be used to study the recombination modulated by a trapping effect of gap states.

By means of a TA technique, an ultra-slow trapping-limited recombination between holes and electrons in nc-TiO_2 materials was studied by Hoffmann et al. [374]. They saw that the transient decays of free electron absorptions in nc-TiO_2 lasted for several hours in a non-exponential mode, as shown in Fig. 56. Such ultra-slow decays fitted well with an approximated saturation kinetic model that belongs to a two-step recombination mechanism involving necessary electron trapping at a gap state. The interme-

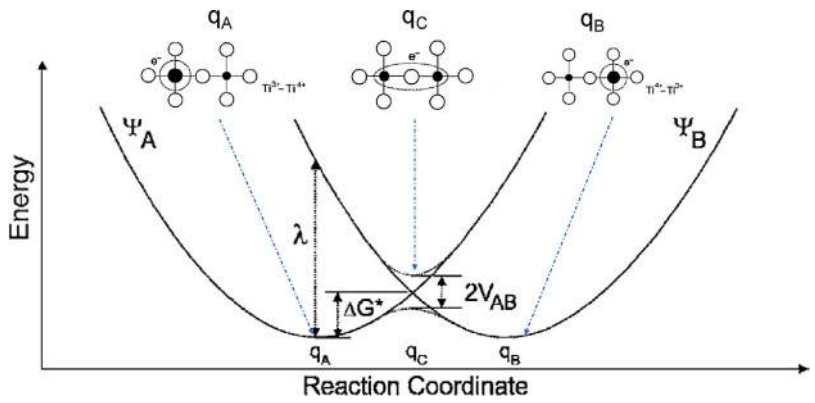

Fig. 55. Schematic diagram and potential energy surface of polaron e^- transfer. In the initial state ψ_A with structure q_A, the electron is localized on the left Ti ion, while in the final state ψ_B with structure q_B, the electron is localized on the right Ti ion. At the transition state ψ_C with structure q_C (a thermal transfer regime), the electron is shared between the two Ti ions.

Reproduced with permission from Ref. [367]. Copyright 2007 American Physical Society.

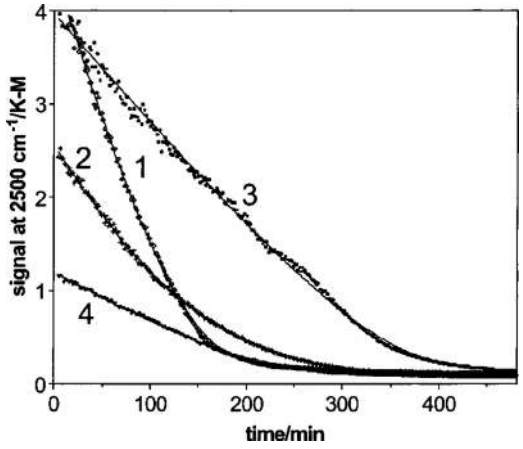

Fig. 56. Plot of DRIFTS signal (at 2500 cm^{-1}) versus time (data points) for four sequential UV treatment/relaxation sequences, along with fits according to the integrated saturation kinetic model (solid lines).

Reproduced with permission from Ref. [374]. Copyright 2002 American Chemical Society.

diate gap traps become saturated after trapping electrons and then recombination was slowed down to a lifetime of hours. In addition to this model, they also proposed a model involving an additional trapping step whose rate is dependent on surface hydration that plays a key role in gap states, which was also consistent with the experimental data. According to this model, the initial trapping confines the electron to an excited state in the trap (Eq. (23)), which subsequently relaxes to a hydration-related trap (Eq. (24)), and then recombine with a VB hole (Eq. (25)). It was considered by them that the hydration dependent rate is important in the ultra-slow recombination. The ultra-long life-time, on a timescale of hours, of charge carriers in photoexcited TiO_2 nanotubes arrays prepared from an anodization were also revealed by a time-resolved TRMC method, which is ascribed to the thermally-assisted re-emission of holes and the recombination processes involving carriers trapped in deep gap states located 1.0–1.2 eV above the VB edge [375].

$$e^-_{cb} + T^0 \overset{k_1, k_{-1}}{\longleftrightarrow} T^*_{e^-} \quad \text{(slow)} \tag{23}$$

$$T^*_{e^-} \overset{k'_2}{\rightarrow} T^{full}_{e^-} \quad \text{(hydration dependent rate)} \tag{24}$$

$$T^{full}_{e^-} + h^+_{vb} \overset{k_2}{\rightarrow} T^0 \quad \text{(fast)} \tag{25}$$

In addition to the ultra-slow recombination, the trapping effect on fast recombination was also seen by fs TA spectroscopy [376]. The TA changes at 1200 nm for an a-TiO_2 dense and a mesoporous a-TiO_2 films were monitored as a function of excitation intensities. An intensity-dependent component was seen after a fast geminate recombination, which also decelerates with an increase in light intensity. Such behavior is the characteristic of a bimolecular recombination between separated charges, in the form of a power law kinetic. The inversely-proportional dependence of the decay time on excitation density shows that the limitation of sub-ns recombination by multi-trapping effect. Different from the above study, this result revealed the importance of fast trapping via shallow traps in recombination. As the recombination kinetic is almost independent on specific surface areas, the shallow gap states contribute to the trap-limited recombination should locate on surfaces, rather than in the bulk.

The trapping effect on recombination was also observed at low temperatures. In recent research, Yates et al. used a steady state PL spectroscopy to study electron hopping transport in a compacted nc-TiO_2 under high-vacuum conditions at low temperatures [377]. Because TiO_2 is an intrinsically n-type material, the potential along the surface depletion layer can retard recombination by separating photoinduced holes and electrons in space. Accumulation of photoinduced positive charge on surfaces lowers the surface electrostatic potential and flattens the initially upward-bent bands, which then results in an increase of PL intensity. Upon the discontinuation of UV irradiation, some negative charges originally distributed in the TiO_2 network return to the surface of the outmost TiO_2 particles, which partially restores the upward band bending and reduces the PL intensity. Therefore, the rate of steady PL reduction was used to estimate a recombination via interparticle transport. The nc-TiO_2 sample exhibited a blue PL emission maximum at 530 nm. Fig. 57 shows that the PL intensity increases with UV light illumination time. After the irradiated surface was initially brought to a near-flat-band condition, the UV light was blocked for 120 min at different temperatures. The PL intensity undergoes an exponential decrease with increased rate constants as the temperature increases. The natural logarithm plot of the rate of interparticle charge migration for recombination with $1/T$ shows the thermal barrier of 150 meV. Therefore, the low temperature PL results revealed that the recombination in nc-TiO_2 materials are dominant via the CB extended states limited by shallow trapping. The low thermal barrier of mobility indicates that the polarons may be the gap states that play the role of trapping.

By means of a low temperature transient EPR, recombination via the migration modulated by small e-polaron hopping was revealed

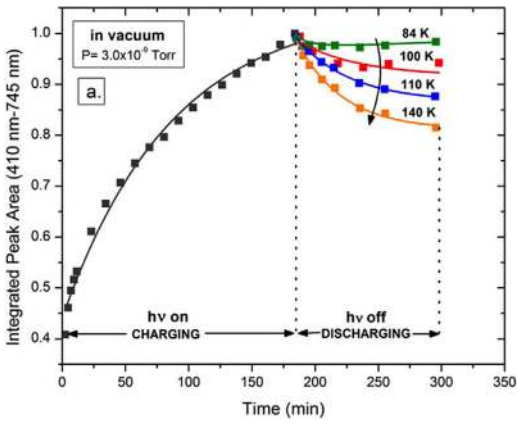

Fig. 57. Change in PL intensity during continuous UV excitation light illumination in vacuum at 140 K and the PL decay upon discontinuation of UV irradiation in the dark in vacuum at different temperatures. Black points represent the PL development upon UV irradiation. The TiO_2 surface was prepared to a near-flat band condition, as a saturation PL intensity plateau was almost achieved. Upon interruption of UV light, a PL decrease was observed at different temperatures: 84 K (green), 100 K (red), 110 K (blue), and 140 K (orange).

Reproduced with permission from Ref. [377]. Copyright 2013 American Chemical Society.

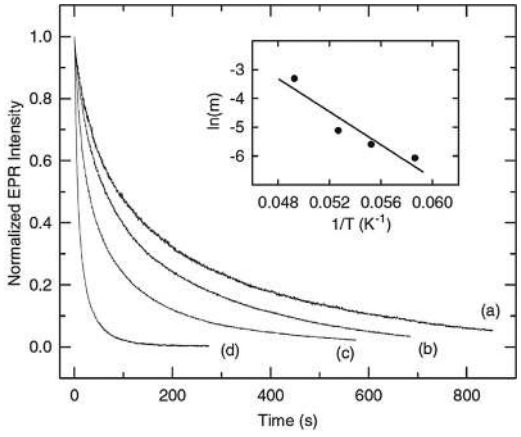

Fig. 58. Isothermal decays of the self-trapped-electron EPR Ti^{3+} signals at very low temperature. The magnetic field was held constant at the peak of the EPR signal and its decay was monitored as a function of time after removing the laser light. Temperatures for the individual decay curves were (a) 17.0, (b) 18.1, (c) 19.0, and (d) 20.3 K. The inset shows the plot of $\ln(m)$ versus $1/T$ used to obtain the activation energy.

Reproduced with permission from Ref. [246]. Copyright 2004 American Physical Society.

in other work [246]. After the excitation laser light was stopped, it was seen that the small e-polaron EPR signals rapidly decrease in intensity if the temperature is between 15 K and 20 K. Fig. 58 shows the decay curves taken at different specific temperatures. The recombination mechanism involving the hopping of e-polarons is described by a general order kinetic model.

$$\left(\frac{n(t)}{n_0}\right)^{1-b} = n_0\left[1 + s' n_0^{b-1}(b-1)\exp\left(-\frac{E}{k_B T}\right)t\right] \quad (26)$$

where b is a physical parameter to indicate recombination order. The decay of normalized EPR intensity was fitted by using this formula. The parameter b was adjusted until a straight line is obtained. The b was determined to about 1.38 for the four lines in Fig. 58, indicating a recombination kinetic between first order and second order. Each line has a different slope that is related to a thermal barrier (E) according to Eq. (24)

$$\ln(m) = \ln[s' n_0^{b-1}] - \frac{E}{k_B T} \quad (27)$$

The plot of $\ln(m)$ versus $1/T$ is shown as an inset in Fig. 58. The thermal barrier for small e-polaron transport to recombination is ~24 meV. It was shown that the primary physical mechanism by which self-trapped electrons decay occurs via the hopping of an electron from one Ti site to the other until it terminates at a trapped hole, or the direct thermal activation of the e-polarons to the CB state following a recombination with a trapped hole.

A recent study combined the EPR and the TA techniques to show the effects of trapping on recombination [378]. Fig. 59(A) shows that the self-localization of photoinduced electrons and holes at normal lattice sites of a nc-TiO_2 leads to e-polarons and h-polarons (O^- and Ti^{3+}). The EPR signals show very slow and monotonic growth over a timescale of seconds and minutes under simultaneous light illumination (Fig. 59(B)). Because the Ti^{3+} density never exceeds 10% of the O^- density, the majority of electrons remains in the CB states. After stopping light excitation for 20 min, Fig. 59(B) shows that the O^- and Ti^{3+} signals deplete to ~90% and 50% of their maximum value, respectively, and then remain constant over a timescale of hours. This result showed that the recombination of trapped electrons is governed by e-polaron diffusion to trapped holes among Ti^{3+} sites. Lowering the temperature increases the lifetime of trapped electrons in polaron states. When the temperature was increased to 140 K, no Ti^{3+} and less O^- signals were detected because of an increase of recombination by the reduction in trapping time. However, although there are almost no trapped electrons, the electrons residing in the CB extended states were still observed by an in situ IR absorption, indicating the separation of the free electrons with the holes after stopping the UV light illumination at this temperature. Further raising the temperature to 298 K significantly increases the IR absorption decay, and both Ti^{3+} and O^- species cannot be observed in this case. Therefore, the recombination of free electrons also accords with a thermally-activated mechanisms, indicate that the CB electrons are possibly trapped at some kinds of traps other than Ti^{3+} featured polarons to some extent, which can keep thermodynamic equilibrium with the CB states.

Yamada et al. used a more comprehensive method that combined a time resolved TA, a time-resolved PC, and a time-resolved PL spectroscopy to study room temperature photocarrier recombination in rutile and anatase single crystals oriented in the [100] direction [379]. The rutile PL, PC, and TA signals show the dependence of photocarrier density on the excitation density (I_{ex}). Fig. 60(A) shows that the PL decay is determined by geminate recombination, featuring a mono-exponential form with a lifetime of 18 ns. The PC decay also has a mono-exponential form with a lifetime of 24 ns. Because the PC decay is mainly attributed to relaxation (trapping) of mobile electrons, the relaxation time of electrons is ~24 ns. The decay of TA contributed by photoinduced trapped holes also shows a single exponential function with a lifetime of 48 ns. It is seen that the PL decay rate is the sum of the decay rates of electrons and holes, so the recombination arises from electron transport to immobilized holes. This result also indicates that the recombination in rutile single crystal is not limited by trapping effect at room temperature due to the geminate mono-exponential recombination.

Fig. 60(B) shows that the anatase PL and TA decays of anatase present by a non-exponential mode. The complete coincidence between the PL and the TA decays indicated the determination of recombination is due to the hole lifetime (~2.3 ns). The non-exponential decay profiles mean that the recombination cannot be described by a two-carrier geminate radiative mechanism, but is governed by a single-carrier non-radiative decay kinetic. The decay

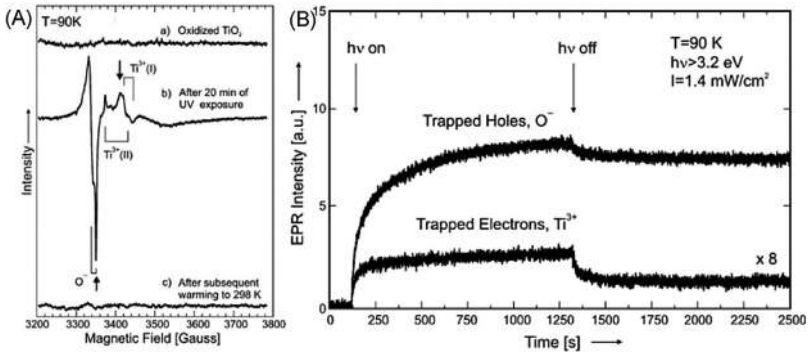

Fig. 59. (A) EPR spectra of oxidized anatase nanoparticles (a) before and (b) after 20 min of UV exposure at 90 K ($I = 1.4\,mW\,cm^{-2}$ with $h\nu > 3.2$ eV). Subsequent warming (c) to 298 K leads to the complete annihilation of paramagnetic charge carriers. Concentration of O- and Ti^{3+} centers as a function of UV exposure time ($I = 1.4\,mW\,cm^{-2}$ with $h\nu > 3.2$ eV).

Reproduced with permission from Ref. [378]. Copyright 2005 American Chemical Society.

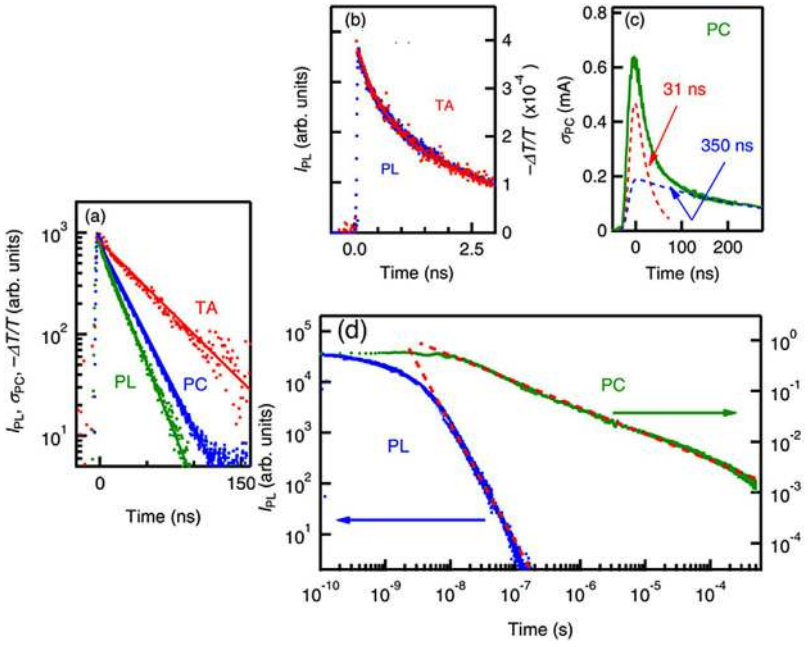

Fig. 60. (A) PL, PC, and TA decay profiles of rutile single crystal. Solid lines are curves fitted by a single exponential function. (B) PL and TA decay dynamics of anatase single crystal in the nanosecond time window. (C) PC decay dynamics of anatase in the nanosecond time region. (D) PL and PC decay dynamics of anatase in a log–log plot.

Reproduced with permission from Ref. [379]. Copyright 2012 AIP Publishing.

behavior also exhibits the nonexponential mode with a lifetime much longer for the PC than the PL and the TA (Fig. 60(C)), which shows the much longer lifetime of electrons than holes in anatase. Fig. 60(D) shows that the PL decays obey a power-law kinetic scaling after 50 ns, and that of PC also follows a power-law mode with a lifetime (us) much longer than the PL lifetime. Therefore, the charge carrier kinetics in an anatase single-crystal are different from rutile. The power-law decay kinetics on a μs timescale shows that the electron recombination is limited by the multiple-trapping-dominated transport involving shallow tail states. Long lifetime of electrons in anatase also leads to electron diffusion lengths of electrons that are much longer in anatase (>10 μm) than rutile (~100 nm), so anatase TiO_2 usually is observed to be more active as compared to rutile. Similar results were also obtained in another TA studies of fresh and reduced r-(110) and a-(101) single crystals that the recombination in rutile is faster than in anatase due to their higher density of bulk gap states [380].

The effect of multi-trapping transport on recombination can be modulated by manipulating a gap state pre-occupation. It was reported that applying a negative bias voltage (potential) to a $Ru(dcbpy)_3$ sensitized nc-TiO_2 electrodes resulted in the reduction in the time constant for electron recombination from ~1 μs to 1 ms, because pre-populating the gap states increases electron transport to immobilized holes for recombination as increased by limiting the trapping effect [381]. Fig. 61 shows the TA decay profiles determined as a function of the bias potentials applied to an nc-TiO_2 electrode. The observed median time (t50%: the time at which the TA decayed to half of its initial value) was used for estimating the recombination lifetime. The linear plot of ln(t50%) vs applied potentials shows a quantitative dependence of t50% upon applied potentials the same as the density of CB electrons, so the recombination of electrons takes place in a trapping-limited geminate mechanism associated with their accumulation at gap states.

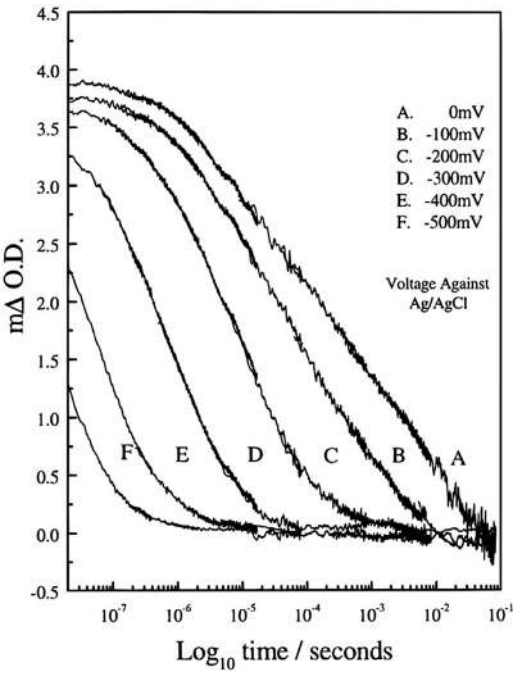

Fig. 61. TA data following the decay of the cation state of $Ru(dcbpy)_2(NCS)_2$ adsorbed on a nc-TiO_2 electrode as a function of applied potential. Cation decay is attributed to charge recombination with electrons in trap/conduction band states of the TiO_2. Data were collected at a probe wavelength of 820 nm in a three electrode photoelectrochemical cell at room temperature, employing 560-nm excitation pulses. The electrolyte was maintained at a constant potential by an Ag/AgCl reference electrode (+40 mV versus SCE). Voltages are quoted versus the reference electrode.

Reproduced with permission from Ref. [381]. Copyright 2004 American Chemical Society.

6.4. *Trapping affected interfacial transfer*

The interfacial transfer is significantly dependent on the trapping effect of gap states because it also terminates charge carrier transport within TiO_2 materials. For example, the spectroscopic study showed the difference between electron interfacial transfer in a-TiO_2 and r-TiO_2 because of their difference in gap states [380]. It was also seen that the pre-population of electrons at gap states increases the interfacial transfer speed by increasing transport, accordingly resulting in an increase of water photoelectrochemical oxidations on TiO_2; the photoinduced H_2 generation by reducing water was seen to be thermally-activated due to the limitation of electron interfacial transfer by trapping effect of gap states [382,383].

The electrons can transfer to O_2 via both the free CB states and the surface gap states. The comparison between those two transfer modes was studied with a TA study [317]. Fig. 62 shows the TA spectrum of a nc-TiO_2 film with a delay time of 100 ns after excitation under a N_2 saturation and an air saturation by using CD_3OD as hole capturers. The introduction of air leads to a decrease in the absorption at 700 nm and has no effect on the featureless absorption from 1500 to 2000 nm, indicating a clear decrease of trapped electrons and no change of free electrons in a nc-TiO_2 film. This result shows a rapid reaction of trapped electrons with O_2 because of the dominant location of shallowly trapped electrons on the particle surface. The long lifetime (100 ms) indicates a slower reaction of free electrons with O_2 than the trapped ones. Therefore, this observation suggests that the free electrons in bulk are firstly trapped at a surface trap sites before their reaction with O_2. The result is consistent with a general recognition that the gap states at surfaces act as a "gate" for the interfacial transfer of charge carriers [384,385]. The

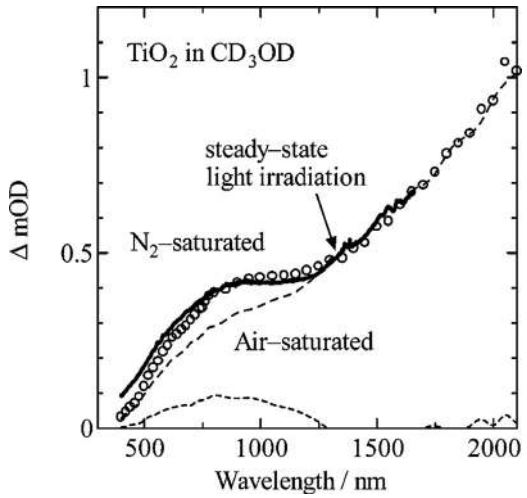

Fig. 62. Transient absorption spectra of a TiO_2 film in N_2-saturated CD_3OD (O) and air-saturated CD_3OD (– – –). The dotted line (···) represents the subtraction spectrum.

Reproduced with permission from Ref. [317]. Copyright 2004 American Chemical Society.

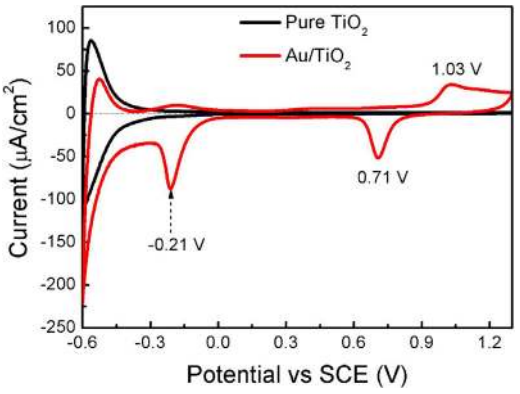

Fig. 63. CV behaviors of pure TiO_2 nanorod arrays and Au/TiO_2 nanorod arrays. Reproduced with permission from Ref. [287]. Copyright 2019 Elsevier.

role of surface gap states of nc-TiO_2 materials in accelerating the interfacial transfer of electrons to an electrolyte was also revealed by a combined theoretical and electrochemical study [386]. If the electron transfer mediating by surface gap states is faster than that by the CB extended states, the electrons trapped at surface cannot equilibrate with that in bulk states. This results in a different steady-state distribution of electrons at surface gap states, characterized with a Fermi level lower than the bulk one in energy. The resulting Fermi level gradient from bulk to surfaces drives electron transport to participate in interfacial transfer.

In some research, the chemical entities of surface gap states were proposed to facilitate electron self-localization at surface Ti sites that have chemical coordination different from bulk ones. For the TiO_2 nanosheets decorated with CdSe quantum dots, under a solar light illumination, the photogenerated electrons in CdSe can transfer to TiO_2 and result in surface Ti^{3+} states. This deep gap state induced by an electron localization drives the transfer of electrons to attend surface chemical reactions. The Ti^{3+} state coupling their oxidized states (Ti^{4+}) was proposed to form a redox shuttle to increase photocatalytic hydrogen generation on TiO_2 surfaces [387]. Our recent electrochemical study also revealed that the Au-induced oxygen defects can form an effective pathway accelerating electron interfacial transfer from a TiO_2 nanorod array to the O_2 in an electrolyte [287]. Fig. 63 shows the electrochemical CVs of pure

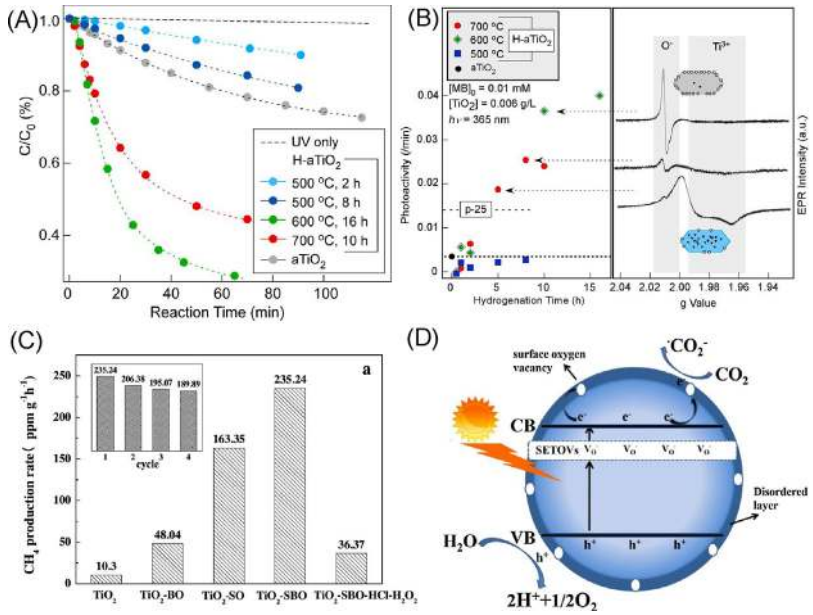

Fig. 64. (A) Photodegradation of methylene blue (MB) under UV irradiation is compared. Under the hydrogenation condition employed. The H-aTiO_2 (Hydrogen reduced a-TiO_2) nanocrystals are found to have either higher or lower photoactivity compared with aTiO_2. (B) Photoactivities (k, min^{-1}) and EPR spectra of H-a-TiO_2 are shown together against hydrogenation time and temperatures. Reproduced with permission from Ref. [402]. Copyright 2019 American Chemical Society. (C) Photocatalytic activity of CH_4 production rate on different TiO_2 under UV light illumination; (D) schematic diagram of CO_2 photoreduction mechanism on TiO_2-SBO (SBO means the Vo trappe an electron). Reproduced with permission from Ref. [406]. Copyright 2017 Elsevier.

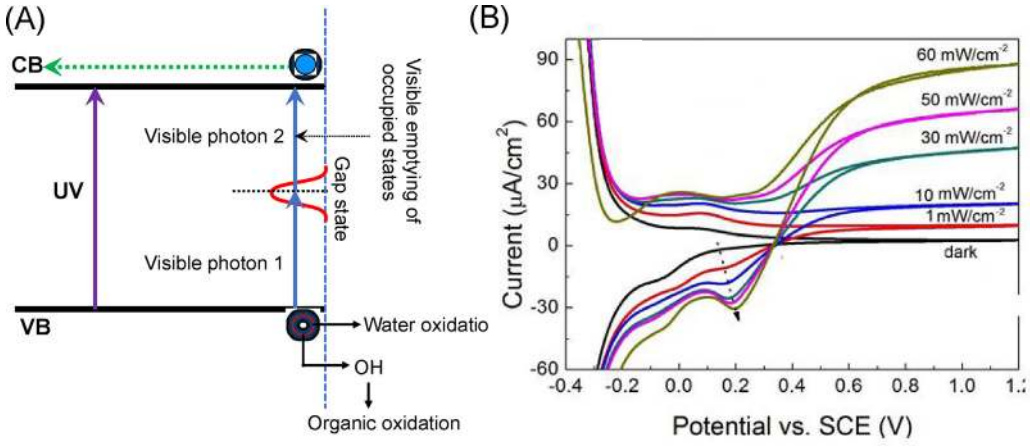

Fig. 65. (A) Schematic diagram for double-photon absorption via a really-existed gap states and the induced photocatalytic effect; (B) CV behaviors of TiO_2 nanorod arrays under illumination 550 nm monochromatic light with different intensities.
Reproduced with permission from Ref. [406]. Copyright 2019 Elsevier.

TiO_2 and Au/TiO_2 nanorod arrays in 0.1 M Na_2SO_4 under a saturated N_2 atmosphere. The cathodic current peak at −0.2 V vs. SCE was ascribed to electron transfer to O_2 via surface oxygen defects created by Au surface decorations, which shows a great increase due to an additional electron interfacial transfer via Au-induced oxygen defects locating at Au/TiO_2 perimeter sites.

By means of an infrared TA spectroscopical technique, the interfacial transfer of trapped holes from a nc-TiO_2 electrode to water electrolyte was studied by monitoring a change of the "finger" absorption for trapped holes [388]. The similarity between the TAs of nc-TiO_2 films in water and in air indicated that the photocatalytic oxidation of water by trapped holes is very slow. When alcohols were present, the appearance of fast decay of TAs just after light excitation shows an immediate reaction of trapped holes with alcohols. The lifetimes of trapped holes in methanol, ethanol, and 2-propanol were determined to be 300, 1000, and 3000 ps, respectively. Because the decay kinetics of trapped holes is mono-exponential on a ns timescale, the capture of trapped holes by alcohols is not limited by a trapping process, but the transfer from a trapping site to the alcohols.

These studies indicated that interfacial transfer of holes for water photocatalytic oxidations needs much longer time, so an inhibition of recombination is necessary so as to create long-lived holes. Lowering recombination by reducing electron transport with a pre-population of gap states is the main method to elongate hole lifetime [389]. It was seen that the TA decay for trapped holes consists of a fast power-law component (1–100 μs) and a stretched exponential one (~30 ms). The fast power-law decay is ascribed to a recombination limited by electron multi-trapping transport, and the stretched exponential decay is assigned to the long lived holes trapped at gap states. The density of long-lived holes can be increased by an increase of applied potentials due to the removal of photoelectrons via an external circuit. Therefore, the slow stretched exponential kinetic is eventually attributed to the

reaction of trapped holes with water. The formation of long-lived holes is prerequisite for a water splitting and it has been recently reported that a hole lifetime of ~0.3 s was required for water oxidation to occur in near neural solution (pH = 6.5). A much faster oxidation occurs with a lifetime of ~30 ms was observed when the pH value was increased to 12.7 due to the function of protons [389].

The interfacial transfer of charge carriers directly determines the photocatalytic efficiency of TiO_2 materials. Because the trapping effect of gap states plays a great role in interfacial transfer, they are also accordingly important for TiO_2 photocatalysis. The higher photocatalytic activity of anatase is usually related to its higher CB edge position. However, recent research showed that the difference in the depths of gap states (trpas) may be a main reason [316]. The traps of electrons are shallower than 0.1 eV in a-TiO_2, so the trapped electrons are under thermal equilibrium with the free electrons over long lifetime (1 ms). However, the deep traps (~0.9 eV) leads to a fast trapping of most of free electrons at gap states within a few ps in r-TiO_2. Only a trace amount of free or shallowly trapped electrons can survive on a ms timescale. The difference in the free electrons leads to the higher photocatalytic reduction activity for anatase over rutile. However, a clear difference was observed in the lifetime of holes in photocatalytic oxidations, which was much longer in rutile than anatase. Longer lifetime of holes is important for the water oxidation, so r-TiO_2 usually shows a higher activity than a-TiO_2 for water photocatalytic oxidation [390].

Furthermore, the trapping effect of gap states on interfacial transfer was also revealed for b-TiO_2 by a TA study [316]. It was seen that the lifetimes of trapped electrons and trapped holes are longer for b-TiO_2 than r-TiO_2 and a-TiO_2, respectively. Although most of the free electrons in b-TiO_2 are trapped at gap states, the b-TiO_2 still showed an activity comparable with a-TiO_2. Under the consideration that the steady photocatalysis proceeds by combining both electron reduction and hole oxidation, the plausible reason for this distinctive activity of b-TiO_2 is the larger number of surviving holes than a-TiO_2. It was revealed that r-TiO_2 has the holes with a longer lifetime, but the electron traps (~0.9 eV) is deeper than b-TiO_2 (~0.4 eV) and a-TiO_2 (<0.1 eV). Therefore, the results indicate that the moderate depth of electron traps allows for reasonable reactivities of both trapped electrons and holes in b-TiO_2, which accordingly results in high activity contrary to that expected from the shorter-lifetime of free electrons.

Ti^{3+} self-doped TiO_2 materials have drawn much attention in recent years. It is thought that Ti^{3+} gap states mainly act as the recombination centers to quench holes due to their deep location in the band gap. However, a recent research reported the role of Ti^{3+}-derived gap states in increasing photocatalytic activity by mediating electron interfacial transfer. Amano et al. combined an EPR, a sheet resistance, and a photoelectrochemical analysis to investigate the effect of Ti^{3+} gap states on photocatalytic water reduction [391]. They saw that the low photocatalytic activity of hydrogen generation of an air-annealed r-TiO_2 is greatly increased to be better than a commercial TiO_2 by a reduction at 700 °C. Re-oxidation of the reduced sample at 500 °C decreased its photocatalytic activity to its original low value. This result showed the function of Ti^{3+} gap states for an increase in photocatalytic activity are due to the increase in donor density and electrical conductivity. High density of electrons at the shallow traps and the CB states are the most important factor to increase electron interfacial transfer for water photocatalytic reduction. In a recent research by us, Ti^{3+} self-dopants were implanted in r-TiO_2 lattice by a direct ice-quenching method [392]. We saw an increase of photocatalytic water reduction and methylene blue degradation due to the promotion of electron interfacial transfer by Ti^{3+} gap states. Under super bandgap illumination, an increase of photocurrents for r-TiO_2 nanorod array by introducing Ti^{3+}-derived gap states was also observed because the increase of donor density increases the charge transport for interfacial transfer [393].

It is a reasonable assumption that surface gap states play a dual role in interfacial transfer and recombination, hence their effect was studied by one of our phenomenological models [394]. We showed that, rather than interfacial transfer, the recombination via surface gap states is increased by an increase of surface trapping speed when the interfacial transfer kinetics is unaffected. However, increasing surface trap density can increase interfacial transfer speed, and consequently leads to an increase of photocatalytic activity. The balance between the roles of trapping and interfacial transfer that the surface gap states play leads to a first increase-then-decrease of photocatalytic activity with an increase of trap density. Majima et al. used a fs time-resolved diffusion reflectance and a single-particle photoluminescence to study the effect of oxygen defects on photocatalytic hydrogen generation under solar light illumination [395]. It was seen that the shallowly trapped electrons are in thermal equilibrium with the free electrons in the case of low surface defect density. When high density of oxygen defects was introduced, most of electrons becomes deeply trapped, which prevent them from participating in photocatalytic reactions. Therefore, an appropriate amount of oxygen defects, which act as gap states, are beneficial for increasing photocatalytic activity due to their role in accelerating the interfacial transfer of electrons for water reduction.

Oxygen activation by photoinduced electrons are important in photocatalytic organic oxidations. The electron transfer to O_2 mediated by gap states is a main pathway, which was studied by means of electron energy loss spectroscopy (EELS) in a recent study [396]. It was seen that the absorption of O_2 results in a new loss at 2.8 eV in the energy loss spectrum, also accompanied with a decrease of Ti^{3+} d-d transition at ~0.9 eV. The species responsive for the 2.8 eV energy loss peak is considered to be surface peroxo (O_2^{2-}, an active ROS) adsorbed at regular 5-f Ti^{4+} sites, caused by electron interfacial transfer to O_2. This research suggested that the importance of self-localization of electrons at Ti sites (e-polaron) is important in O_2 activation. A recent DFT calculation further revealed that the formation of O_2^{2-} species by electron interfacial transfer from Ti sites to adsorbed O_2 is characterized with an apparent activation energy [397], which is also supported by our recent steady photoconductance experimental result and the TA results of Durrant et al. [342,398]. Moreover, the importance of bulk Ti^{3+} cations was also indicated. By means of a temperature-programmed desorption spectroscopy and a scanning tunneling microscopy (STM), it was reported that the bulk Ti(i)-induced Ti^{3+} sites can provide electrons for O_2 chemical adsorption and result in surface activated O_2 species. Because the Ti^{3+} species are almost independent of chemical entities, it is thought that the attraction of photoinduced electrons localized at bulk Ti sites to the oxygen facilitates the electron transport from the bulk to surfaces [399].

Not merely limited on surfaces, it was reported that the surface defects and the bulk defects can couple together to accelerate electron interfacial transfer to O_2 and then increase photocatalytic activity. It was shown that the photocatalytic oxidation of benzene, methanol, a-phenethyl alcohol and the photocatalytic reduction of CO_2 by light-illuminated TiO_2 materials can be increased by increasing the ratio of surface V_Os to the bulk V_Os [400–403]. In a research performed by Yu et al., a traditional hydrogen reduction method was used to reduce a-TiO_2 [402]. The EPR spectra were measured to show the spatial distribution of surface defect (O^-) and bulk defect (Ti^{3+}), which was then related to the photocatalytic activity for methylene blue degradation. Fig. 64(A) shows that the photocatalytic activity increases with an increase of surface-to-bulk defect ratio under UV light illumination, probably due to a decrease of recombination via bulk defects and an increase of interfacial transfer via surface defects (Fig. 64(B)). Under a solar

light illumination, Yang et al. suggested another synergistic effect for the bulk and surface defects in increasing the photocatalytic activity [401], as shown in Fig. 64(C), which proposed that the bulk V_os formed a middle band for using both the UV and the visible lights (Fig. 64(D)). The surface V_os sites can increase light absorption, together coupling with an acceleration of electron interfacial transfer to O_2.

6.5. Role of intermediate gap states in a double-photon absorption

In addition to the mediation of charge carrier kinetics by a trapping effect, another important effect of gap states is their intermediate role in realizing a double-photon absorption of visible light. Fig. 65(A) shows that the occupied gap states can be switched from a full state to an empty state by absorbing a visible photon. If the emptied gap states have a lifetime that is long enough, they would allow a further transition of an electron from the VB states to them; this can eventually result in an electron in the CB states and the hole in the VB states. From this viewpoint, it is known that the photoelectrochemical or the photocatalytic behavior led by this double-photon absorption are the same as a super bandgap transition. In the literature, such visible response of TiO_2 materials were called a sub-bandgap response [404,405], which was found several decades ago on r-TiO_2 single-crystals and compact r-TiO_2 films. The sub-bandgap response is usually neglected as compared to the super-bandgap response because of low efficiency. In a recent study by one of us, it was interesting to see that the TiO_2 nanorod array presented a very high sub-bandgap response. Fig. 65(B) shows the CV plots of impurity-free TiO_2 nanorod arrays under an illumination of 550 nm light with different intensities. It was clearly revealed that emptying the occupied gap states (~0.2 V vs SCE) is accompanied with photocurrent generation. Importantly, the photocurrent can reach one sixth of a UV-induced one under UV illumination with the same photon flux. It was also seen that the double-photon absorption can result in a photocatalytic degradation of methyl orange aqueous solution and an generation of hydroxyl free radicals ((OH). Therefore, the role of gap states in mediating photon absorption mode may be important in designing visible light responsive TiO_2 photocatalysis [406].

7. Summary and remarks

This review has dealt with the chemical entities, physiochemical nature of the intrinsic intermediate gap states in TiO_2 materials, and their role in charge carrier kinetics from bottom level to top level. A schematic summary is shown in Fig. 66. We carefully elaborated the spatial distribution, mobilities, and formation mechanisms of some of the main chemical entities that cause the gap states of TiO_2, including the V_os, OHs, and Ti(i)s. It is illustrated that the V_Os distribution on the surfaces is different from surface to surface and from polymorph to polymorph, and the Ti(i)s can also locate both in bulk and on surfaces of the TiO_2 materials. We summarized the physiochemical nature of gap states that are formed by charge carrier localizations at normal lattice and defect sites that were widely studied both experimentally and theoretically. It is comprehensively elaborated that polarons are the main contribution to gap state formation. If e-polarons and h-polarons are within the Coulombic attraction distance, an exciton can also be formed and contribute to the gap states. We gave a general description to the energy distribution of gap states, and defined the continuous band-tailed gap states and the monoenergetic gap states in a rigorous way. The shallow gap states and the deep ones are distinguished from a kinetic viewpoint considering thermal release. Furthermore, the thermodynamic population of charge carriers,

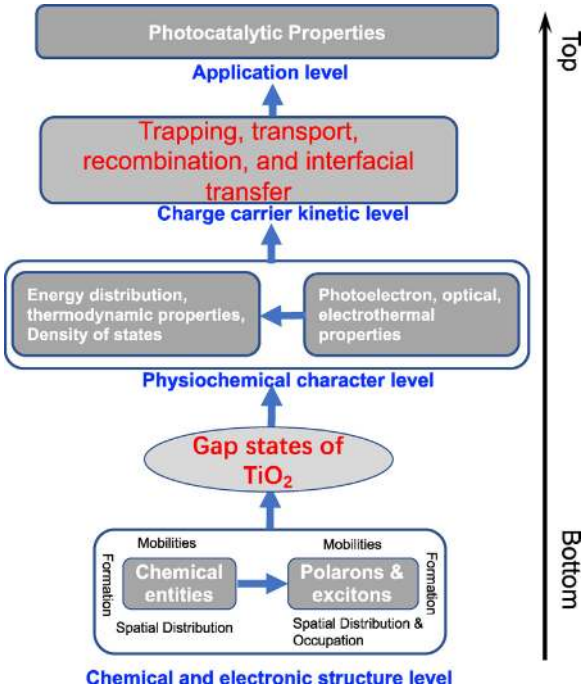

Fig. 66. A bottom-to-top level schematic illustration of the gap states of TiO_2 materials, charge carrier kinetics, and associated applications.

their energy distribution, and thermodynamic properties are also discussed. Photoelectron emission spectroscopy, electrochemical techniques, transient optical absorption, and steady state photoluminescence that were used to study TiO_2 gap states are summarized from viewpoints of energy distribution and density of states. The association of them with chemical entities and charge carrier localization were also illustrated. Lastly, the trapping effect of gap states on charge carrier kinetics in TiO_2 materials, including the transport, the recombination, and the interfacial transfer, were also carefully summarized and discussed. We also elaborated the relationship between photocatalytic properties of TiO_2 materials with the charge carrier interfacial transfer modulated by gap states. Because engineering gap states is the main strategy to modulate the charge carrier kinetics that drive the photocatalytic process of TiO_2 materials, it is expected that the results summarized in the present review provide good assistance and guidance to make TiO_2 photocatalytic materials, this approach is also applicable to other semiconductor photocatalytic materials.

Acknowledgment

This work was supported by the Foundation of China (51772230, 51461135004), Hubei Foreign Science and Technology Cooperation Project (2017AHB059), and the Japan Society for the Promotion of Science (JSPS) for an Invitation Fellowship for Foreign Researchers (L16531). I.P. Parkin thanks the Wuhan University of Technology for a Visiting Professorship.

References

[1] A. Fujishima, K. Honda, Electrochemical photolysis of water at a semiconductor electrode, Nature 238 (1972) 37–38.
[2] D.M. Schultz, T.P. Yoon, Solar synthesis: prospects in visible light photocatalysis, Science 343 (2014), 1239176-1–8.
[3] A. Meng, J. Zhang, D. Xu, B. Cheng, J. Yu, Enhanced photocatalytic H2-production activity of anatase TiO_2 nanosheet by selectively depositing dual-cocatalysts on {101} and {001} facets, Appl. Catal. B: Environ. 198 (2016) 286–294.

[4] S. Banerjee, D.D. Dionysiou, S.C. Pillai, Self-cleaning applications of TiO_2 by photo-induced hydrophilicity and photocatalysis, Appl. Catal. B: Environ. 176–177 (2015) 396–428.
[5] J. Zhang, P. Zhou, J. Liu, J. Yu, New understanding of the difference of photocatalytic activity among anatase, rutile and brookite TiO_2, Phys. Chem. Chem. Phys. 16 (2014) 20382–20386.
[6] A.L. Linsebigler, G. Lu, J.T. Yates, Photocatalysis on TiO_2 surfaces: principles, mechanisms, and selected results, Chem. Rev. 95 (1995) 735–758.
[7] A. Fujishima, X. Zhang, D.A. Tryk, TiO_2 photocatalysis and related surface phenomena, Surf. Sci. Rep. 63 (2008) 515–582.
[8] K. Qi, B. Cheng, J. Yu, W. Ho, A review on TiO_2-based Z-scheme photocatalysts, Chin. J. Catal. 38 (2017) 1936–1955.
[9] J. Schneider, M. Matsuoka, M. Takeuchi, J. Zhang, Y. Horiuchi, M. Anpo, D.W. Bahnemann, Understanding TiO_2 photocatalysis: mechanisms and materials, Chem. Rev. 114 (2014) 9919–9986.
[10] X. Lang, X. Chen, J. Zhao, Heterogeneous visible light photocatalysis for selective organic transformations, Chem. Soc. Rev. 43 (2014) 473–486.
[11] W. Wang, M.O. Tadé, Z. Shao, Research progress of perovskite materials in photocatalysis and photovoltaics-related energy conversion and environmental treatment, Chem. Soc. Rev. 44 (2015) 5371–5408.
[12] D. Xu, Y. Hai, X. Zhang, S. Zhang, R. He, Bi_2O_3 cocatalyst improving photocatalytic hydrogen evolution performance of TiO_2, Appl. Surf. Sci. 400 (2017) 530–536.
[13] Y.K. Mishra, G. Modi, V. Cretu, V. Postica, O. Lupan, T. Reime, I. Paulowicz, V. Hrkac, W. Benecke, L. Kienle, R. Adelung, Direct growth of freestanding ZnO tetrapod networks for multifunctional applications in photocatalysis, UV photodetection, and gas sensing, ACS Appl. Mater. Interfaces 7 (2015) 14303–14316.
[14] D. Xu, L. Li, R. He, L. Qi, L. Zhang, B. Cheng, Noble metal-free RGO/TiO_2 composite nanofiber with enhanced photocatalytic H2-production performance, Appl. Surf. Sci. 434 (2018) 620–625.
[15] H. Li, Y. Liu, Xing Gao, C. Fu, X. Wang, Facile synthesis and enhanced visible-light photocatalysis of graphitic carbon nitride composite semiconductors, ChemSusChem 8 (2015) 1189–1196.
[16] X. Chen, A. Selloni, Introduction: titanium dioxide (TiO_2) nanomaterials, Chem. Rev. 114 (2014) 9281–9282.
[17] A. Meng, B. Zhu, B. Zhong, L. Zhang, B. Cheng, Direct Z-scheme TiO_2/CdS hierarchical photocatalyst for enhanced photocatalytic H2-production activity, Appl. Surf. Sci. 422 (2017) 518–527.
[18] B. Yoon, D. Yadav, R. Raj, E. Sortino, S. Ghose, P. Sarin, D. Shoemaker, Measurement of O and Ti atom displacements in TiO_2 during flash sintering experiments, J. Am. Ceram. Soc. 101 (2018) 1811–1817.
[19] S. Wang, L. Pan, J.-J. Song, W. Mi, J.-J. Zou, L. Wang, X. Zhang, Titanium-defected undoped anatase TiO_2 with p-type conductivity, room-temperature ferromagnetism, and remarkable photocatalytic performance, J. Am. Chem. Soc. 137 (2015) 2975–2983.
[20] M.J. Powell, R. Quesada-Cabrera, A. Taylor, D. Teixeira, I. Papakonstantinou, R.G. Palgrave, G. Sankar, I.P. Parkin, Intelligent multifunctional VO_2/SiO_2/TiO_2 coatings for self-cleaning, energy-saving window panels, Chem. Mater. 28 (2016) 1369–1376.
[21] F. Chen, W. Luo, Y. Mo, H. Yu, B. Cheng, In situ photodeposition of amorphous CoSx on the TiO_2 towards hydrogen evolution, Appl. Surf. Sci. 430 (2018) 448–456.
[22] J. Fei, J. Li, Controlled preparation of porous TiO_2–Ag nanostructures through supramolecular assembly for plasmon-enhanced photocatalysis, Adv. Mater. 27 (2015) 314–319.
[23] J. Low, L. Zhang, B. Zhu, Z. Liu, J. Yu, TiO_2 photonic crystals with localized surface photothermal effect and enhanced photocatalytic CO_2 reduction activity, ACS Sustain. Chem. Eng. 6 (2018) 15653–15661.
[24] L. Ma, G. Wang, C. Jiang, H. Bao, Q. Xu, Synthesis of core-shell TiO_2@g-C3N4 hollow microspheres for efficient photocatalytic degradation of rhodamine B under visible light, Appl. Surf. Sci. 430 (2018) 263–272.
[25] Y. Lai, J. Huang, Z. Cui, M. Ge, K. Zhang, Z. Chen, L. Chi, Recent advances in TiO_2-based nanostructured surfaces with controllable wettability and adhesion, Small 12 (2016) 2203–2224.
[26] L. Gao, Y. Li, J. Ren, S. Wang, R. Wang, G. Fu, Y. Hu, Passivation of defect states in anatase TiO_2 hollow spheres with Mg doping: realizing efficient photocatalytic overall water splitting, Appl. Catal. B: Environ. 202 (2017) 127–133.
[27] S.A. Ansari, M.M. Khan, M.O. Ansari, M.H. Cho, Silver nanoparticles and defect-induced visible light photocatalytic and photoelectrochemical performance of Ag@m-TiO_2 nanocomposite, Sol. Energy Mater. Sol. Cells 141 (2015) 162–170.
[28] P. Wang, Y. Lu, X. Wang, H. Yu, Co-modification of amorphous-Ti(IV) hole cocatalyst and $Ni(OH)_2$ electron cocatalyst for enhanced photocatalytic H_2-production performance of TiO_2, Appl. Surf. Sci. 391 (2017) 259–266.
[29] P. Wang, X. Yi, Y. Lu, H. Yu, J. Yu, In-situ synthesis of amorphous H_2TiO_3-modified TiO_2 and its improved photocatalytic H_2-evolution performance, J. Colloid Interface Sci. 532 (2018) 272–279.
[30] E.M. Samsudin, S.B. Abd Hamid, J.C. Juan, W.J. Basirun, A.E. Kandjani, Surface modification of mixed-phase hydrogenated TiO_2 and corresponding photocatalytic response, Appl. Surf. Sci. 359 (2015) 883–896.
[31] X. Li, J. Yu, M. Jaroniec, Hierarchical photocatalysts, Chem. Soc. Rev. 45 (2016) 2603–2636.
[32] K. Osako, K. Matsuzaki, T. Susaki, S. Ueda, G. Yin, A. Yamaguchi, H. Hosono, M. Miyauchi, Direct observation of interfacial charge transfer between rutile TiO_2 and ultrathin CuO_x film by visible-light illumination and its application for efficient photocatalysis, ChemCatChem 10 (2018) 4545–4554.
[33] R. Godin, Y. Wang, M.A. Zwijnenburg, J. Tang, J.R. Durrant, Time-resolved spectroscopic investigation of charge trapping in carbon nitrides photocatalysts for hydrogen generation, J. Am. Chem. Soc. 139 (2017) 5216–5224.
[34] B. Ohtani, Revisiting the fundamental physical chemistry in heterogeneous photocatalysis: its thermodynamics and kinetics, Phys. Chem. Chem. Phys. 16 (2014) 1788–1797.
[35] P. Zhang, T. Wang, X. Chang, J. Gong, Effective charge carrier utilization in photocatalytic conversions, Acc. Chem. Res. 49 (2016) 911–921.
[36] B. Liu, Monte-Carlo modelling of nano-material photocatalysis: bridging photocatalytic activity and microscopic charge kinetics, Phys. Chem. Chem. Phys. 18 (2016) 11520–11527.
[37] J. Low, B. Dai, T. Tong, C. Jiang, J. Yu, In situ irradiated X-Ray photoelectron spectroscopy investigation on direct Z-scheme TiO_2/CdS composite film photocatalyst, Adv. Mater. 30 (2018) 1802981.
[38] H. Gerischer, A. Heller, The role of oxygen in photooxidation of organic molecules on semiconductor particles, J. Phys. Chem. 95 (1991) 5261–5267.
[39] B. Liu, X. Zhao, A. Fujishim, K. Nakata, Thermodynamic and kinetic analysis of heterogeneous photocatalysis for semiconductor systems, Phys. Chem. Chem. Phys. 16 (2014) 8751–8760.
[40] B. Liu, X. Zhao, Kinetic study of the heterogeneous photocatalysis of porous nanocrystalline TiO_2 assemblies using a continuous random walk simulation, Phys. Chem. Chem. Phys. 16 (2014) 22343–22351.
[41] A.L. Luna, D. Dragoe, K. Wang, P. Beaunie, E. Kowalska, B. Ohtani, D.B. Uribe, M.A. Valenzuela, H. Remita, C. Colbeau-Justin, Photocatalytic hydrogen evolution using Ni–Pd/TiO_2: correlation of light absorption, charge-carrier dynamics, and quantum efficiency, J. Phys. Chem. C 121 (2017) 14302–14311.
[42] N.S. Allen, N. Mahdjoub, V. Vishnyakov, P.J. Kelly, R.J. Kriek, The effect of crystalline phase (anatase, brookite and rutile) and size on the photocatalytic activity of calcined polymorphic titanium dioxide (TiO_2), Polym. Degrad. Stab. 150 (2018) 31–36.
[43] J. Schneider, D. Bahnemann, Strong transient absorption of trapped holes in anatase and rutile TiO_2 at high laser intensities, J. Phys. Chem. C 122 (2018) 13979–13985.
[44] B. Liu, R. Zhang, Effects of spatial topologies and electron Fermi-level gradient on the photocatalytic efficiency of nano-particulate semiconductors, Phys. Chem. Chem. Phys. 19 (2017) 10116–10124.
[45] N. Lakshminarasimhan, A.D. Bokare, W. Choi, Effect of agglomerated state in mesoporous TiO_2 on the morphology of photodeposited Pt and photocatalytic activity, J. Phys. Chem. C 116 (2012) 17531–17539.
[46] Y. Park, W. Kim, D. Monllor-Satoca, T. Tachikawa, T. Majima, W. Choi, Role of interparticle charge transfers in agglomerated photocatalyst nanoparticles: demonstration in aqueous suspension of dye-sensitized TiO_2, J. Phys. Chem. Lett. 4 (2013) 189–194.
[47] S. Kashiwaya, T. Toupance, A. Klein, W. Jaegermann, Fermi level positions and induced band bending at single crystalline anatase (101) and (001) surfaces: origin of the enhanced photocatalytic activity of facet engineered crystals, Adv. Energ. Mater. (2018), http://dx.doi.org/10.1002/aenm.201802195.
[48] K. Ozawa, M. Emori, S. Yamamoto, R. Yukawa, S. Yamamoto, R. Hobara, K. Fujikawa, H. Sakama, I. Matsuda, Electron–hole recombination time at TiO_2 single-crystal surfaces: Influence of surface band bending, J. Phys. Chem. Lett. 5 (2014) 1953–1957.
[49] A. Meng, S. Wu, B. Cheng, J. Yu, J. Xu, Hierarchical TiO_2/$Ni(OH)_2$ composite fibers with enhanced photocatalytic CO_2 reduction performance, J. Mater. Chem. A 6 (2018) 4729–4736.
[50] K. Shirai, G. Fazio, T. Sugimoto, D. Selli, L. Ferraro, K. Watanabe, M. Haruta, B. Ohtan, H. Kurata, C.D. Valentin, Y. Matsumoto, Water-assisted hole trapping at the highly curved surface of nano-TiO_2 photocatalyst, J. Am. Chem. Soc. 140 (2018) 1415–1422.
[51] R. Sanjinés, H. Tang, H. Berger, F. Gozzo, G. Margaritondo, F. Lévy, Electronic structure of anatase TiO_2 oxide, J. Appl. Phys. 75 (1994) 2945–2951.
[52] L. Guan, X. Chen, Photoexcited charge transport and accumulation in anatase TiO_2, ACS Appl. Energy Mater. 1 (2018) 4313–4320.
[53] T. Di, J. Zhang, B. Cheng, J. Yu, Hierarchically nanostructured porous TiO_2(B) with superior photocatalytic CO_2 reduction activity, Sci. China-Chem. 61 (2018) 344–350.
[54] H. Onishi, Y. Iwasawa, Reconstruction of TiO_2(110) surface: STM study with atomic-scale resolution, Surf. Sci. 313 (1994) L783–L789.
[55] F. Sieland, J. Schneider, D.W. Bahnemann, Fractal charge carrier kinetics in TiO_2, J. Phys. Chem. C 121 (2017) 24282–24291.
[56] M. Dumortier, T. Bosserez, J. Rongé, J.A. Martens, S. Haussener, Combined experimental–numerical analysis of transient phenomena in a photoelectrochemical water splitting cell, J. Phys. Chem. C 120 (2016) 3705–3714.
[57] H.-X. Zhang, Y.F. Zhu, M. Zhao, Interface charge transfer and enhanced visible light response of graphene/anatase TiO_2 (110) systems with and without oxygen vacancy: a DFT + U calculation, Appl. Surf. Sci. 420 (2017) 105–109.
[58] B. Choudhury, A. Choudhury, Oxygen defect dependent variation of band gap, Urbach energy and luminescence property of anatase, anatase–rutile mixed phase and of rutile phases of TiO_2 nanoparticles, Physica E 56 (2014) 364–371.

[59] F. Xu, J. Zhang, B. Zhu, J. Yua, J. Xu, $CuInS_2$ sensitized TiO_2 hybrid nanofibers for improved photocatalytic CO_2 reduction, Appl. Catal. B: Environ. 230 (2018) 194–202.
[60] M. Setvin, U. Aschauer, J. Hulva, T. Simschitz, B. Daniel, M. Schmid, A. Selloni, U. Diebold, Following the reduction of oxygen on TiO_2 anatase (101) step by step, J. Am. Chem. Soc. 138 (2016) 9565–9571.
[61] M.K. Nowotny, L.R. Sheppard, T. Bak, J. Nowotny, Defect chemistry of titanium dioxide. Application of defect engineering in processing of TiO_2-based photocatalysts, J. Phys. Chem. C 112 (2008) 5275–5300.
[62] Z. Jiao, M. Shang, J. Liu, G. Lu, X. Wang, Y. Bi, The charge transfer mechanism of Bi modified TiO_2 nanotube arrays: TiO_2 serving as a "charge-transfer-bridge", Nano Energy 31 (2017) 96–104.
[63] N.O. Gopal, H.-H. Lo, S.-C. Sheu, S.-C. Ke, A potential site for trapping photogenerated holes on rutile TiO_2 surface as revealed by EPR spectroscopy: an avenue for enhancing photocatalytic activity, J. Am. Chem. Soc. 132 (2010) 10982–10983.
[64] T. Lana-Villarreal, A. Rodes, J.M. Pérez, R. Gómez, A spectroscopic and electrochemical approach to the study of the interactions and photoinduced electron transfer between catechol and anatase nanoparticles in aqueous solution, J. Am. Chem. Soc. 127 (2005) 12601–12611.
[65] E.M. Samsudin, S.B. Hamid, Effect of band gap engineering in anionic-doped TiO_2 photocatalyst, Appl. Surf. Sci. 391 (2017) 326–336.
[66] X. Pan, Y. Xu, Defect-mediated growth of noble-metal (Ag, Pt, and Pd) nanoparticles on TiO_2 with oxygen vacancies for photocatalytic redox reactions under visible light, J. Phys. Chem. C 117 (2013) 17996–18005.
[67] S.K. Cushing, F. Meng, J. Zhang, B. Ding, C.K. Chen, C.-J. Chen, R.-S. Liu, A.D. Bristow, J. Bright, P. Zheng, N. Wu, Effects of defects on photocatalytic activity of hydrogen-treated titanium oxide nanobelts, ACS Catal. 7 (2017) 1742–1748.
[68] L. Liu, Y. Jiang, H. Zhao, J. Chen, J. Cheng, K. Yang, Y. Li, Engineering coexposed {001} and {101} facets in oxygen-deficient TiO_2 nanocrystals for enhanced CO_2 photoreduction under visible light, ACS Catal. 6 (2016) 1097–1108.
[69] P. Wan, Z.D. Hood, S.P. Adhikarie, Y. Xug, S. Yang, S. Wu, Enhancing the photoresponse and photocatalytic properties of TiO_2 by controllably tuning defects across {101} facets, Appl. Surf. Sci. 434 (2018) 711–716.
[70] T. Xia, Y. Zhang, J. Murowchick, X. Chen, Vacuum-treated titanium dioxide nanocrystals: optical properties, surface disorder, oxygen vacancy, and photocatalytic activities, Catal. Today 225 (2014) 2–9.
[71] M. Freitag, J. Teuscher, Y. Saygili, X. Zhang, F. Giordano, P. Liska, J. Hua, S.M. Zakeeruddin, J.-E. Moser, M. Grätzel, A. Hagfeldt, Dye-sensitized solar cells for efficient power generation under ambient lighting, Nat. Photonics 11 (2017) 372–378.
[72] S. Lettieri, V. Gargiulo, D.K. Pallotti, G. Vitiello, P. Maddalena, M. Alfè, R. Marotta, Evidencing opposite charge-transfer processes at TiO_2/graphene-related materials interface through a combined EPR, photoluminescence and photocatalysis assessment, Catal. Today 315 (2018) 19–30.
[73] R.V. Nair, P.K. Gayathri, V.S. Gummaluri, P.M.G. Nambissan, C. Vijayan, Large bandgap narrowing in rutile TiO_2 aimed towards visible light applications and its correlation with vacancy-type defects history and transformation, J. Phys. D: Appl. Phys. 51 (2018) 045107.
[74] S. Pigeot-Rémy, F. Dufour, A. Herissan, V. Ruaux, F. Maugé, R. Hazime, C. Foronato, C. Guillard, C. Chaneac, O. Durupthy, C. Colbeau-Justin, S. Cassaignon, Bipyramidal anatase TiO_2 nanoparticles, a highly efficient photocatalyst? Towards a better understanding of the reactivity, Appl. Catal. B: Environ. 203 (2017) 324–334.
[75] L. Jing, S. Li, S. Song, L. Xue, H. Fu, Investigation on the electron transfer between anatase and rutile in nano-sized TiO_2 by means of surface photovoltage technique and its effects on the photocatalytic activity, Sol. Energy Mater. Sol. Cells 92 (2008) 1030–1036.
[76] M.G. Méndez-Medrano, E. Kowalska, A. Lehoux, A. Herissan, B. Ohtani, D. Bahena, V. Briois, C. Colbeau-Justin, J.L. Rodríguez-López, H. Remita, Surface Modification of TiO_2 with Ag nanoparticles and CuO nanoclusters for application in photocatalysis, J. Phys. Chem. C 120 (2016) 5143–5154.
[77] E. Baldini, T. Palmieri, E. Pomarico, G. Auböck, M. Chergui, Clocking the ultrafast electron cooling in anatase titanium dioxide nanoparticles, ACS Photonics 5 (2018) 1241–1249.
[78] A.J.E. Rettie, W.D. Chemelewski, D. Emin, C. Buddie Mullins, Unravelling small-polaron transport in metal oxide photoelectrodes, J. Phys. Chem. Lett. 7 (2016) 471–479.
[79] A. Naldoni, M. Allieta, S. Santangelo, M. Marelli, F. Fabbri, S. Cappelli, C.L. Bianchi, R. Psaro, V. Dal Santo, Effect of nature and location of defects on bandgap narrowing in black TiO_2 nanoparticles, J. Am. Chem. Soc. 134 (2012) 7600–7603.
[80] B. Liu, X. Zhao, The synergetic effect of V and Fe-co-doping in TiO_2 studied from the DFT + U first-principle calculation, Appl. Surf. Sci. 399 (2017) 654–662.
[81] M. Kapilashrami, Y. Zhang, Y.-S. Liu, A. Hagfeldt, J. Guo, Probing the optical property and electronic structure of TiO_2 nanomaterials for renewable energy applications, Chem. Rev. 114 (2014) 9662–9707.
[82] F.D. Angelis, C.D. Valentin, S. Fantacci, A. Vittadini, A. Selloni, Theoretical studies on anatase and less common TiO_2 phases: bulk, surfaces, and nanomaterials, Chem. Rev. 114 (2014) 9708–9753.
[83] H. Park, H. Kim, G.H. Moon, W. Choi, Photoinduced charge transfer processes in solar photocatalysis based on modified TiO_2, Energy Environ. Sci. 9 (2016) 411–433.
[84] V.K. Etacheri, C. Di Valentin, J. Schneider, D. Bahnemann, S.C. Pillai, Visible-light activation of TiO_2 photocatalysts: advances in theory and experiments, J. Photochem. Photobiol. C: Rev. 25 (2015) 1–29.
[85] J. Wen, X. Li, W. Liu, Y. Fang, J.X.Y. Xu, Photocatalysis fundamentals and surface modifications of TiO_2 materials, Chin. J. Catal. 36 (2015) 2049–2070.
[86] K. Nakata, A. Fujishima, TiO_2 photocatalysis: design and applications, J. Photochem. Photobiol. C: Rev. 13 (2012) 169–189.
[87] Y. Nosaka, A.Y. Nosaka, Generation and detection of reactive oxygen species in photocatalysis, Chem. Rev. 117 (2017) 11302–11336.
[88] R. Qian, H. Zong, J. Schneider, G. Zhou, T. Zhao, Y. Li, J. Yang, D.W. Bahnemann, J.H. Pan, Charge carrier trapping, recombination and transfer during TiO_2 photocatalysis: an overview, Catal. Today (2018), http://dx.doi.org/10.1016/j.cattod.2018.10.053.
[89] X. Du, E.R. Weeks, Energy barriers, entropy barriers, and non-Arrhenius behavior in a minimal glassy model, Phys. Rev. E 93 (2016) 062613.
[90] M. Batzill, K. Katsiev, D.J. Gaspar, U. Diebold, Variations of the local electronic surface properties of TiO_2 (110) induced by intrinsic and extrinsic defects, Phys. Rev. B 66 (2002) 235401.
[91] L. Forro, O. Chauvet, D. Emin, L. Zuppiroli, H. Berger, F. Lévy, High mobility n-type charge carriers in large single crystals of anatase (TiO_2), J. Appl. Phys. 75 (1994) 633–635.
[92] X. Chen, C. Burda, The electronic origin of the visible-light absorption properties of C-, N- and S-doped TiO_2 nanomaterials, J. Am. Chem. Soc. 130 (2008) 5018–5019.
[93] L.-L. Tan, W.-J. Ong, S.-P. Chai, A.R. Mohamed, Visible-light-activated oxygen-rich TiO_2 as next generation photocatalyst: importance of annealing temperature on the photoactivity toward reduction of carbon dioxide, Chem. Eng. J. 283 (2016) 1254–1263.
[94] J. Jupille, G. Thornton, Defects on TiO_2—key pathways to important surface process, in: Defects at Oxide Surface, 2015, pp. 81–121.
[95] C. Rath, P. Mohanty, A.C. Pandey, N.C. Mishra, Oxygen vacancy induced structural phase transformation in TiO_2 nanoparticles, J. Phys. D: Appl. Phys. 42 (2009) 205101.
[96] B.J. Morgan, G.W. Watson, A density functional theory + U study of oxygen vacancy formation at the (110), (100), (101), and (001) surfaces of rutile TiO_2, J. Phys. Chem. C 113 (2009) 7322–7328.
[97] K.K. Ghuman, C.V. Singh, Self-trapped charge carriers in defected amorphous TiO_2, J. Phys. Chem. C 120 (2016) 27910–27916.
[98] S. Wendt, R. Schaub, J. Matthiesen, E.K. Vestergaard, E. Wahlström, M.D. Rasmussen, P. Thostrup, L.M. Molina, E. Lægsgaard, I. Stensgaard, B. Hammer, F. Besenbacher, Oxygen vacancies on TiO_2 (110) and their interaction with H_2O and O_2: a combined high-resolution STM and DFT study, Surf. Sci. 598 (2005) 226–245.
[99] L.A. Miccio, M. Setvin, M. Mülle, M. Abadía, I. Piquero, J. Lobo-Checa, F. Schiller, C. Rogero, M. Schmid, D. Sánchez-Portal, U. Diebold, J.E. Ortega, Interplay between steps and oxygen vacancies on curved TiO_2(110), Nano Lett. 16 (2016) 2017–2022.
[100] B. Yoon, D. Yadav, R. Raj, E. Sortino, S. Ghose, P. Sarin, D. Shoemaker, Measurement of O and Ti atom displacements in TiO_2 during flash sintering experiments, J. Am. Ceram. Soc. 101 (2018) 1811–1817.
[101] M.A. Henderson, A surface perspective on self-diffusion in rutile TiO_2, Surf. Sci. 419 (1999) 174–187.
[102] T.S. Bjørheim, A. Kuwabara, T. Norby, Defect chemistry of rutile TiO_2 from first principles calculations, J. Phys. Chem. C 117 (2013) 5919–5930.
[103] A.C. Papageorgiou, N.S. Beglitis, C.L. Pang, G. Teobaldi, G. Cabailh, Q. Chen, A.J. Fisher, W.A. Hofer, G. Thornton, Electron traps and their effect on the surface chemistry of TiO_2(110), Proc. Natl. Acad. Sci. U.S.A. 107 (2010) 2391–2396.
[104] M. Liu, X. Qiu, M. Miyauchi, K. Hashimoto, Cu(II) oxide amorphous nanoclusters grafted Ti^{3+} self-doped TiO_2: an efficient visible light photocatalyst, Chem. Mater. 23 (2011) 5282–5286.
[105] B. Qiu, Y. Zhou, Y. Ma, X. Yang, W. Sheng, M. Xing, J. Zhang, Facile synthesis of the Ti^{3+} self-doped TiO_2-graphene nanosheet composites with enhanced photocatalysis, Sci. Rep. 5 (2015) 8591.
[106] Y. Yoon, Y. Du, J.C. Garcia, Z. Zhu, Z. Wang, N.G. Petrik, G.A. Kimmel, Z. Dohnalek, M.A. Henderson, R. Rousseau, N. Aaron Deskins, I. Lyubinetsky, Anticorrelation between surface and subsurface point defects and the impact on the redox chemistry of TiO_2(110), ChemPhysChem 16 (2015) 313–321.
[107] K. Li, S. Gao, Q. Wang, H. Xu, Z. Wang, B. Huang, Y. Dai, J. Lu, In-situ-reduced synthesis of Ti^{3+} self-doped TiO_2/g-C_3N_4 heterojunctions with high photocatalytic performance under LED light irradiation, ACS Appl. Mater. Interfaces 7 (2015) 9023–9030.
[108] F. Zuo, K. Bozhilov, R.J. Dillon, L. Wang, P. Smith, X. Zhao, C. Bardeen, P. Feng, Active facets on titanium(III)-doped TiO_2: an effective strategy to improve the visible-light photocatalytic activity, Angew. Chem. Int. Ed. 51 (2012) 6223–6226.
[109] S.G. Ullattil, P. Periyat, A 'one pot' gel combustion strategy towards Ti^{3+} self-doped 'black' anatase TiO_{2-x} solar photocatalyst, J. Mater. Chem. A 4 (2016) 5854–5858.
[110] T. Sekiya, T. Yagisawa, N. Kamiya, D.D. Mulmi, S. Kurita, Y. Murakami, T. Kodaira, Defects in anatase TiO_2 single crystal controlled by heat treatments, J. Phys. Soc. Jpn. 73 (2004) 703–710.
[111] L.Q. Wang, D.R. Baer, M.H. Engelhard, Creation of variable concentrations of defects on TiO_2 (110) using low-density electron beams, Surf. Sci. 320 (1994) 295–306.

[112] M.J. Jackman, A.G. Thomas, C. Muryn, Photoelectron spectroscopy study of stoichiometric and reduced anatase TiO_2 (101) surfaces: the effect of subsurface defects on water adsorption at near-ambient pressures, J. Phys. Chem. C 119 (2015) 13682–13690.

[113] S. Mezhenny, P. Maksymovych, T.L. Thompson, O. Diwald, D. Stahl, S.D. Walck, J.T. Yates Jr., STM studies of defect production on the TiO_2 (110)-(1×1) and TiO_2 (110)-(1×2) surfaces induced by UV irradiation, Chem. Phys. Lett. 369 (2003) 152–158.

[114] Z. Zhang, M.N. Hedhili, H. Zhu, P. Wang, Electrochemical reduction induced self-doping of Ti^{3+} for efficient water splitting performance on TiO_2 based photoelectrodes, Phys. Chem. Chem. Phys. 15 (2013) 15637–15644.

[115] R. Fu, S. Gao, H. Xu, Q. Wang, Z. Wang, B. Huang, Y. Dai, Fabrication of Ti^{3+} self-doped TiO_2(A) nanoparticle/TiO_2(R) nanorod heterojunctions with enhanced visible-light-driven photocatalytic properties, RSC Adv. 4 (2014) 37061–37069.

[116] Z. Zheng, B. Huang, X. Meng, J. Wang, S. Wang, Z. Lou, Z. Wang, X. Qin, X. Zhang, Y. Dai, Metallic zinc-assisted synthesis of Ti^{3+} self-doped TiO_2 with tunable phase composition and visible-light photocatalytic activity, Chem. Commun. 49 (2013) 868–870.

[117] A. Wahl, J. Augustynski, Charge carrier transport in nanostructured anatase TiO_2 films assisted by the self-doping of nanoparticles, J. Phys. Chem. B 120 (1998) 7820–7828.

[118] M. Xing, W. Fang, M. Nasir, Y. Ma, J. Zhang, M. Anpo, Self-doped Ti^{3+}-enhanced TiO_2 nanoparticles with a high-performance photocatalysis, J. Catal. 297 (2013) 236–243.

[119] G. Charlton, P.B. Howes, C.L. Nicklin, P. Steadman, J.S.G. Taylor, C.A. Muryn, S.P. Harte, J. Mercer, R. McGrath, D. Norman, T.S. Turner, G. Thornton, Relaxation of TiO_2 (110)-(1×1) using surface X-ray diffraction, Phys. Rev. Lett. 78 (1997) 495–498.

[120] U. Diebold, The surface science of titanium dioxide, Surf. Sci. Rep. 48 (2003) 53–229.

[121] T.R. Gordon, M. Cargnello, T. Paik, F. Mangolini, R.T. Weber, P. Fornasiero, C.B. Murray, Nonaqueous synthesis of TiO_2 nanocrystals using TiF_4 to engineer morphology, oxygen vacancy concentration, and photocatalytic activity, J. Am. Chem. Soc. 134 (2012) 6751–6761.

[122] I. Nakamura, N. Negishi, S. Kutsuna, T. Ihara, S. Sugihara, K. Takeuchi, Role of oxygen vacancy in the plasma-treated TiO_2 photocatalyst with visible light activity for NO removal, J. Mol. Catal. A: Chem. 161 (2000) 205–212.

[123] M. Lazzeri, A. Vittadini, A. Selloni, Structure and energetics of stoichiometric TiO_2 anatase surfaces, Phys. Rev. B 63 (2001) 155409.

[124] H. Tang, Z. Cheng, S. Dong, X. Cui, H. Feng, X. Ma, B. Luo, A. Zhao, J. Zhao, B. Wang, Understanding the intrinsic chemical activity of anatase TiO_2(001)-(1×4) surface, J. Phys. Chem. C 121 (2017) 1272–1282.

[125] Y. Liang, S. Gan, S.A. Chambers, E.I. Altman, Surface structure of anatase TiO_2 (001): reconstruction, atomic steps, and domains, Phys. Rev. B 63 (2001) 235402.

[126] M. Setvín, U. Aschauer, P. Scheiber, Y.F. Li, W. Hou, M. Schmid, A. Selloni, U. Diebold, Reaction of O_2 with subsurface oxygen vacancies on TiO_2 anatase (101), Science 341 (2013) 988–991.

[127] U. Martinez, J.Ø. Hansen, E. Lira, H.H. Kristoffersen, P. Huo, R. Bechstein, E. Lægsgaard, F. Besenbacher, B. Hammer, S. Wendt, Reduced step edges on rutile TiO_2(110) as competing defects to oxygen vacancies, Phys. Rev. Lett. 109 (2012) 155501.

[128] G. Liu, H.G. Yang, X. Wang, L. Cheng, H. Lu, L. Wang, G. Qing (Max) Lu, H.M. Cheng, Enhanced photoactivity of oxygen-deficient anatase TiO_2 sheets with dominant {001} facets, J. Phys. Chem. C 113 (2009) 21784–21788.

[129] G. Liu, H.G. Yang, X. Wang, L. Cheng, J. Pan, G. Qing (Max) Lu, H.M. Cheng, Visible light responsive nitrogen doped anatase TiO_2 sheets with dominant {001} facets derived from TiN, J. Am. Chem. Soc. 131 (2009) 12868–12869.

[130] A. Kim, D.P. Debecker, F. Devred, V. Dubois, C. Sanchez, C. Sassoye, CO_2 methanation on Ru/TiO_2 catalysts: On the effect of mixing anatase and rutile TiO_2 supports, Appl. Catal. B: Environ. 220 (2018) 615–625.

[131] L.B. Vilhelmsen, B. Hammer, Identification of the catalytic site at the interface perimeter of Au clusters on rutile TiO_2 (110), ACS Catal. 4 (2014) 1626–1631.

[132] H. Cheng, A. Selloni, Surface and subsurface oxygen vacancies in anatase TiO_2 and differences with rutile, Phys. Rev. B 79 (2009) 092101.

[133] R. Verma, S.K. Samdarshi, Correlating oxygen vacancies and phase ratio/interface with efficient photocatalytic activity in mixed phase TiO_2, J. Alloys Compd. 629 (2015) 105–112.

[134] M.V. Ganduglia-Pirovano, A. Hofmann, J. Sauer, Oxygen vacancies in transition metal and rare earth oxides: current state of understanding and remaining challenges, Surf. Sci. Rep. 62 (2007) 219–270.

[135] R. Schaub, E. Wahlström, A. Rønnau, E. Lægsgaard, I. Stensgaard, F. Besenbacher, Oxygen-mediated diffusion of oxygen vacancies on the TiO_2(110) surface, Science 299 (2003) 377–379.

[136] E. Wahlström, N. Lopez, R. Schaub, P. Thostrup, A. Rønnau, C. Africh, E. Lægsgaard, J.K. Nørskov, F. Besenbacher, Bonding of gold nanoclusters to oxygen vacancies on rutile TiO_2(110), Phys. Rev. Lett. 90 (2003) 026101.

[137] C.M. Yim, C.L. Pang, G. Thornton, Oxygen vacancy origin of the surface band-gap state of TiO_2(110), Phys. Rev. Lett. 104 (2010) 036806.

[138] V.E. Henrich, G. Dresselhaus, H.J. Zeiger, Observation of two-dimensional phases associated with defect states on the surface of TiO_2, Phys. Rev. Lett. 36 (1976) 1335–1338.

[139] X. Mao, X. Lang, Z. Wang, Q. Hao, B. Wen, Z. Ren, D. Dai, C. Zhou, L.M. Liu, X. Yang, Band-gap states of TiO_2 (110): major contribution from surface defects, J. Phys. Chem. Lett. 4 (2013) 3839–3844.

[140] A.G. Thomas, W.R. Flavell, A.K. Mallick, A.R. Kumarasinghe, D. Tsoutsou, N. Khan, C. Chatwin, S. Rayner, G.C. Smith, R.L. Stockbauer, S. Warren, T.K. Johal, S. Patel, D. Holland, A. Taleb, F. Wiame, Comparison of the electronic structure of anatase and rutile TiO_2 single-crystal surfaces using resonant photoemission and X-ray absorption spectroscopy, Phys. Rev. B 75 (2007) 035105.

[141] B.J. Morgan, G.W. Watson, A DFT + U description of oxygen vacancies at the TiO_2 rutile (110) surface, Surf. Sci. 601 (2007) 5034–5041.

[142] G.S. Herman, Z. Dohnálek, N. Ruzycki, U. Diebold, Experimental investigation of the interaction of water and methanol with anatase-TiO_2 (101), J. Phys. Chem. B 107 (2003) 2788–2795.

[143] M.R. Ranade, A. Navrotsky, H.Z. Zhang, J.F. Banfield, S.H. Elder, A. Zaban, P.H. Borse, S.K. Kulkarni, G.S. Doran, H.J. Whitfield, Energetics of nanocrystalline TiO_2, Proc. Natl. Acad. Sci. U.S.A. 99 (2002) 6476–6481.

[144] Y. He, O. Dulub, H. Cheng, A. Selloni, U. Diebold, Evidence for the predominance of subsurface defects on reduced anatase TiO_2(101), Phys. Rev. Lett. 102 (2009) 106105.

[145] A.G. Thomas, W.R. Flavell, A.R. Kumarasinghe, A.K. Mallick, D. Tsoutsou, G.C. Smith, R. Stockbauer, S. Patel, M. Grätzel, R. Hengerer, Resonant photoemission of anatase TiO_2 (101) and (001) single crystals, Phys. Rev. B 67 (2003) 035110.

[146] G.S. Herman, M.R. Sievers, Y. Gao, Structure determination of the two-domain (1×4) anatase TiO_2 (001) surface, Phys. Rev. Lett. 84 (2000) 3354–3357.

[147] R. Hengerer, B. Bolliger, M. Erbudak, M. Grätzel, Structure and stability of the anatase TiO_2 (101) and (001) surfaces, Surf. Sci. 460 (2000) 162–169.

[148] M. Lazzeri, A. Selloni, Stress-driven reconstruction of an oxide surface: the anatase TiO_2 (001)-(1×4) surface, Phys. Rev. Lett. 87 (2001), 266105-1–4.

[149] J.C. Woicik, E.J. Nelson, L. Kronik, M. Jain, J.R. Chelikowsky, D. Heskett, L.E. Berman, G.S. Herman, Hybridization and bond-orbital components in site-specific X-ray photoelectron spectra of rutile TiO_2, Phys. Rev. Lett. 89 (2002) 077401.

[150] J.P. Perdew, K. Burke, M. Ernzerhof, Generalized gradient approximation made simple, Phys. Rev. Lett. 77 (1996) 3865–3868.

[151] D.J. Shu, S.T. Ge, M. Wang, N.B. Ming, Interplay between external strain and oxygen vacancies on a rutile TiO_2 (110) surface, Phys. Rev. Lett. 101 (2008) 116102.

[152] D.J. Shu, F. Liu, X.G. Gong, Simple generic method for predicting the effect of strain on surface diffusion, Phys. Rev. B 64 (2001) 245410.

[153] B. Yang, F. Liu, M.G. Lagally, Local strain-mediated chemical potential control of quantum dot self-organization in heteroepitaxy, Phys. Rev. Lett. 92 (2004) 025502.

[154] G.H. Lu, M. Cuma, F. Liu, First-principles study of strain stabilization of Ge (105) facet on Si (001), Phys. Rev. B 72 (2005) 125415.

[155] Y. Yang, L.-C. Yin, Y. Guo, P. Niu, J.-Q. Wang, L. Gu, X. Chen, G. Liu, L. Wang, H. Cheng, An unusual strong visible-light absorption band in red anatase TiO_2 photocatalyst induced by atomic hydrogen-occupied oxygen vacancies, Adv. Mater. 30 (2018) 1704479.

[156] Z. Song, J. Hrbek, R. Osgood, Formation of TiO_2 nanoparticles by reactive-layer-assisted deposition and characterization by XPS and STM, Nano Lett. 5 (2005) 1327–2133.

[157] S. Selcuk, A. Selloni, Influence of external electric field on oxygen vacancies at anatase (101) surface, J. Chem. Phys. 141 (2014) 084705.

[158] P. Scheiber, M. Fidler, O. Dulub, M. Schmid, U. Diebold, W. Hou, U. Aschauer, A. Selloni, (Sub)Surface mobility of oxygen vacancies at the TiO_2 anatase (101) surface, Phys. Rev. Lett. 109 (2012) 136103.

[159] Z. Zhang, Q. Ge, S.C. Li, B.D. Kay, J.M. White, Z. Dohnálek, Imaging intrinsic diffusion of bridge-bonded oxygen vacancies on TiO_2 (110), Phys. Rev. Lett. 99 (2007) 126105.

[160] C.Y. Wu, K.J. Tu, J.P. Deng, Y.S. Lo, C.H. Wu, Markedly enhanced surface hydroxyl groups of TiO_2 nanoparticles with superior water-dispersibility for photocatalysis, Materials 10 (2017) 566.

[161] K. Lv, X. Guo, X. Wu, Q. Li, W. Ho, M. Li, H. Ye, D. Du, Photocatalytic selective oxidation of phenol to produce dihydroxybenzenes in a TiO_2/UV system: hydroxyl radical versus hole, Appl. Catal. B: Environ. 199 (2016) 405–411.

[162] M. Terracciano, V. Galstyan, I. Rea, M. Casalino, L. De Stefano, G. Sbervegleri, Chemical modification of TiO_2 nanotube arrays for label-free optical biosensing applications, Appl. Surf. Sci. 419 (2017) 235–240.

[163] R. Schaub, P. Thostrup, N. Lopez, E. Lægsgaard, I. Stensgaard, J.K. Nørskov, F. Besenbacher, Oxygen vacancies as active sites for water dissociation on rutile TiO_2 (110), Phys. Rev. Lett. 87 (2001) 266104.

[164] O. Bikondoa, C.L. Pang, R. Ithnin, C.A. Muryn, H. Onishi, G. Thornton, Direct visualization of defect-mediated dissociation of water on TiO_2 (110), Nat. Mater. 5 (2006) 189–192.

[165] S. Wendt, J. Matthiesen, R. Schaub, E.K. Vestergaard, E. Lægsgaard, F. Besenbacher, B. Hammer, Formation and splitting of paired hydroxyl groups on reduced TiO_2 (110), Phys. Rev. Lett. 96 (2006) 066107.

[166] E. Cho, S. Han, H.S. Ahn, K.R. Lee, S.K. Kim, C.S. Hwang, First-principles study of point defects in rutile TiO_2, Phys. Rev. B 73 (2006) 193202.

[167] H. Iddir, S. Öğüt, P. Zapol, N.D. Browning, Diffusion mechanisms of native point defects in rutile TiO_2: ab initio total-energy calculations, Phys. Rev. B 75 (2007) 073203.

[168] K.T. Park, M.H. Pan, V. Meunier, E.W. Plummer, Surface reconstructions of TiO_2 (110) driven by suboxides, Phys. Rev. Lett. 96 (2006) 226105.
[169] N. Shibata, A. Goto, S.Y. Choi, T. Mizoguchi, S.D. Findlay, T. Yamamoto, Y. Ikuhara, Direct imaging of reconstructed atoms on TiO_2 (110) surfaces, Science 322 (2008) 570–573.
[170] J. Yang, B. Liu, H. Xie, X. Zhao, C. Terashima, A. Fujishima, K. Nakata, In situ photoconductivity kinetic study of nano-TiO_2 during the photocatalytic oxidation of formic acid: effects of new recombination and current doubling, J. Phys. Chem. C 119 (2015) 21711–21722.
[171] S. Ardo, G.J. Meyer, Photodriven heterogeneous charge transfer with transition-metal compounds anchored to TiO_2 semiconductor surfaces, Chem. Soc. Rev. 38 (2009) 115–164.
[172] B. Liu, X. Wang, L. Wen, X. Zhao, Investigation of electron behavior in nano-TiO_2 photocatalysis by using in situ open-circuit voltage and photoconductivity measurements, Chem. A: Eur. J. 19 (2013) 10751–10759.
[173] F. Wang, W. Ge, T. Shen, B. Ye, Z. Fu, Y. Lu, The effect of bulk/surface defects ratio change on the photocatalysis of TiO_2 nanosheet film, Appl. Surf. Sci. 410 (2017) 513–518.
[174] A.S. Alexandrov, N. Mott, Polarons & Bipolarons, World Scientific Pub. Co. Inc., Singapore, 1996, pp. 1–191.
[175] D. Emin, Polarons, Cambridge University Press, Cambridge, UK, 2013, pp. 1–227.
[176] D. Emin, Optical properties of large and small polarons and bipolarons, Phys. Rev. B: Condens. Matter Mater. Phys. 48 (1993) 13691–13702.
[177] A.L. Shluger, A.M. Stoneham, Small polarons in real crystals: concepts and problems, J. Phys.: Condens. Matter 5 (1993) 3049–3086.
[178] D. Emin, Small polarons, Phys. Today 35 (1982) 34–40.
[179] J.J. Carey, K.P. McKenna, Does polaronic self-trapping occur at anatase TiO_2 surfaces, J. Phys. Chem. C (2018), http://dx.doi.org/10.1021/acs.jpcc.8b09437.
[180] M. D'Arienzo, J. Carbajo, A. Bahamonde, M. Crippa, S. Polizzi, R. Scotti, L. Wahba, T. Morazzoni, Photogenerated defects in shape-controlled TiO_2 anatase nanocrystals: a probe to evaluate the role of crystal facets in photocatalytic processes, J. Am. Chem. Soc. 133 (2011) 17652–17661.
[181] D. Zhang, M. Yang, S. Dong, Hydroxylation of the rutile TiO_2(110) surface enhancing its reducing power for photocatalysis, J. Phys. Chem. C 119 (2015) 1451–1456.
[182] A. Janotti, C. Franchini, J.B. Varley, G. Kresse, C.G. Van de Walle, Dual behavior of excess electrons in rutile TiO_2, Phys. Stat. Sol. RRl 7 (2013) 199–203.
[183] B. Yan, D. Wan, X. Chi, C. Li, M.R. Motapothula, S. Hooda, P. Yang, Z. Huang, S. Zeng, A.G. Ramesh, S.J. Pennycook, A.R. Ariando, J. Martin, T. Venkatesan, Anatase TiO_2—a model system for large polaron transport, ACS Appl. Mater. Interfaces 10 (2018) 38201–38208.
[184] A.J. Cohen, P. Mori-Sanchez, W. Yang, Insights into current limitations of density functional theory, Science 321 (2008) 792–794.
[185] C.J. Calzado, N.C. Hernandez, J.F. Sanz, Effect of on-site coulomb repulsion term U on the band-gap states of the reduced rutile (110) TiO_2 surface, Phys. Rev. B 77 (2008) 045118–045120.
[186] M. Reticcioli, M. Setvin, X. Hao, P. Flauger, G. Kresse, M. Schmid, U. Diebold, C. Franchini, Polaron-driven surface reconstructions, Phys. Rev. X 7 (2017) 031053.
[187] Y. Zhang, Z. Xing, X. Liu, Z. Li, X. Wu, J. Jiang, M. Li, Q. Zhu, W. Zhou, Ti^{3+} self-doped blue TiO_2(B) single-crystalline nanorods for efficient solar-driven photocatalytic performance, ACS Appl. Mater. Interfaces 8 (2016) 26851–26859.
[188] L. Zhang, C. Ni, H. Jiu, H. Chen, G. Qi, Preparation of anatase/TiO_2(B) TiO_2 nanosheet for high performance of photocatalytic reduction of CO_2, J. Mater. Sci. Mater. Electron. 28 (2017) 6601–6606.
[189] B.J. Morgan, G.W. Watson, Intrinsic n-type defect formation in TiO_2: a comparison of rutile and anatase from GGA + U calculations, J. Phys. Chem. C 114 (2010) 2321–2328.
[190] G. Mattioli, F. Filippone, P. Alippi, A.A. Bonapasta, Ab initio study of the electronic states induced by oxygen vacancies in rutile and anatase TiO_2, Phys. Rev. B 78 (2008) 241201.
[191] E. Finazzi, C.D. Valentin, G. Pacchioni, A. Selloni, Excess electron states in reduced bulk anatase TiO_2: comparison of standard GGA, GGA + U, and hybrid DFT calculations, J. Chem. Phys. 129 (2008) 154113.
[192] L. Liu, Q. Liu, W. Xiao, C. Pan, Z. Wang, O_2 adsorption and dissociation on an anatase (101) surface with a subsurface Ti interstitial, Phys. Chem. Chem. Phys. 18 (2016) 4569–4576.
[193] Y. Yoon, Y. Du, J.C. Garcia, Z. Zhu, Z.T. Wang, N.G. Petrik, G.A. Kimmel, Z. Dohnalek, M.A. Henderson, R. Rousseau, Anticorrelation between surface and subsurface point defects and the impact on the redox chemistry of TiO_2(110), ChemPhysChem 16 (2015) 313–321.
[194] K.T. Park, M. Pan, V. Meunier, E.W. Plummer, Reoxidation of TiO_2 (110) via Ti interstitials and line defects, Phys. Rev. B 75 (2007) 245415–245420.
[195] K. Morita, T. Shibuya, K. Yasuoka, Stability of excess electrons introduced by Ti interstitial in rutile TiO_2 (110) surface, J. Phys. Chem. C 121 (2017) 1602–1607.
[196] C.D. Valentin, G. Pacchioni, A. Selloni, Reduced and n-type doped TiO_2: nature of Ti^{3+} species, J. Phys. Chem. C 113 (2009) 20543–20552.
[197] P.G. Moses, A. Janotti, C. Franchini, G. Kresse, C.G. Van de Walle, Donor defects and small polarons on the TiO_2(110) surface, J. Appl. Phys. 119 (2016) 181503.
[198] A. Argondizzo, S. Tan, H. Petek, Resonant two-photon photoemission from Ti3d defect states of TiO_2 (110) revisited, J. Phys. Chem. C 120 (2016) 12959–12966.
[199] C.D. Valentin, G. Pacchioni, A. Selloni, Electronic structure of defect states in hydroxylated and reduced rutile TiO_2(110) surfaces, Phys. Rev. Lett. 97 (2006) 166803.
[200] N.A. Deskins, R. Rousseau, M. Dupuis, Localized electronic states from surface hydroxyls and polarons in TiO_2(110), J. Phys. Chem. C 113 (2009) 14583–14586.
[201] S.L. Dudarev, G.A. Botton, S.Y. Savrasov, C.J. Humphreys, A.P. Sutton, Electron-energy-loss spectra and the structural stability of nickel oxide: an LSDA + U study, Phys. Rev. B 57 (1998) 1505–1509.
[202] E. Canadell, M.H. Whangbo, Conceptual aspects of structure–property correlations and electronic instabilities, with applications to low-dimensional transition-metal oxides, Chem. Rev. 91 (1991) 965–1034.
[203] P.M. Kowalski, M.F. Camellone, N.N. Nair, B. Meyer, D. Marx, Charge localization dynamics induced by oxygen vacancies on the TiO_2(110) surface, Phys. Rev. Lett. 105 (2010) 146405.
[204] S.K. Wallace, K.P. Mckenna, Facet-dependent electron trapping in TiO_2 nanocrystals, J. Phys. Chem. C 119 (2015) 1913–1920.
[205] Y. Nakaoka, Y. Nosada, ESR investigation into the effects of heat treatment and crystal structure on radicals produced over irradiated TiO_2 powder, J. Photochem. Photobiol. A: Chem. 110 (1997) 299–305.
[206] C.D. Valentin, A. Selloni, Bulk and surface polarons in photoexcited anatase TiO_2, J. Phys. Chem. Lett. 2 (2011) 2223–2228.
[207] S.A. Shevlin, S.M. Woodley, Electronic and optical properties of doped and undoped $(TiO_2)_n$ nanoparticles, J. Phys. Chem. C 114 (2010) 17333–17343.
[208] U. Martinez, L.B. Vilhelmsen, H.H. Kristoffersen, J. Stausholm-Møller, B. Hammer, Steps on rutile TiO_2 (110): active sites for water and methanol dissociation, Phys. Rev. B 84 (2011) 205434.
[209] I. Dawson, P.D. Bristowe, First-principles study of a tilt grain boundary in rutile, Phys. Rev. B 54 (1996) 13727–13733.
[210] D. Lee, Y. Kanai, Y.J. Am, Role of four-fold coordinated titanium and quantum confinement in CO_2 reduction at titania surface, Chem. Soc. 134 (2012) 20266–20269.
[211] M. Posternak, A. Baldereschi, B. Delley, Dissociation of water on anatase TiO_2 nanoparticles: the role of undercoordinated Ti atoms at edges, J. Phys. Chem. C 113 (2009) 15862–15867.
[212] M. Nolan, A. Iwaszuk, K.A. Gray, Localization of photoexcited electrons and holes on low coordinated Ti and O sites in free and supported TiO_2 nanoclusters, J. Phys. Chem. C 118 (2014) 27890–27900.
[213] A. Iwaszuk, M. Nolan, Reactivity of sub 1 nm supported clusters: $(TiO_2)_n$ clusters supported on rutile TiO_2(110), Phys. Chem. Chem. Phys. 13 (2011) 4963–4973.
[214] A. Iwaszuk, P.A. Mulheran, M. Nolan, TiO_2 nanocluster modified-rutile TiO_2 photocatalyst: a first principles investigation, J. Mater. Chem. A 1 (2013) 2515–2525.
[215] S. Auvinen, M. Lahti, M. Alatalo, Unoccupied titanium 3d states due to subcluster formation in stoichiometric TiO_2 nanoparticles, Int. J. Quantum Chem. 115 (2015) 1175–1180.
[216] M. Nolan, N.A. Deskins, K.C. Schwartzenberg, K.A. Gray, Local interfacial structure influences charge localization in titania composites: beyond the band alignment paradigm, J. Phys. Chem. C 120 (2016) 1808–1815.
[217] J.C. Garcia, M. Nolan, N.A. Deskins, The nature of interfaces and charge trapping sites in photocatalytic mixed-phase TiO_2 from first principles modeling, J. Chem. Phys. 142 (2015) 024708.
[218] N.Q. Le, I.V. Schweigert, Modeling electronic trap states at interfaces between anatase nanoparticles, J. Phys. Chem. C 121 (2017) 14254–14260.
[219] A. Tilocca, A. Selloni, DFT-GGA and DFT + U simulations of thin water layers on reduced TiO_2 anatase, J. Phys. Chem. C 116 (2012) 9114–9121.
[220] S. Selcuk, A. Selloni, Facet-dependent trapping and dynamics of excess electrons at anatase TiO_2 surfaces and aqueous interfaces, Nat. Mater. 15 (2016) 1103–1107.
[221] M. Sumita, C. Hu, Y. Tateyama, Interface water on TiO_2 anatase (101) and (001) surfaces: first-principles study with TiO_2 slabs dipped in bulk water, J. Phys. Chem. C 114 (2010) 18529–18537.
[222] C.R. Parrinello, Unified approach for molecular dynamics and density-functional theory, Phys. Rev. Lett. 55 (1985) 2471–2474.
[223] N. Wu, J. Wang, D.N. Tafen, H. Wang, J.-G. Zheng, J.P. Lewis, X. Liu, S.S. Leonard, A. Manivannan, Shape-enhanced photocatalytic activity of single-crystalline anatase TiO_2 (101) nanobelts, J. Am. Chem. Soc. 132 (2010) 6679–6685.
[224] J. Yu, J. Low, W. Xiao, P. Zhou, M. Jaroniec, Enhanced photocatalytic CO_2-reduction activity of anatase TiO_2 by coexposed {001} and {101} facets, J. Am. Chem. Soc. 136 (2014) 8839–8842.
[225] T. Ohno, K. Sarukawa, M. Matsumura, Crystal faces of rutile and anatase TiO_2 particles and their roles in photocatalytic reactions, New J. Chem. 26 (2002) 1167–1170.
[226] J. Cheng, J.V. Vondele, M. Sprik, Identifying trapped electronic holes at the aqueous TiO_2 interface, J. Phys. Chem. C 118 (2014) 5437–5444.
[227] N.A. Deskins, M. Dupuis, Intrinsic hole migration rates in TiO_2 from density functional theory, J. Phys. Chem. C 113 (2009) 346–358.
[228] T. Shibuya, K. Yasuoka, S. Mirbt, B. Sanyal, Bipolaron formation induced by oxygen vacancy at rutile TiO_2 (110) surfaces, J. Phys. Chem. C 118 (2014) 9429–9435.

[229] M.A. Henderson, W.S. Epling, C.H.F. Peden, C.L. Perkins, Insights into photoexcited electron scavenging processes on TiO_2 obtained from studies of the reaction of O_2 with OH groups adsorbed at electronic defects on TiO_2 (110), J. Phys. Chem. B 107 (2003) 534–545.
[230] B.J. Morgan, G.W. Watson, Polaronic trapping of electrons and holes by native defects in anatase TiO_2, Phys. Rev. B 80 (2009) 233102.
[231] E. Finazzi, C.D. Valentin, G. Pacchioni, Nature of Ti interstitials in reduced bulk anatase and rutile TiO_2, J. Phys. Chem. C 113 (2009) 3382–3385.
[232] P. Le Fèvre, J. Danger, H. Magnan, D. Chandesris, J. Jupille, S. Bourgeois, M.-A. Arrio, R. Gotter, A. Verdini, A. Morgante, Stoichiometry-related auger lineshapes in titanium oxides: influence of valence-band profile and of Coster–Kronig processes, Phys. Rev. B 69 (2004) 155421.
[233] P. Krüger, S. Bourgeois, B. Domenichini, H. Magnan, D. Chandesris, P. Le Fèvre, A.M. Flank, J. Jupille, L. Floreano, A. Cossaro, A. Verdini, A. Morgante, Defect states at the TiO_2(110) surface probed by resonant photoelectron diffraction, Phys. Rev. Lett. 100 (2008) 055501.
[234] P. Krüger, J. Jupille, S. Bourgeois, B. Domenichini, A. Verdini, L. Floreano, A. Morgante, Intrinsic nature of the excess electron distribution at the TiO_2 (110) surface, Phys. Rev. Lett. 108 (2012) 126803.
[235] C. Wang, N. Zhang, Q. Li, Y. Yu, J. Zhang, Y. Li, H. Wang, Dielectric relaxations in rutile TiO_2, J. Am. Ceram. Soc. 98 (2015) 148–153.
[236] J. Jaćimović, C. Vaju, A. Magrez, H. Berger, L. Forró, R. Gaál, V. Cerovski, R. Žikić, Pressure dependence of the large-polaron transport in anatase TiO_2 single crystals, Eur. Phys. Lett. 99 (2012) 57005.
[237] M. Setvin, C. Franchini, X. Hao, M. Schmid, A. Janotti, M. Kaltak, C.G.V. Walle, G. Kresse, U. Diebold, Direct view at excess electrons in TiO_2 rutile and anatase, Phys. Rev. Lett. 113 (2014) 086402.
[238] S. Moser, L. Moreschini, J. Jaćimović, O.S. Barišić, H. Berger, A. Magrez, Y.J. Chang, K.S. Kim, A. Bostwick, E. Rotenberg, L. Forró, M. Grioni, Tunable polaronic conduction in anatase TiO_2, Phys. Rev. Lett. 110 (2013) 196403.
[239] H. Fröhlich, Electrons in lattice fields, Adv. Phys. 3 (1954) 325–361.
[240] M. Setvin, X. Hao, B. Daniel, J. Pavelec, Z. Novotny, G.S. Parkinson, M. Schmid, G. Kresse, C. Franchini, U. Diebold, Charge trapping at the step edges of TiO_2 anatase (101), Angew. Chem. Int. Ed. 53 (2014) 4714–4716.
[241] X. Gong, A. Selloni, M. Batzill, U. Diebold, Steps on anatase TiO_2 (101), Nat. Mater. 5 (2006) 665–670.
[242] C.M. Yim, M.B. Watkins, M.J. Wolf, C.L. Pang, K. Hermansson, G. Thornton, Engineering polarons at a metal oxide surface, Phys. Rev. Lett. 117 (2016) 116402.
[243] F. Zuo, L. Wang, T. Wu, Z. Zhang, D. Borchardt, P. Feng, Self-doped Ti^{3+} enhanced photocatalyst for hydrogen production under visible light, J. Am. Chem. Soc. 132 (2010) 11856–11857.
[244] Y. Zhou, C. Cheng, N. Wang, Y. Li, H. Ding, Stable Ti^{3+} self-doped anatase-rutile mixed TiO_2 with enhanced visible light utilization and durability, J. Phys. Chem. C 120 (2016) 6116–6124.
[245] C. Mao, F. Zuo, Y. Hou, X. Bu, P. Feng, In situ preparation of a Ti^{3+} self-doped TiO_2 film with enhanced activity as photoanode by N_2H_4 reduction, Angew. Chem. Int. Ed. 126 (2014) 10653–10657.
[246] S. Yang, A.T. Brant, N.C. Giles, L.E. Halliburton, Intrinsic small polarons in rutile TiO_2, Phys. Rev. B 87 (2013) 125201.
[247] Z. Wang, B. Wen, Q. Hao, L. Liu, C. Zhou, X. Mao, X. Lang, W. Yin, D. Dai, A. Selloni, X. Yang, Localized excitation of Ti^{3+} ions in the photo absorption and photocatalytic activity of reduced rutile TiO_2, J. Am. Chem. Soc. 137 (2015) 9146–9152.
[248] P. Zawadzki, Absorption spectra of trapped holes in anatase TiO_2, J. Phys. Chem. C 117 (2013) 8647–8651.
[249] M. Watanabe, T. Hayashi, Time-resolved study of self-trapped exciton luminescence in anatase TiO_2 under two-photon excitation, J. Lumin. 112 (2005) 88–91.
[250] M. Watanabe, S. Sasaki, T. Hayashi, Time-resolved study of photoluminescence in anatase TiO_2, J. Lumin. 87–89 (2000) 1234–1236.
[251] M. Gallart, T. Cottineau, B. Hönerlage, V. Keller, N. Keller, P. Gilliot, Temperature dependent photoluminescence of anatase and rutile TiO_2 single crystals: polaron and self-trapped exciton formation, J. Appl. Phys. 124 (2018) 133104.
[252] N. Hosaka, T. Sekiya, S. Kurita, Excitonic state in anatase TiO_2 single crystal, J. Lumin. 72–74 (1997) 874–875.
[253] G. Fazio, L. Ferrighi, C.D. Valentin, Spherical versus faceted anatase TiO_2 nanoparticles: a model study of structural and electronic properties, J. Phys. Chem. C 119 (2015) 20735–20746.
[254] B. Astinchap, R. Moradian, K. Gholami, Effect of sputtering power on optical properties of prepared TiO_2 thins films by thermal oxidation of sputtered Ti layers, Mater. Sci. Semicond. Process. 63 (2017) 169–175.
[255] M.M. Khan, S.A. Ansari, D. Pradhan, M.O. Ansari, D.H. Han, J. Lee, M.H. Cho, Band gap engineered TiO_2 nanoparticles for visible light induced photoelectrochemical and photocatalytic studies, J. Mater. Chem. A 2 (2014) 637–644.
[256] F. Bensouici, M. Bououdina, A.A. Dakhel, R. Tala-Ighil, M. Tounane, A. Iratni, T. Souier, S. Liu, W. Cai, Optical, structural and photocatalysis properties of Cu-doped TiO_2 thin films, Appl. Surf. Sci. 395 (2017) 110–116.
[257] J.A. Anta, V. Morales-Flórez, Combined effect of energetic and spatial disorder on the trap-limited electron diffusion coefficient of metal-oxide nanostructures, J. Phys. Chem. C 112 (2008) 10287–10293.
[258] J. Nelson, R.E. Chandler, Random walk models of charge transfer and transport in dye sensitized systems, Coord. Chem. Rev. 248 (2004) 1181–1194.
[259] M. Ansari-Rad, J.A. Anta, J. Bisquert, Interpretation of diffusion and recombination in nanostructured and energy-disordered materials by stochastic quasi-equilibrium simulation, J. Phys. Chem. C 117 (2013) 16275–16289.
[260] J.A. Anta, Random walk numerical simulation for solar cell applications, Energy Environ. Sci. 2 (2009) 387–392.
[261] H. Gerischer, A. Heller, Photocatalytic oxidation of organic molecules at TiO_2 particles by sunlight in aerated water, J. Electrochem. Soc. 139 (1992) 113–118.
[262] H. Tang, K. Prasad, R. Sanjines, P.E. Schmid, F. Levy, Electrical and optical properties of TiO_2 anatase thin films, J. Appl. Phys. 75 (1994) 2042–2047.
[263] F. Nunzi, E. Mosconi, L. Storchi, E. Ronca, A. Selloni, M. Grätzele, F.D. Angelis, Inherent electronic trap states in TiO_2 nanocrystals: effect of saturation and sintering, Energy Environ. Sci. 6 (2013) 1221–1229.
[264] C. Richter, C.A. Schmuttenmaer, Exciton-like trap states limit electron mobility in TiO_2 nanotubes, Nat. Nanotechnol. 5 (2010) 769–772.
[265] X. Chen, L. Liu, P.Y. Yu, S.S. Mao, Increasing solar absorption for photocatalysis with black hydrogenated titanium dioxide nanocrystals, Science 331 (2011) 746–750.
[266] R.A. Streeat, Cambridge University Press, Cambridge, UK, 1991, p. 118.
[267] L. Bertoluzzi, J. Bisquert, Equivalent circuit of electrons and holes in thin semiconductor films for photoelectrochemical water splitting applications, J. Phys. Chem. Lett. 3 (2012) 2517–2522.
[268] L. Bertoluzzi, L. Badia-Bou, F. Fabregat-Santiago, S. Gimenez, J. Bisquert, Interpretation of cyclic voltammetry measurements of thin semiconductor films for solar fuel applications, J. Phys. Chem. Lett. 4 (2013) 1334–1339.
[269] J. Bisquert, A. Zaban, P. Salvador, Analysis of the mechanisms of electron recombination in nanoporous TiO_2 dye-sensitized solar cells: nonequilibrium steady-state statistics and interfacial electron transfer via surface states, J. Phys. Chem. B 106 (2002) 8774–8782.
[270] J. van de Lagemaat, A.J. Frank, Nonthermalized electron transport in dye-sensitized nanocrystalline TiO_2 films: transient photocurrent and random-walk modeling studies, J. Phys. Chem. B 105 (2001) 11194–11205.
[271] J.A. Anta, J. Nelson, N. Quirke, Charge transport model for disordered materials: application to sensitized TiO_2, Phys. Rev. B 65 (2002) 125324.
[272] J.A. Anta, F. Casanueva, G. Oskam, A numerical model for charge transport and recombination in dye-sensitized solar cells, J. Phys. Chem. B 110 (2006) 5372–5378.
[273] Q. Wang, S. Ito, M. Grätzel, F. Fabregat-Santiago, I. Mora-Seró, J. Bisquert, T. Bessho, H. Imai, Characteristics of high efficiency dye-sensitized solar cells, J. Phys. Chem. B 110 (2006) 25210–25221.
[274] S. Krischok, J. Günster, D.W. Goodman, O. Höfft, V. Kempter, MIES and UPS(HeI) studies on reduced TiO_2(110), Surf. Interface Anal. 37 (2005) 77–82.
[275] P. Reckers, M. Dimamay, J. Klett, S. Trost, K. Zilberberg, T. Riedl, B.A. Parkinson, J. Brötz, W. Jaegermann, T. Mayer, Deep and shallow TiO_2 gap states on cleaved anatase single crystal (101) surfaces, nanocrystalline anatase films, and ALD titania ante and post annealing, J. Phys. Chem. C 119 (2015) 9890–9898.
[276] T. Berger, D. Monllor-Satoca, M. Jankulovska, T. Lana-Villarreal, R. Gómez, The electrochemistry of nanostructured titanium dioxide electrodes, ChemPhysChem 13 (2012) 2824–2875.
[277] F. Fabregat-Santiago, I. Mora-Seró, G. Garcia-Belmonte, J. Bisquert, Cyclic voltammetry studies of nanoporous semiconductors. Capacitive and reactive properties of nanocrystalline TiO_2 electrodes in aqueous electrolyte, J. Phys. Chem. B 107 (2003) 758–768.
[278] Bisquert, F. Fabregat-Santiago, I. Mora-Seró, G. Garcia-Belmonte, E.M. Barea, E. Palomares, A review of recent results on electrochemical determination of the density of electronic states of nanostructured metal-oxide semiconductors and organic hole conductors, Inorg. Chim. Acta 361 (2008) 684–698.
[279] M. Jankulovska, T. Berger, T. Lana-Villarreal, R. Gómez, A comparison of quantum-sized anatase and rutile nanowire thin films: devising differences in the electronic structure from photoelectrochemical measurements, Electrochim. Acta 62 (2012) 172–180.
[280] T. Berger, J.A. Anta, V. Morales-Flrez, Electrons in the band gap: spectroscopic characterization of anatase TiO_2 nanocrystal electrodes under Fermi level control, J. Phys. Chem. C 116 (2012) 11444–11455.
[281] J. Bisquert, Chemical capacitance of nanostructured semiconductors: its origin and significance for nanocomposite solar cells, Phys. Chem. Chem. Phys. 5 (2003) 5360–5364.
[282] T. Berger, T. Lana-Villarreal, D. Monllor-Satoca, R. Gmez, An electrochemical study on the nature of trap states in nanocrystalline rutile thin films, J. Phys. Chem. C 111 (2007) 9936–9942.
[283] M. Jankulovska, T. Berger, S.S. Wong, R. Gmez, T. Lana-Villarreal, Trap states in TiO_2 films made of nanowires, nanotubes or nanoparticles: an electrochemical study, ChemPhysChem 13 (2012) 3008–3017.
[284] F. Fabregat-Santiago, E.M. Barea, J. Bisquert, G.K. Mor, K. Shankar, C.A. Grimes, High carrier density and capacitance in TiO_2 nanotube arrays induced by electrochemical doping, J. Am. Chem. Soc. 130 (2008) 11312–11316.
[285] Q. Zhang, V. Celorrio, K. Bradley, F. Eisner, D. Cherns, D.J. Wei Yan, Fermín density of deep trap states in oriented TiO_2 nanotube arrays, J. Phys. Chem. C 118 (2014) 18207–18213.

[286] M. Zare, A. Mortezaal, A. Shafiekhani, Photoelectrochemical determination of shallow and deep trap states of platinum-decorated TiO_2 nanotube arrays for photocatalytic applications, J. Phys. Chem. C 120 (2016) 9017–9027.
[287] B. Liu, J. Wang, J. Yang, X. Zhao, Charge carrier interfacial transfer pathways from TiO_2 and Au/TiO_2 nanorod arrays to electrolyte and the association with photocatalysis, Appl. Surf. Sci. 464 (2019) 367–375.
[288] F. Su, T. Wang, R. Lv, J. Zhang, P. Zhang, J. Lu, J. Gong, Dendritic Au/TiO_2 nanorod arrays for visible-light driven photoelectrochemical water splitting, Nanoscale 5 (2013) 9001–9009.
[289] L. Li, X.C. Zeng, Direct simulation evidence of generation of oxygen vacancies at the golden cage Au_{16} and TiO_2 (110) interface for CO oxidation, J. Am. Chem. Soc. 136 (2014) 15857–15860.
[290] Y. Maeda, Y. Iizuka, M. Kohyama, Generation of oxygen vacancies at an Au/TiO_2 perimeter interface, J. Am. Chem. Soc. 135 (2013) 906–909.
[291] H. Wang, J. He, G. Boschloo, H. Lindstrolm, A. Hagfeldt, S. Lindquist, Electrochemical investigation of traps in a nanostructured TiO_2 film, J. Phys. Chem. B 105 (2001) 2529–2533.
[292] G. Schlichthörl, S.Y. Huang, J. Sprague, A.J. Frank, Band edge movement and recombination kinetics in dye-sensitized nanocrystalline TiO_2 solar cells: a study by intensity modulated photovoltage spectroscopy, J. Phys. Chem. B 101 (1997) 8141–8155.
[293] P.E. de Jongh, D. Vanmaekelbergh, Investigation of the electronic transport properties of nanocrystalline particulate TiO_2 electrodes by intensity-modulated photocurrent spectroscopy, J. Phys. Chem. B 101 (1997) 2716–2722.
[294] A. Sacco, Electrochemical impedance spectroscopy: fundamentals and application in dye-sensitized solar cells, Renew. Sustain. Energy Rev. 79 (2017) 814–829.
[295] L. Bertoluzzi, I. Herraiz-Cardona, R. Gottensmann, A. Zaban, J. Bisquert, Relaxation of electron carriers in the density of states of nanocrystalline TiO_2, J. Phys. Chem. Lett. 5 (2014) 689–694.
[296] F. Cao, G. Oskam, P.C. Searson, J.M. Stipkala, T.A. Heimer, F. Farzad, G.J. Meyer, Electrical and optical properties of porous nanocrystalline TiO_2 films, J. Phys. Chem. 99 (1995) 11974–11980.
[297] D.-D. Qin, Y.-P. Bi, X.-J. Feng, W. Wan, G.D. Barbe, T. Wang, Y.-M. Song, X.-Q. Lu, T.E. Mallouk, Hydrothermal growth and photoelectrochemistry of highly oriented, crystalline anatase TiO_2 nanorods on transparent conducting electrodes, Chem. Mater. 27 (2015) 4180–4183.
[298] D. Mandal, T.W. Hamann, Charge distribution in nanostructured TiO_2 photoanode determined by quantitative analysis of the band edge unpinning, ACS Appl. Mater. Interfaces 8 (2016) 419–424.
[299] S. Takata, Y. Miura, Y. Matsumoto, Evidence for the intrinsic nature of band-gap states electrochemically observed on atomically flat TiO_2(110) surfaces, Phys. Chem. Chem. Phys. 16 (2014) 24784–24789.
[300] A. Kafizas, X. Wang, S.R. Pendlebury, P. Barnes, M. Ling, C.S. Vazquez, R. Quesada-Cabrera, C. Li, I.P. Parkin, J.R. Durrant, Where do photogenerated holes go in anatase:rutile TiO_2? A transient absorption spectroscopy study of charge transfer and lifetime, J. Phys. Chem. A 120 (2016) 715–723.
[301] D. Bahnemann, A. Henglein, J. Lilie, L. Spanhel, Flash photolysis observation of the absorption spectra of trapped positive holes and electrons in colloidal TiO_2, J. Phys. Chem. 88 (1984) 709–711.
[302] Me. Hu, Y. Cao, Z. Li, S. Yang, Z. Xing, Ti^{3+} self-doped mesoporous black TiO_2/SiO_2 nanocomposite as remarkable visible light photocatalyst, Appl. Surf. Sci. 426 (2017) 734–744.
[303] J. Pan, Z. Dong, B. Wang, Z. Jiang, C. Zhao, J. Wang, C. Song, Y. Zheng, C. Li, The enhancement of photocatalytic hydrogen production via Ti^{3+} self-doping black TiO_2/g-C_3N_4 hollow core–shell nano-heterojunction, Appl. Catal. B: Environ. 242 (2019) 92–99.
[304] J. Lee, Z. Li, L. Zhu, S. Xie, X. Cui, Ti^{3+} self-doped TiO_2 via facile catalytic reduction over $Al(acac)_3$ with enhanced photoelectrochemical and photocatalytic activities, Appl. Catal. B: Environ. 224 (2018) 715–724.
[305] S.H. Szczepankiewicz, J.A. Moss, M.R. Hoffmann, Electron traps and the stark effect on hydroxylated titania photocatalysts, J. Phys. Chem. B 106 (2002) 7654–7658.
[306] N.A. Deskins, R. Rousseau, M. Dupuis, Distribution of Ti^{3+} surface sites in reduced TiO_2, J. Phys. Chem. C 115 (2011) 7562–7572.
[307] T. Berger, T. Lana-Villarreal, D. Monllor-Satoca, R. Gómez, Charge transfer reductive doping of nanostructured TiO_2 thin films as a way to improve their photoelectrocatalytic performance, Electrochem. Commun. 8 (2006) 1713–1718.
[308] G. Boschloo, D. Fitzmaurice, Spectroelectrochemical investigation of surface states in nanostructured TiO_2 electrodes, J. Phys. Chem. B 103 (1999) 2228–2231.
[309] A. Yamakata, T. Ishibashi, H. Onishi, Electron- and hole-capture reactions on Pt/TiO_2 photocatalyst exposed to methanol vapor studied with time-resolved infrared absorption spectroscopy, J. Phys. Chem. B 106 (2002) 9122–9125.
[310] A. Yamakata, T. Ishibashi, H. Onishi, Time-resolved infrared absorption spectroscopy of photogenerated electrons in platinized TiO_2 particles, Chem. Phys. Lett. 333 (2001) 271–277.
[311] G. Boschloo, A. Hagfeldt, Activation energy of electron transport in dye-sensitized TiO_2 solar cells, J. Phys. Chem. B 109 (2005) 12093–12098.
[312] D.M. Savory, A.J. McQuillan, Influence of formate adsorption and protons on shallow trap infrared absorption (STIRA) of anatase TiO_2 during photocatalysis, J. Phys. Chem. C 117 (2013) 23645–23656.
[313] D.M. Savory, A.J. McQuillan, IR spectroscopic behavior of polaronic trapped electrons in TiO_2 under aqueous photocatalytic conditions, J. Phys. Chem. C 118 (2014) 13680–13692.
[314] A. Yamakata, J.J.M. Vequizo, H. Matsunaga, Distinctive behavior of photogenerated electrons and holes in anatase rutile TiO_2 powders, J. Phys. Chem. C 119 (2015) 24538–24545.
[315] A. Yamakata, J.J.M. Vequizo, M. Kawaguchi, Behavior and energy state of photogenerated charge carriers in single-crystalline and polycrystalline powder $SrTiO_3$ studied by time-resolved absorption spectroscopy in the visible to mid-infrared region, J. Phys. Chem. C 119 (2015) 1880–1885.
[316] J.J.M. Vequizo, H. Matsunaga, T. Ishiku, S. Kamimura, T. Ohno, A. Yamakata, Trapping-induced enhancement of photocatalytic activity on brookite TiO_2 powders: comparison with anatase and rutile TiO_2 powders, ACS Catal. 7 (2017) 2644–2651.
[317] T. Yoshihara, R. Katoh, A. Furube, Y. Tamaki, M. Murai, K. Hara, S. Murata, H. Arakawa, M. Tachiya, Identification of reactive species in photoexcited nanocrystalline TiO_2 films by wide-wavelength-range (400–2500 nm) transient absorption spectroscopy, J. Phys. Chem. B 108 (2004) 3817–3823.
[318] H. Zhang, M. Zhou, Q. Fu, B. Lei, W. Lin, H. Guo, M. Wu, Y. Lei, Observation of defect state in highly ordered titanium dioxide nanotube arrays, Nanotechnology 25 (2014) 275603.
[319] F.J. Knorr, D. Zhang, J.L. McHale, Influence of $TiCl_4$ treatment on surface defect photoluminescence in pure and mixed-phase nanocrystalline TiO_2, Langmuir 23 (2007) 8686–8690.
[320] D.K. Pallotti, L. Passoni, P. Maddalena, F. Di Fonzo, S. Lettieri, Photoluminescence mechanisms in anatase and rutile TiO_2, J. Phys. Chem. C 121 (2017) 9011–9021.
[321] R.E. Rex, Y. Yang, F.J. Knorr, J.Z. Zhang, Y. Li, J.L. McHale, Spectroelectrochemical photoluminescence of trap states in H-treated rutile TiO_2 nanowires: implications for photooxidation of water, J. Phys. Chem. C 120 (2016) 3530–3541.
[322] F.J. Knorr, C.C. Mercado, J.L. McHale, Trap-state distributions and carrier transport in pure and mixed-phase TiO_2: influence of contacting solvent and interphasial electron transfer, J. Phys. Chem. C 112 (2008) 12786–12794.
[323] R. Nakamura, T. Okamura, N. Ohashi, A. Imanishi, Y. Nakato, Molecular mechanisms of photoinduced oxygen evolution, PL emission, and surface roughening at atomically smooth (110) and (100) n-TiO_2 (rutile) surfaces in aqueous acidic solutions, J. Am. Chem. Soc. 127 (2005) 12975–12983.
[324] C.C. Mercado, F.J. Knorr, J.L. McHale, S.M. Usmani, A.S. Ichimura, L.V. Saraf, Location of hole and electron traps on nanocrystalline anatase TiO_2, J. Phys. Chem. C 116 (2012) 10796–10804.
[325] F.J. Knorr, J.L. McHale, Spectroelectrochemical photoluminescence of trap states of nanocrystalline TiO_2 in aqueous media, J. Phys. Chem. C 117 (2013) 13654–13662.
[326] G. Boschloo, D. Fitzmaurice, Spectroelectrochemistry of highly doped nanostructured tin dioxide electrodes, J. Phys. Chem. B 103 (1999) 7860–7868.
[327] C. Kritayakornupong, K. Plankensteiner, B.M.T. Rode, The Jahn–Teller effect of the Ti-III ion in aqueous solution: extented ab initio QM/MM molecular dynamics simulations, ChemPhysChem 5 (2004) 1499–1506.
[328] P.R.F. Barnes, A.Y. Anderson, M. Juozapavicius, L. Liu, X. Li, E. Palomares, A. Forneli, B.C. O'Regan, Factors controlling charge recombination under dark and light conditions in dye sensitised solar cells, Phys. Chem. Chem. Phys. 13 (2011) 3547–3558.
[329] R.E. Rex, F.J. Knorr, J.L. McHale, Surface traps of TiO_2 nanosheets and nanoparticles as illuminated by spectroelectrochemical photoluminescence, J. Phys. Chem. C 118 (2014) 16831–16841.
[330] N. Murakami, Y. Kurihara, T. Tsubota, T. Ohno, Shape-controlled anatase titanium (IV) oxide particles prepared by hydrothermal treatment of peroxo titanic acid in the presence of polyvinyl alcohol, J. Phys. Chem. C 113 (2009) 3062–3069.
[331] T. Tachikawa, S. Yamashita, T. Majima, Evidence for crystal-face-dependent TiO_2 photocatalysis from single-molecule imaging and kinetic analysis, J. Am. Chem. Soc. 133 (2011) 7197–7204.
[332] R.E. Rex, F.J. Knorr, J.L. McHale, Imaging luminescent traps on single anatase TiO_2 crystals: the influence of surface capping on phoroluminescence charge transport, J. Phys. Chem. C 119 (2015) 26212–26218.
[333] H.G. Yang, C.H. Sun, S.Z. Qiao, J. Zou, G. Liu, S.C. Smith, H.M. Cheng, G.Q. Lu, Anatase TiO_2 single crystals with a large percentage of reactive facets, Nature 453 (2008) 638–641.
[334] C. Wehrenfennig, C.M. Palumbiny, H.J. Snaith, M.B. Johnston, L. Schmidt-Mende, L.M. Herz, Fast charge-carrier trapping in TiO_2 nanotubes, J. Phys. Chem. C 119 (2015) 9159–9168.
[335] Z. Pei, S. Weng, P. Liu, Enhanced photocatalytic activity by bulk trapping and spatial separation of charge carriers: a case study of defect and facet mediated TiO_2, Appl. Catal. B: Environ. 180 (2016) 463–470.
[336] Y. Yu, X. Yang, Y. Zhao, X. Zhang, L. An, M. Huang, G. Chen, R. Zhang, Engineering the band gap states of the rutile TiO_2(110) surface by modulating the active heteroatom, Angew. Chem. Int. Ed. 130 (2018) 8686–8690.
[337] Y. Tamaki, A. Furube, M. Murai, K. Hara, R. Katoh, M. Tachiya, Dynamics of efficient electron-hole separation in TiO_2 nanoparticles revealed by femtosecond transient absorption spectroscopy under the weak-excitation condition, Phys. Chem. Chem. Phys. 9 (2007) 1453–1460.
[338] Y. Tamaki, K. Hara, R. Katoh, M. Tachiya, A. Furube, Femtosecond visible-to-IR spectroscopy of TiO_2 nanocrystalline films: elucidation of the

electron mobility before deep trapping, J. Phys. Chem. C 113 (2009) 11741–11746.
[339] J.L. Peter, D.J. Vinyard, G.W. Brudvig, J.M. Mayer, Slow equilibration between spectroscopically distinct trap states in reduced TiO_2 nanoparticles, J. Am. Chem. Soc. 139 (2017) 2868–2871.
[340] K. Shirai, T. Sugimoto, K. Watanabe, M. Haruta, H. Kurata, Y. Matsumoto, Effect of water adsorption on carrier trapping dynamics at the surface of anatase TiO_2 nanoparticles, Nano Lett. 16 (2016) 1323–1327.
[341] M.C. Fravventura, L.D.A. Siebbeles, T.J. Savenije, Mechanisms of photogeneration and relaxation of excitons and mobile carriers in anatase TiO_2, J. Phys. Chem. C 118 (2014) 7337–7343.
[342] B. Liu, J. Yang, X. Zhao, J. Yu, Role of electron interfacial transfer in mesoporous nano-TiO_2 photocatalysis: a combined study of in-situ photoconductivity and kinetic simulation, Phys. Chem. Chem. Phys. 19 (2017) 8866–8873.
[343] B. Liu, R. Zhang, Effects of geometrical topology and electron fermi-level gradient on the photocatalytic efficiency in semiconductor nano-particulate photocatalysis, Phys. Chem. Chem. Phys. 19 (2017) 10116–10124.
[344] D. Vanmaekelbergh, P.E. de Jongh, Driving force for electron transport in porous nanostructured photoelectrodes, J. Phys. Chem. B 103 (1999) 747–750.
[345] J. Bisquert, Chemical diffusion coefficient of electrons in nanostructured semiconductor electrodes and dye-sensitized solar cells, J. Phys. Chem. B 108 (2004) 2323–2332.
[346] B. van de Zanden, A. Goossens, The nature of electron migration in dye-sensitized nanostructured TiO_2, J. Phys. Chem. B 104 (2000) 7171–7178.
[347] J. Bisquert, Hopping transport of electrons in dye-sensitized solar cells, J. Phys. Chem. C 111 (2017) 17163–17168.
[348] J. Nelson, S.A. Haque, D.R. Klug, J.R. Durrant, Trap-limited recombination in dye-sensitized nanocrystalline metal oxide electrodes, Phys. Rev. B 63 (2001) 797–801.
[349] B. O'Regan, M. Grätzel, A low-cost, high-efficiency solar cell based on dye-sensitized colloidal TiO_2 films, Nature 353 (1991) 737–740.
[350] H.J. Mandujano-Ramírez, J.P. González-Vázquez, G. Oskam, T. Dittrich, G. Garcia-Belmonte, I. Mora-Seró, J. Bisquert, J.A. Anta, Charge separation at disordered semiconductor heterojunctions from random walk numerical simulations, Phys. Chem. Chem. Phys. 16 (2014) 4082–4091.
[351] J. Nelson, Continuous-time random-walk model of electron transport in nanocrystalline TiO_2 electrodes, Phys. Rev. B 59 (1999) 15374.
[352] B. Liu, X. Zhao, J. Yu, A. Fujishima, K. Nakata, A stochastic study of electron transfer kinetics in nano-particulate photocatalysis: a comparison of the quasi-equilibrium approximation with a random walking model, Phys. Chem. Chem. Phys. 18 (2016) 31914–31923.
[353] A.V. Barzykin, M. Tachiya, Mechanism of charge recombination in dye-sensitized nanocrystalline semiconductors: random flight model, J. Phys. Chem. B 106 (2002) 4356–4363.
[354] S.A. Haque, Y. Tachibana, R.L. Willis, J.E. Moser, M. Graetzel, D.R. Klug, J.R. Durrant, Parameters influencing charge recombination kinetics in dye-sensitized nanocrystalline titanium dioxide films, J. Phys. Chem. B 104 (2000) 538–547.
[355] P.E. de Jongh, D. Vanmaekelbergh, Trap-limited electronic transport in assemblies of nanometer-size TiO_2 particles, Phys. Rev. Lett. 77 (1996) 3427–3430.
[356] H. Chen, Z. Wei, K. Yan, Y. Bai, S. Yang, H. Chen, Z. Wei, Unveiling two electron-transport modes in oxygen-deficient TiO_2 nanowires and their influence on photoelectrochemical operation, J. Phys. Chem. Lett. 5 (2014) 2890–2896.
[357] J. Zheng, L. Mo, W. Chen, L. Jiang, Y. Ding, Z. Li, L. Hu, S. Dai, Surface states in TiO_2 submicrosphere films and their effect on electron transport, Nano Res. 10 (2017) 3671–3679.
[358] J. Villanueva-Cab, S.-R. Jang, A.F. Halverson, K. Zhu, Ar.J. Frank, Trap-free transport in ordered and disordered TiO_2 nanostructures, Nano Lett. 14 (2014) 2305–2309.
[359] A. Petrozza, C. Groves, H. Snaith, Electron transport and recombination in dye-sensitized mesoporous TiO_2 probed by photoinduced charge conductivity modulation spectroscopy with Monet-Carlo modelling, J. Am. Chem. Soc. 130 (2008) 12912–12920.
[360] J. Chen, G. Wu, T. Wang, X. Li, M. Li, Y. Sang, H. Liu, Carrier step-by-step transport initiated by precise defect distribution engineering for efficient photocatalytic hydrogen generation, ACS Appl. Mater. Interfaces 9 (2017) 4634–4642.
[361] J. Park, M.K. Lee, Performance enhancement of dye-sensitized solar cell with a $TiCl_4$-treated TiO_2 compact layer, Electron. Mater. Lett. 11 (2015) 271–275.
[362] J. Zhang, T.F. Hughes, M. Steigerwald, L. Brus, R.A. Friesner, Realistic cluster modeling of electron transport and trapping in solvated TiO_2 nanoparticles, J. Am. Chem. Soc. 134 (2012) 12028–12042.
[363] D.C. Hurum, A.G. Agrios, K.A. Gray, T. Rajh, M.C. Thurnauer, Explaining the enhanced photocatalytic activity of Degussa P25 mixed-phase TiO_2 using EPR, J. Phys. Chem. B 107 (2003) 4545–4549.
[364] D.O. Scanlon, C.W. Dunnill, J. Buckeridge, S.A. Shevlin, A.J. Logsdail, S.M. Woodley, C.R.A. Catlow, M.J. Powell, R.G. Palgrave, I.P. Parkin, G.W. Watson, T.W. Keal, P. Sherwood, A. Walsh, A.A. Sokol, Band alignment of rutile and anatase TiO_2, Nat. Mater. 12 (2013) 798–801.
[365] S.K. Wallace, K.P. McKenna, Grain boundary controlled electron mobility in polycrystalline titanium dioxide, Adv. Mater. Interfaces 1 (2014) 1400078.
[366] J.M. Jiménez, G.R. Bourret, T. Berger, K.P. McKenna, Modification of charge trapping at particle/particle interfaces by electrochemical hydrogen doping of nanocrystalline TiO_2, J. Am. Chem. Soc. 138 (2016) 15956–15964.
[367] N.A. Deskins, M. Dupuis, Electron transport via polaron hopping in bulk TiO_2: a density functional theory characterization, Phys. Rev. B 75 (2007) 195212.
[368] P. Zawadzki, A.B. Laursen, K.W. Jacobsen, S. Dahl, J. Rossmeisl, Oxidative trends of TiO_2–hole trapping at anatase and rutile surface, Energy Environ. Sci. 5 (2012) 9866–9869.
[369] G.M. Turner, M.C. Beard, C.A. Schmuttenmaer, Carrier localization and cooling in dye-sensitized nanocrystalline titanium dioxide, J. Phys. Chem. B 106 (2002) 11716–11719.
[370] T.J. Savenije, M.P. de Haas, J.M.Z. Warman, The yield and mobility of charge carriers in smooth and nanoporous TiO_2 films, Z. Phys. Chem. 212 (1999) 201–206.
[371] A. Furube, T. Asahi, H. Masuhara, H. Yamashita, M. Anpo, Direct observation of a picosecond charge separation process in photoexcited platinum-loaded TiO_2, particles by femtosecond diffuse reflectance spectroscopy, Chem. Phys. Lett. 336 (2001) 424–430.
[372] M. Anpo, M. Takeuchi, Effect of the local structure of Ti-oxide species on the photocatalytic reactivity and photo-induced super hydrophilic properties of Ti/Si and Ti/B binary oxide thin films, J. Catal. 216 (2003) 505–516.
[373] B. Enright, D. Fitzmaurice, Spectroscopic determination of electron and hole effective masses in a nanocrystalline semiconductor film, J. Phys. Chem. 100 (1996) 1027–1035.
[374] H.S. Steven, J.A. Moss, M.R. Hoffmann, Slow surface charge trapping kinetics on irradiated TiO_2, J. Phys. Chem. B 106 (2002) 2922–2927.
[375] M.H. Zarifi, A. Mohammadpour, S. Farsinezhad, B.D. Wiltshire, M. Nosrati, A.M. Askar, M. Daneshmand, K. Shankar, Time-resolved microwave photoconductivity (TRMC) using planar mcrowave resonators: Application to the study of long-lived charge pairs in photoexcited titania nanotube arrays, J. Phys. Chem. C 119 (2015) 14358–14365.
[376] M. Sachs, E. Pastor, A. Kafizas, J.R. Durrant, Evaluation of surface state mediated charge recombination in anatase and rutile TiO_2, J. Phys. Chem. Lett. 7 (2016) 3742–3746.
[377] A. Stevanovic, J.T. Yates Jr., Electron hopping through TiO_2 powder: a study by photoluminescence spectroscopy, J. Phys. Chem. C 117 (2013) 24189–24195.
[378] T. Berger, M. Sterrer, O. Diwald, E. Kno1zinger, D. Panayotov, T.L. Thompson, J.T. Yates Jr., Light-induced charge separation in anatase TiO_2 particles, J. Phys. Chem. B 109 (2005) 6061–6068.
[379] Y. Yamada, Y. Kanemitsu, Determination of electron and hole lifetimes of rutile and anatase TiO_2 single crystals, Appl. Phys. Lett. 101 (2012) 133907.
[380] P. Maity, O.F. Mohammed, K. Katsiev, H. Idriss, Study of the bulk charge carrier dynamics in anatase and rutile TiO_2 single crystals by femtosecond time-resolved spectroscopy, J. Phys. Chem. C 122 (2018) 8925–8932.
[381] S.A. Haue, Y. Tachibana, D.R. Klug, J.R. Durrant, Charge recombination kinetics in dye-sensitized nanocrystalline titanium dioxide films under externally applied bias, J. Phys. Chem. B 102 (1998) 1745–1749.
[382] P. Deák, B. Aradi, T. Frauenheim, Oxygen deficiency in TiO_2: similarities and differences between the Ti self-interstitial and the O vacancy in bulk rutile and anatase, Phys. Rev. B 92 (2015) 045204.
[383] Y. Chiba, A. Islam, Y. Watanabe, R. Komiya, N. Koide, L. Han, Dye-sensitized solar cells with conversion efficiency of 11.1%, Jpn. J. Appl. Phys. 45 (2006) 24–28.
[384] S.G. Kumar, L.G. Devi, Review on modified TiO_2 photocatalysis under UV/visible light: selected results and related mechanisms on interfacial charge carrier transfer dynamics, J. Phys. Chem. A 115 (2011) 13211–13241.
[385] J.X. Low, V. Cheng, J.G. Yu, Surface modification and enhanced photocatalytic CO_2 reduction performance of TiO_2. A review, Appl. Surf. Sci. 392 (2017) 658–686.
[386] I. Mora-Seró, J. Bisquert, Fermi level of surface states in TiO_2 nanoparticles, Nano Lett. 3 (2003) 945–949.
[387] Y. Ji, W. Guo, H. Chen, L. Zhang, S. Chen, M. Hua, Y. Long, Surface Ti^{3+}/Ti^{4+} redox shuttle enhancing photocatalytic H_2 production in ultrathin TiO_2 nanosheets/CdSe quantum dots, J. Phys. Chem. C 119 (2015) 27053–27059.
[388] Y. Tamaki, A. Furube, M. Murai, K. Hara, R. Katoh, M. Tachiya, Direct observation of reactive trapped holes in TiO_2 undergoing photocatalytic oxidation of adsorbed alcohols: evaluation of the reaction rates and yields, J. Am. Chem. Soc. 128 (2006) 416–417.
[389] J. Tang, J.R. Durrant, D.R. Klug, Mechanism of photocatalytic water splitting in TiO_2. reaction of water with photoholes, importance of charge carrier dynamics, and evidence for four-hole chemistry, J. Am. Chem. C 130 (2008) 13885–13891.
[390] A.J. Cowan, J. Tang, W. Leng, J.R. Durrant, D.R. Klug, Water splitting by nanocrystalline TiO_2 in a complete photoelectrochemical cell exhibits efficiencies limited by charge recombination, J. Phys. Chem. C 114 (2010) 4208–4214.
[391] F. Amano, M. Nakata, A. Yamamoto, T. Tanaka, Effect of Ti^{3+} ions and conduction band electrons on photocatalytic and photoelectrochemical activity of rutile titania for water oxidation, J. Phys. Chem. C 120 (2016) 6467–6774.
[392] B. Liu, K. Cheng, S. Nie, X. Zhao, H. Yu, J. Yu, A. Fujishima, K. Nakata, Ice-water quenching induced Ti^{3+} self-doped TiO_2 with surface lattice distortion and the increased photocatalytic activity, J. Phys. Chem. C 121 (2017) 19836–19848.

[393] G. Wang, H. Wang, Y. Ling, Y. Tang, X. Yang, R.C. Fitzmorris, C. Wang, J.Z. Zhang, Y. Li, Hydrogen-treated TiO_2 nanowire arrays for photoelectrochemical water splitting, Nano Lett. 11 (2011) 3026–3033.
[394] B. Liu, K. Nakata, X. Zhao, T. Ochiai, T. Murakami, A. Fujishima, Theoretical kinetic analysis of heterogeneous photocatalysis: the effects of surface trapping and bulk recombination through defects, J. Phys. Chem. C 115 (2011) 16037–16042.
[395] O. Elbanna, M. Fujitsuka, S. Kim, T. Majima, Charge carrier dynamics in TiO_2 mesocrystals with oxygen vacancies for photocatalytic hydrogen generation under solar light irradiation, J. Phys. Chem. C 122 (2018) 15163–15170.
[396] M.A. Henderson, M. Shen, Z.T. Wang, I. Lyubinetsky, Characterization of the active surface species responsible for UV-induced desorption of O_2 from the rutile TiO_2 (110) surface, J. Phys. Chem. C 117 (2013) 5774–5784.
[397] Y.-F.L, A. Selloni, Theoretical study of interfacial electron transfer from reduced anatase TiO_2(101) to adsorbed O_2, J. Am. Chem. Soc. 135 (2013) 9195–9199.
[398] X. Li, A.N.M. Green, S.A. Haque, A. Mills, J.R. Durrant, Light-driven oxygen scavenging by titania/polymer nanocomposite films, J. Photochem. Photobiol. A: Chem. 162 (2004) 253–259.
[399] E. Lira, S. Wendt, P. Huo, J.Ø. Hansen, R. Streber, S. Porsgaard, Y. Wei, R. Bechstein, E. Lægsgaard, F. Besenbacher, The importance of bulk Ti^{3+} defects in the oxygen chemistry on titania surfaces, J. Am. Chem. Soc. 133 (2011) 6529–6532.
[400] J. Yan, G. Wu, N. Guan, L. Li, Z. Li, X. Cao, Understanding the effect of surface/bulk defects on the photocatalytic activity of TiO_2: anatase versus rutile, Phys. Chem. Chem. Phys. 15 (2013) 10978–10988.
[401] J. Li, M. Zhang, Z. Guan, Q. Li, C. He, J. Yang, Synergistic effect of surface and bulk single-electron-trapped oxygen vacancy of TiO_2, in the photocatalytic reduction of CO_2, Appl. Catal. B: Environ. 206 (2017) 300–307.
[402] X. Yu, B. Kim, Y.K. Kim, Highly enhanced photoactivity of anatase TiO_2 nanocrystals by controlled hydrogenation-induced surface defects, ACS Catal. 3 (2013) 2479–2486.
[403] M. Kong, Y. Li, X. Chen, T. Tian, P. Fang, F. Zheng, X. X. Zhao, Tuning the relative concentration ratio of bulk defects to surface defects in TiO_2 nanocrystals leads to high photocatalytic efficiency, J. Am. Chem. Soc. 133 (2011) 16414–16417.
[404] P. Salvador, Subbandgap photoresponse of n-TiO_2 electrodes: transient photocurrent-time behavior, Surf. Sci. 192 (1987) 36–46.
[405] D. Laser, S. Gottesfeld, Photocurrents induced by subbandgap illumination in a Ti-Oxide film electrode, J. Electrochem. Soc. 126 (1979) 475–478.
[406] B. Liu, J. Yang, J. Wang, X. Zhao, K. Nakata, High sub-band gap response of TiO_2 nanorod arrays for visible photoelectrochemical water oxidation, Appl. Surf. Sci. 465 (2019) 192–200.